THE UNIVERSITY OF CHICAGO

AN INTEGRATED CAVITY OUTPUT SPECTROMETER FOR MEASUREMENTS OF THE HDO/H_2O ISOTOPIC RATIO IN THE ASIAN SUMMER MONSOON

A DISSERTATION SUBMITTED TO
THE FACULTY OF THE DIVISION OF THE PHYSICAL SCIENCES
IN CANDIDACY FOR THE DEGREE OF
DOCTOR OF PHILOSOPHY

DEPARTMENT OF PHYSICS

BY
BENJAMIN WADE CLOUSER

CHICAGO, ILLINOIS
JUNE 2018

To my wife, Fatima.

5 *The sun also ariseth, and the sun goeth down*

and hasteth to his place where he arose.

6 *The wind goeth toward the south, and turneth about unto the north;*

it whirleth about continually, and the wind returneth again according to his circuits.

7 *All the rivers run into the sea; yet the sea is not full;*

unto the place from whence the rivers come, thither they return again.

8 *All things are full of labour; man cannot utter it:*

the eye is not satisfied with seeing, nor the ear filled with hearing.

9 *The thing that hath been, it is that which shall be;*

and that which is done is that which shall be done: and there is no new thing under the sun.

— The Preacher

TABLE OF CONTENTS

LIST OF FIGURES

LIST OF TABLES

LIST OF ABBREVIATIONS

AIDA Aerosol Interactions and Dynamics in the Atmosphere

AM Asian Monsoon

APeT AIDA PCI extractive TDL

ATD Arizona Test Dust

ChiWIS Chicago Water Isotope Spectrometer

CRDS Cavity Ringdown Spectroscopy

DFB Distributed Feedback

FISH Fast In-situ Stratospheric Hygrometer

FLASH Fluorescence Advanced Stratospheric Hygrometer

HITRAN High Resolution Transmission database for spectroscopy

ICOS Integrated Cavity Output Spectroscopy

IsoCloud Isotopic fractionation in Clouds

KIT Karlsrühe Institute of Technology

MDB Myasichiev Design Bureau

MK Murphy-Koop

MOV Metal Oxide Varistor

PCV Plano-Concave

PCX Plano-Convex

SA Sulfuric Acid

SOA Secondary Organic Aerosols

SP-APicT Single-Path AIDA PCI in cloud TDL

TDL Tunable Diode Laser

TDLAS Tunable Diode Laser Absorption Spectroscopy

TTL Tropical Tropopause Layer

UT/LS Upper Troposphere/Lower Stratosphere

VSMOW Vienna Standard Mean Ocean Water

ACKNOWLEDGMENTS

The work presented here has spanned five years and two field campaigns, and I owe many people thanks for their time and effort.

From the IsoCloud campaigns I'd like to thank the scientists and staff at KIT, Ottmar Möhler, Harald Saathoff, Jan Habig, and Naruki Hiranuma. From PTB Braunschweig and the University of Darmstadt, I'd like to thank Volker Ebert, Bennjamin Kühnreich, and Steven Wagner. From Universitè Joseph Fourier Grenoble, I'd like to thank Janek Landsberg and Erik Kerstel. Financial support for the IsoCloud campaigns was provided by an International Collaboration in Chemistry grant (joint NSF-DFG).

From the StratoClim campaigns I'd first like to thank the whole StratoClim team, especially Fred Stroh, and Marcus Rex, and Leena-Kaisa Viitanen for making it happen through years of effort and numerous setbacks, and Marc Von Höbe for useful discussions. I'd also like to thank the MDB team for keeping the aircraft up and running in conditions that were often not optimal. Big thanks to Antonis Dragoneas for accepting huge responsibility for the group beyond what he already had, and making the Kalamata campaign happen. I'd like to acknowledge all the help we got from the support staffs in Kiruna, Kalamata, and Kathmandu, especially the Buddha Air ground crew.

Thanks to Rudy Montoya, Jim Ranson, Steve Gabbard, and Steve Shertz from NCAR for their expert engineering and technical help. Without them, ChiWIS wouldn't exist. I'd especially like to thank Steve Shertz for his mentorship and the time he took to teach me. Thanks to Vic Guarino and Steve Clark for their patience and engineering expertise. I'd like to acknowledge all the engineers I've talked to over the phone over the last few years who got genuinely excited about this project, and went far beyond what was required of them to help me out and point me in the right direction.

From the University of Chicago there are many people to thank, so I'll start at the beginning. I'd like to thank Tom Rosenbaum for his patience and understanding at a time when I didn't know what I wanted, and Helmut Krebs for teaching me to be safe and effective

in the machine shop. Thanks to Liz Moyer for all the great opportunities I've had to learn, build, and travel in her research group. Thanks to Kara Lamb for many useful discussions in regards to the IsoCloud campaigns. Thanks to Max Bolot for expanding my horizons in regards to estimation techniques, and teaching me everything I know about France. Thanks to Clare Singer and Dylan Gaeta for all their help in the lab and in Kathmandu.

Special thanks to Laszlo Sarkozy for numerous useful discussions, mentorship, and guidance in the lab, and companionship in all the long and late hours we doubled as electricians, plumbers, and long-haul truckers.

Eternal gratitude to my wife Fatima for her patience through all my long deployments into the field, to Colorado, and sometimes just to Hinds.

Last, and most importantly, I'd like to thank my parents and grandparents, Sid, Anne, Lamoine, Sue, Frank, and Irene, for the opportunities, guidance, and culture that let me achieve everything I have so far.

ABSTRACT

The Tropical Tropopause Layer (TTL) and the Asian Monsoon (AM) are important regions for current and future climate. They are the main pathways by which tropospheric air ascends into the stratosphere, and the TTL is the coldest region of the lower atmosphere (at times $T < 185\ K$). Air ascending through the TTL is dehydrated by formation of high-altitude cirrus, which are radiatively important, producing a total radiative forcing of $4\ {}^{W}/_{m^2}$ over the tropics. The link between deep convection and high-altitude cirrus is an important potential positive feedback in a changing climate. A warmer world may experience more frequent and vigorous deep convection, resulting in more high-altitude cirrus clouds that contribute to warming.

In-situ measurements of water isotopologues can help reveal how convective detrainment of water vapor contributes to later cirrus formation. Convectively lofted ice is isotopically heavier than surrounding vapor since the heavier isotopologues (e.g. HDO and $H_2^{18}O$) preferentially partition into the condensed phases. As this lofted ice sublimates, its isotopic signature is imprinted on the TTL. Both remote sensing and in-situ instruments have measured isotopic profiles that show an increase with altitude in the TTL, likely due to the sublimation of lofted ice. These profiles provide information about the importance of convective detrainment of vapor and ice relative to other sources and sinks in the overall water budget.

The AM is an especially interesting area for TTL water isotopologue measurements. The AM may contribute up to 75% of the upward water vapor flux to the tropopause in Northern Hemisphere summer. Recent analysis of ACE-FTS satellite data shows significant differences in water vapor isotopic enhancement between the North American and Asian monsoons, suggesting differences in water transport processes, but no in-situ water isotopologue measurements in the AM have yet verified this observation. High-altitude measurements of the AM are extremely limited in general, and StratoClim will provide a valuable new perspective on this important region.

Here I describe the motivation, design, construction, and performance of an Integrated Cavity Output Spectrometer (ICOS), designed to make the first measurements of the HDO/H_2O ratio in the Asian Summer Monsoon. In addition, I discuss the context motivating the construction of this instrument, and describe the results of an investigation into the metastable forms of ice that resulted from previous cloud chamber studies. In the following, Chapter 1 reviews the properties of water and introduces the scientific motivation for studying cirrus clouds and the isotopic composition of atmospheric water vapor; Chapter 2 reviews the principles underlying measurements by absorption spectroscopy; Chapter 3 describes results from an experimental campaign at the AIDA cloud and aerosol chamber using the custom-built Chicago Water Isotope Spectrometer (ChiWIS); Chapter 4 describes the design of a new version of ChiWIS for use on high-altitude aircraft that relies on Integrated Cavity Output Spectroscopy (ICOS); and Chapter 5 describes a new optical element designed to mitigate poor light collection efficiency in ICOS instruments. The non-axially symmetric optical component described here increases the light collection efficiency of the instrument by a factor of 6. ChiWIS flew aboard a high-altitude aircraft in the 2017 StratoClim science campaign out of Kathmandu, Nepal, and Chapter 6 reviews the measurements and field performance of the instrument during this campaign.

CHAPTER 1

INTRODUCTION

This chapter provides brief introductions to some important concepts found throughout this manuscript. Section 1.1 gives overview of the properties of water, including its importance to the broader climate, the range of concentrations found throughout the atmosphere, metastable forms of ice that may be found in the coldest parts of the atmosphere, and the relative concentrations of the 9 stable isotopologues of water. Following that is a review of stable isotope physics and a brief explanation of how it is applied to understand processes in the atmosphere. Section 1.3 gives a brief introduction to monsoons in general and the Asian Summer monsoon in particular, and is followed by a brief discussion of the importance of field campaigns. Last is an overview of the structure of this thesis.

1.1 Properties of Water

Water is a unique substance for a variety of reasons, not least of which is that it simultaneously exists in three phases on Earth's surface and in its atmosphere. Each of these phases has numerous and profound impacts on the planet: water vapor is the main greenhouse gas on Earth, accounting for about 60% of the greenhouse effect [Kiehl and Trenberth, 1997]; liquid water covers about 70% of Earth's surface; ice covers $\approx 10\%$ of Earth's surface, and its high albedo reflects about 2% of the sun's energy back into space annually. Water also has an unusually high latent heat, which means that its phase changes absorb and release significant energy, and that advection and convection of liquid and solid cloud particles serve as a primary pathway of transporting energy throughout Earth's atmosphere. Indeed, Earth's energy budget and energy balance cannot be understood without including the phase changes of water [Pierrehumbert, 2002].

While chemically similar, the isotopologues of water differentiate under phase transitions, with the heavier isotopologues preferring to be in the condensed phase. So during the growth

of an ice cloud, for example, the vapor will become depleted in heavier isotopologues and the ice enriched. This effect allows the HDO/H2O ratio, for example, to be used as a tracer of both microphysical and large scale processes. Although H_2O is the most common form of water, the singly-substituted isotopologues $H_2{}^{17}O$, $H_2{}^{18}O$, and HDO are all abundant enough to measure through mass and absorption spectroscopies.

1.1.1 The Clausius-Clapeyron relation

The Clausius-Clapeyron relation is derived from the fact that along a phase boundary, the Gibbs free energy must be the same regardless of the phase of the material. From this, the slope of the phase boundary line is found to be (e.g. Schroeder [1999]):

$$\frac{dP}{dT} = \frac{S_2 - S_1}{V_2 - V_1} \tag{1.1}$$

Here $S_{1,2}$ and $V_{1,2}$ are the entropies and volumes associated with the two phases in question. Recognizing that the entropy difference between the phases is equal to L/T, the latent heat of the phase transition over the temperature, and writing $\Delta V = V_2 - V_1$, we can write the Clausius-Clapeyron relation:

$$\frac{dP}{dT} = \frac{L}{T\Delta V} \tag{1.2}$$

In Earth's atmosphere the ideal gas law is a reasonable approximation, and in the case of water's liquid-gas and solid-gas phase transformations, $V_g \gg V_l$, so equation 1.2 can be rewritten as

$$\frac{de_s}{dT} = \frac{Le_s}{R_v T^2} \tag{1.3}$$

In this equation R_v is the gas constant of water, and e_s is the saturation vapor pressure over the condensed phase. Latent heat is not a strong function of temperature, and for most applications it is acceptable to treat it as a constant. Integrating equation 1.3 yield an

expression for the saturation vapor pressure of water over liquid or ice

$$e_s(T) = e_{s0} e^{\frac{L}{R_v}\left(\frac{1}{T_0} - \frac{1}{T}\right)} = Ae^{-B/T} \tag{1.4}$$

Here $e_{s0} = 6.11$ hPa is the experimentally determined saturation vapor pressure at $T_0 = 273.15$ K, and is the same to 3 significant figures for water and ice. For water $A = 2.53 \times 10^9$ hPa and $B = 5.42 \times 10^3$ K, and for ice $A = 3.41 \times 10^{10}$ hPa and $B = 6.13 \times 10^3$ K [Rogers and Yau, 1989]. The saturation vapor pressure sets the range of water vapor concentrations found in Earth's atmosphere, and varies nearly exponentially as a function of temperature. This large range is set by the saturation vapor pressure of water, which varies nearly exponentially as a function of temperature. From the coldest parts of the Tropical Tropopause Layer ($T \approx 190$ K) to the warmest and wettest parts of the tropics, water vapor concentrations span nearly 4 orders of magnitude.

1.1.2 Metastable forms of ice

The phase diagram of solid H_2O is extremely complicated [Hobbs, 1974], with at least 17 different ice structures known. These structures are typically probed using x-ray, electron, or neutron diffraction, which give detailed information about the crystal structure of the water molecules. These crystals can be formed through a variety of methods including deposition, compression, and annealing. In the conditions found in Earth's atmosphere, ice forms sheets of puckered, hexagonal rings, which can either be layered as mirror images or shifted by half a ring width (Figure 1.1). The former is the familiar hexagonal ice (I_h), and the latter is the hypothesized cubic ice (I_c). Hexagonal ice is the stabler of the two crystal structures, although there is evidence [Takahashi, 1982] that when ice nucleates from the liquid it forms embryonic cubic ice structures which subsequently anneal to hexagonal ice. Since I_c is metastable with respect to I_h, and should therefore have a higher vapor pressure, it has been proposed as the cause of so-called anomalous supersaturation [Peter et al., 2006],

where relative humidities well in excess of 100% are observed even in the presence of ice clouds. However, pure cubic ice has never been observed in Earth's atmosphere.

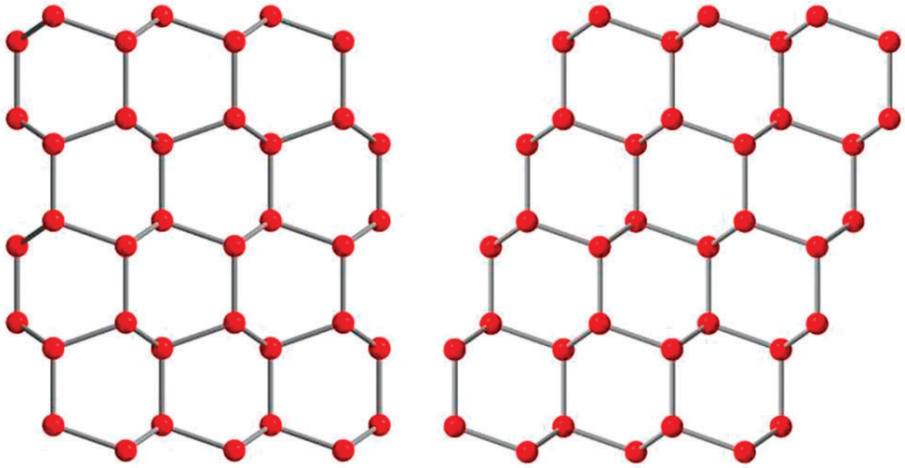

Figure 1.1: Ice I is composed of sheets of puckered, hexagonal rings of water molecules, and has two subtypes: hexagonal ice (I_h) and cubic ice (I_c). In I_h the sheets are arranged as mirror images (*left*), and in I_c they are shifted by half a ring width with respect to the previous layer. Figure from Malkin et al. [2015b].

Ice deposited in the coldest parts of Earth's atmosphere appears to sometimes form a stacking-disordered phase (I_{sd}), which consists of randomly alternating layers of I_h and I_c orientations. I_{sd} is primarily characterized by a cubicity value χ, which is the proportion of layers that have cubic orientation with respect to the previous layers. The stacking disordered structure does not appear to be significantly less stable than that of I_h, but such crystals often contain large numbers of faults and defects which do make significant contributions to the free energy of stacking disordered crystals which may result in elevated vapor pressures[].

Chapter 3 will discuss the results of an investigation into metastable forms of ice at the AIDA cloud chamber at the Karlsruhe Institute of Technology (KIT).

1.1.3 Isotopologues of Water

The water molecule is composed of two hydrogen atoms and one oxygen atom. There are two stable forms of hydrogen (^{1}H and ^{2}H = D), and three stable forms of oxygen (^{16}O, ^{17}O, and ^{18}O), which form 9 different isotopologues of water. The 7 most abundant of these

isotopologues are listed in Table 1.1, along with their natural abundances [Biévre et al., 1984]. The term isotopologue refers only to molecules with a different number of isotopes, whereas isotopomer refers to isotopologues with different arrangements within a molecule. For example, ^{14}N-^{15}N-^{16}O and ^{15}N-^{14}N-^{16}O are different isotopomers of nitrous oxide, but both have the same number of each component isotope and are considered to be the same isotopologue. Here I will generally use the word 'isotope' to describe the methods and theory, but 'isotopologue' to refer to specific isotopologues of water.

Table 1.1: Natural abundances of water isotopologues

Isotopologue	Abundance
$H_2{}^{16}O$	0.997317
$H_2{}^{18}O$	0.00200
$H_2{}^{17}O$	3.718840e-04
$HD^{16}O$	3.106930e-04
$HD^{18}O$	6.230030e-07
$HD^{17}O$	1.158530e-07
$D_2{}^{16}O$	2.419700e-08

These isotopologues have slightly different physical properties, such as density, vapor pressure, and absorption spectra. These differences can be exploited to infer information about mixing, condensation and evaporation, and transport processes in Earth's atmosphere, and will be covered in more detail in section 1.2.5.

1.2 Review of Stable Isotope Physics

Stable isotope physics is a powerful tool which draws on and contributes to many different fields. When applied to observations of the distribution of water vapor isotopologues, isotopic measurements can provide information about large scale transport in the atmosphere, the temperature at which ice in Greenland and Antarctica was formed, and detailed information about the microphysics of growing ice crystals. I briefly review here the important concepts necessary to understand the distribution of water vapor isotopologues in the atmosphere. This section follows the outline of the much more detailed work of [Criss, 1999].

1.2.1 Background

Isotopes are nuclides that have the same number of protons, but differing numbers of neutrons. The number of protons is commonly called the atomic number and is denoted Z, and the number of neutrons is denoted by $\mathcal{N}$. The mass number of a nuclide is given by

$$A = \mathrm{Z} + \mathcal{N} \tag{1.5}$$

Nuclides with the same atomic number are electronically similar since they have the same number of protons and electrons, and consequently behave quite similarly chemically, tend to be in the same phase under the same conditions, etc. The differing masses of isotopes gives rise to slight but noticeable differences. Here we focus on fractionation, which is the differential partitioning of isotopes between the phases during a phase transition. Fractionation falls into two broad categories: equilibrium fraction which is a mass-dependent, quantum mechanical effect, and non-equilibrium fractionation which is typically due to processes that are fast, irreversible, or one-directional.

The amount of an isotope present is often expressed as a ratio of the heavier isotope to the lighter one. Various standards exist for which the ratios of common isotopes are very well known. For example, the D/H ratio of Vienna Standard Mean Ocean Water (VSMOW) is very well known ($R_{VSMOW,D/H}$ = D/H = 155.95×10^{-6}), as is the ^{18}O/^{16}O ratio ($R_{VSMOW,^{18}O/^{16}O}$ =^{18} O/^{16}O = 2005.2×10^{-6}) [Araguás-Araguás et al., 2000]. Isotopic ratios are often expressed relative to a standard in δ notation, which allows for much easier comparison of results between instruments and measurement methods. For example, the deuterium concentration in a water sample can be expressed in per mille (‰) as:

$$\delta\mathrm{D} = \frac{R_{samp} - R_{VSMOW,D/H}}{R_{VSMOW,D/H}} \times 1000 \tag{1.6}$$

δD values can range from -1000‰ to ∞, which correspond to a sample with none of the heavy

isotope and one with only the heavy isotope, respectively. Samples with more negative values are 'depleted', and those with more positive values are 'enriched'. Typically δ values are very small, but for the hydrogen isotopes of water they can be quite large. For example, in the stratosphere typically $\delta D \approx -600‰$ [Randel et al., 2012].

1.2.2 Fractionation

Isotopic abundances vary from sample to sample, and the processes controlling that variation give insight into the natural world. When some effect causes variation in the distribution of isotopes or isotopologues, it is referred to as fractionation. The value of isotopic measurements of water mainly stems from an understanding of the effects of mixing and fractionation on observations. This section will focus solely on fractionation, but treatments of the effects of mixing on isotopic measurements can be found in Galewsky and Hurley [2010], Criss [1999]. These processes can be broadly divided into equilibrium and non-equilibrium processes. In the following subsections reference will often be made to water, but in principle the ideas introduced are applicable to any system containing two or more species which undergoes a phase transition.

If some process results in fractionation it can be associated with a fractionation factor:

$$\alpha = \frac{R_b}{R_a}, \tag{1.7}$$

which represents the ratio of isotopologues in one phase or part of a reaction to the ratio in the other. Here the ratios are defined as $R_i = N_{b,i}/N_{a,i}$, where the subscript i represents the phase or part of the system, and a and b represent two isotopologues. Typically b is the heavier isotopologue and a is the lighter one. Equation 1.7 can be rewritten as a differential equation that describes the changes in bulk composition as material is added or removed:

$$\alpha = \frac{d \ln N_b}{d \ln N_a}, \tag{1.8}$$

This formulation is quite useful for understanding the distribution of water vapor isotopologues in Earth's atmosphere (Section 1.2.5).

Equilibrium Fractionation

Equilibrium fractionation is the partitioning of isotopologues in chemical equilibrium, and occur during chemical reaction, phase changes, and as a result of gravitational settling, to name a few examples. Here I focus on the fractionation due to phase changes, specifically from gaseous to a condensed phase. Phase changes are mass dependent processes, in that heavier isotopologues tend to be more strongly bound to their neighbors in the condensed phases and slower to propagate through diffusion in the vapor. This tighter binding manifests as a lower vapor pressure for heavier isotopologues, first observed by Wahl and Urey [1935] in their study of heavy water. In practice, this difference in vapor pressure typically results in the heavier isotopologues being more abundant in the condensed phases. Numerous works have investigated the VPIE, and a detailed derivation can be found in [Hopfner, 1969].

Equilibrium fractionation across a phase boundary is intimately related to the fundamental spectroscopy of a molecule or atom, as both rely on a detailed accounting of the quantum energy levels of the species in question. Urey's statistical mechanical theory of fractionation [Urey, 1947] shows that fractionation of gaseous diatomic molecules is strongly dependent on the ratios of the partition function of the isotopologues. He derived a simplified ratio of partition functions for a molecule (a) and its isotopologue (b):

$$\frac{Q_b}{Q_a} = \frac{\sigma_a U_b}{\sigma_b U_a} \cdot \frac{e^{-U_b/2}}{e^{-U_a/2}} \cdot \frac{1 - e^{-U_a}}{1 - e^{-U_b}} \tag{1.9}$$

Here U is the spacing of the vibrational energy levels, $h\nu/kT$, and the σ's represent the symmetry of the molecule. The first factor on the right is due to the rotation of the molecule, the second is due to the zero-point energy, and the third is due to the vibrational energy level spacings. The zero-point energy contribution and the vibrational spacings are typically

the most important in this ratio. Similar formulas hold for non-linear polyatomic molecules possessing more vibrational and rotational degrees of freedom.

The fractionation factor can be related to the ratio of partition functions given above through the equilibrium constant of the 'reaction' [Ferronsky, 1982], which is given by:

$$\alpha = \left(\frac{K}{K_\infty} \right)^{1/ac}, \tag{1.10}$$

where ac is equal to the number of atoms exchanged in the isotopic reaction, and K_∞ is the equilibrium constant at very high temperatures. Depending on the molecule and temperature range in question, the equilibrium fractionation factor may have a temperature dependence proportional to $1/T$ or $1/T^2$. In some cases, the temperature dependence may be more complicated, and a more general form is used [Criss, 1999]:

$$\ln \alpha = C_0 + C_1/T + C_2/T^2 \tag{1.11}$$

Table 1.2: Fractionation Parameters for ^{18}O and D

Atom	Phase	C_0	C_1	C_2	Citation
D	Liquid-Gas	5.2612e-02	-76.248	24844	Majoube, Michel [1971]
D	Ice-Gas	-0.0934	0	16288	Majoube, Michel [1971]
^{18}O	Liquid-Gas	-2.0667e-03	-0.4156	1137	Majoube, Michel [1971]
^{18}O	Ice-Gas	-0.028224	0	11.839	Merlivat and Nief [1967]

Liquid-gas and ice-gas fractionation factors for D and ^{18}O are presented in Table 1.2. Numerous other works have investigated these fractionation factors for both solids and liquids including Matsuo et al. [1964], Johansson and Holmberg [1969], Pupezin et al. [1972], Ellehøj et al. [2013], Lamb et al. [2017].

1.2.3 Non-equilibrium Fractionation

Non-equilibrium fractionation effects associated with water are often due to diffusional effects, and are typically associated with growth/evaporation in super- or subsaturated con-

ditions. These effects are typically expressed as a correction factor on the equilibrium fractionation value.

The equipartition theorem states that on average a system's energy should be evenly divided amongst its degrees of freedom. In the case of an ideal gas, this means that on average the all molecules making up the gas will have the same average kinetic energy. Since gases are typically composed of many different species, some with different masses, this means that each species will have its own typical velocity, and consequently, its own characteristic rate of diffusion. This observation gives rise to Graham's law of diffusion:

$$\frac{v_1}{v_2} = \sqrt{\frac{m_2}{m_1}}, \tag{1.12}$$

which provides a starting point for understanding these types of non-equilibrium effects. Here the v_i's are the average velocity for each molecule, and this ratio represents the ratio of the diffusion rates. This theory is not exact, however, and typically diffusivity ratios have to be measured. Diffusivity ratios between H_2O and its heavier isotopologues have been measured by [Ehhalt and Knott, 1965, Merlivat, 1978, Cappa et al., 2003, Luz et al., 2009].

Evaporation

A theory of fractionation due to evaporation from liquid can be developed from the recognition of the fact that evaporation is the result of two competing processes: molecules leaving the liquid reservoir and going into the vapor, and water vapor molecules striking the liquid and becoming attached to it. The rate of molecules leaving is proportional to the activity of the water, and the rate of molecules entering the water is proportional to the partial pressure of the water vapor [Criss, 1999]. From these assumptions one can derive a non-equilibrium evaporation fractionation factor that depends on the properties of the carrier gas into which the evaporation is occurring:

$$R_E = \frac{R_w - \alpha_{eq} h R_v}{\alpha^0_{evap}\,(1-h)}, \tag{1.13}$$

where h is the relative humidity of the carrier gas, R_v is the isotopic ratio of the carrier gas, R_w is the isotopic ratio of the water, R_E is the isotopic ratio of the evaporate, α_{eq} is the equilibrium fractionation factor, and α^0_{evap} is the non-equilibrium fractionation between the water and the component lost under zero humidity.

Evaporation from ice into subsaturated air is thought to simply strip off the layers exposed to the vapor, preserving the isotopic composition of the ice.

Condensation

Similarly, the supersaturated conditions in which condensation often occurs result in non-equilibrium corrections to the fractionation factor. The effects are due to the fact that the heavier water isotopologues diffuse more slowly through air, and can become depleted in the near-field of a growing ice crystal, as the heavy isotopologues diffuse too slowly to replace those that attach to the crystal. The result of this is that the vapor remains isotopically heavier than it otherwise would.

Jouzel and Merlivat [1984] investigated these effects and derived a kinetic correction to the equilibrium fractionation factor in supersaturated conditions:

$$\alpha_{kin} = \frac{S}{\alpha_{eq} D/D' \left(S-1\right) + 1}, \tag{1.14}$$

where S is the saturation, D/D' is the ratio of diffusivities between H_2O and the heavier isotopologue, respectively, and α_{eq} is the equilibrium fractionation factor. This relationship is, of course, subject to further corrections from effects like ventilation, for example.

Having considered fractionation factors, I now consider how isotopic ratios evolve in systems undergoing condensation or evaporation.

1.2.4 Rayleigh Fractionation

The Rayleigh distillation occurs when one component of a system with multiple phases is continually removed. This process is a good approximation to the formation of precipitation in the presence of water isotopologues, since the precipitation continually falls out of the air parcel it forms in. If a vapor sample has isotopic ratio $R = N_b/N_a$ and the total number of molecules is $N = N_a + N_b$, where N_b is the rare isotope, then as vapor condenses at equilibrium, mass balance demands that:

$$\frac{NR}{1+R} = \frac{(N+dN)(R+dR)}{1+R+dR} - \frac{\alpha R}{1+\alpha R}dN \tag{1.15}$$

Given the typical abundances of water vapor isotopologues on Earth (Table 1.1), the value of R is much less than one and the denominators of each term above can be approximated as one. In that case, the equation reduces to:

$$NR = (N+dN)(R+dR) - \alpha R dN \tag{1.16}$$

Rearranging and dropping the second order terms yields the differential equation:

$$\frac{dR}{R} = (\alpha - 1)\frac{dN}{N}. \tag{1.17}$$

Assuming α is constant and with initial conditions N_0 and R_0 yields the Rayleigh equation [Rayleigh, 1902]:

$$R = R_0 f^{\alpha - 1}, \tag{1.18}$$

where $f = N/N_0$ is the fraction of the original material left in the vapor phase, and R represents the isotopic ratio of the vapor.

1.2.5 Application to Water in Earth's Atmosphere

Since the advent of mass spectrometers sensitive enough to make the necessary measurements [Nier, 1947, McKinney et al., 1950], the global distribution of water vapor isotopologues in Earth's hydrosphere and atmosphere have been shown to be reasonably well described by the isotopic physicos described in previous sections. Dansgaard [1953] found a relationship between the condensation temperature of precipitation and ^{18}O abundance, and Craig [1961], Dansgaard [1964], Craig and Gordon [1965] explained the observed abundances in ocean water, polar ice, and precipitation. Craig [1961] postulated the 'meteoritic water line' which relates the measured deuterium and ^{18}O values in precipitation found all over the world:

$$\delta\mathrm{D} = 8\ \delta^{18}\mathrm{O} + 10. \tag{1.19}$$

Beyond providing a first-order understanding of the global distribution of water vapor isotopologues, these tools also provide understanding into other important atmospheric phenomena. The relationships between temperature and isotopic abundance can be used to estimate temperature profiles from ice cores [Dansgaard et al., 1969], which have been used to infer past climate [Legrand and Mayewski, 1997]. Remote sensing and in-situ measurements [Moyer et al., 1996, Hanisco et al., 2007, Sayres et al., 2010, Kuang et al., 2003] of the δD values in the Upper Troposphere/Lower Stratosphere (UT/LS), provide insight into stratosphere-troposphere exchange. Rayleigh fractionation does a good job explaining the observed depletions up to the upper troposphere at which point convectively detrained ice becomes an important factor. Its presence can be inferred by the isotopic enhancement associated with the complete evaporation of ice into the dry air at these altitudes. This exchange helps to set the water vapor concentration of the stratosphere and is thus essential to understanding its radiative properties and ozone chemistry [de F. Forster and Shine, 1999, Kirk-Davidoff et al., 1999]. The stable isotopologues of water have also been used to study water vapor transport and mixing in the free troposphere [Galewsky et al., 2007,

2011, Hurley et al., 2012, Dyroff et al., 2015], which is necessary for a better understanding of the water vapor feedback, an important element in global warming induced changes in subtropical humidity.

In general the observed water vapor isotopologue abundances in the boundary layer are difficult to interpret as they reflect many different processes [Wen et al., 2010], including in-mixing from the free troposphere [Welp et al., 2012], exchange with precipitation [Lai and Ehleringer, 2011], evaporation from soil or sea surface [Merlivat and Jouzel, 1979], and transpiration from plants [Moreira et al., 1997, Yepez et al., 2003, Williams et al., 2004].

1.3 The Asian Summer Monsoon

Because this thesis involves measurements made oven the Asian Monsoon, I review monsoon systems, then focus on the Asian Summer Monsoon, and finally turn to how isotopologues can be used to understand them.

Monsoons are weather systems with a wet phase and a dry phase. The wet phases are typically associated with 'sea breezes' onto land from the cooler seas, and the dry phases are associated with 'land breezes' from the cold winter continents out to sea. The strongest monsoon systems also show marked changes in wind patterns. The two most organized monsoon systems are the North American Monsoon (NAM) and the Asian Monsoon (AM), and the latter is the greater of the two. Historically the AM was known for two things: the monsoon rains, which water the crops of South Asia, and the the reversal of the trade winds from northeast to southwest, which set the clock on trade with other parts of the world.

The Asian Summer monsoon is the largest and most organized on Earth. In the broadest terms, it is driven by three processes. As the sun moves higher in the sky during northern hemisphere summer, the southern hemisphere has a net radiative loss, and the northern hemisphere has a net radiative gain. These differences in net radiative heating result in large scale flows that attempt to redistribute the heat. Locally, differences in heating can greatly amplify these large scale effects, and the contrast between land and sea is one of the strongest

examples of this for two reasons. The first is that the specific heat of water is about twice that of dry land, so for each unit of heat added, the temperature increase of the land surface is twice that of water. The second is that the sea's effective heat capacity is much greater than that of land, due mainly to the sea surface mixing with the cooler layers below. This land/sea difference is the first ingredient necessary for the AM, and it creates surface level pressure gradients shown in Figure 1.2 that drive moist air from the sea to the land.

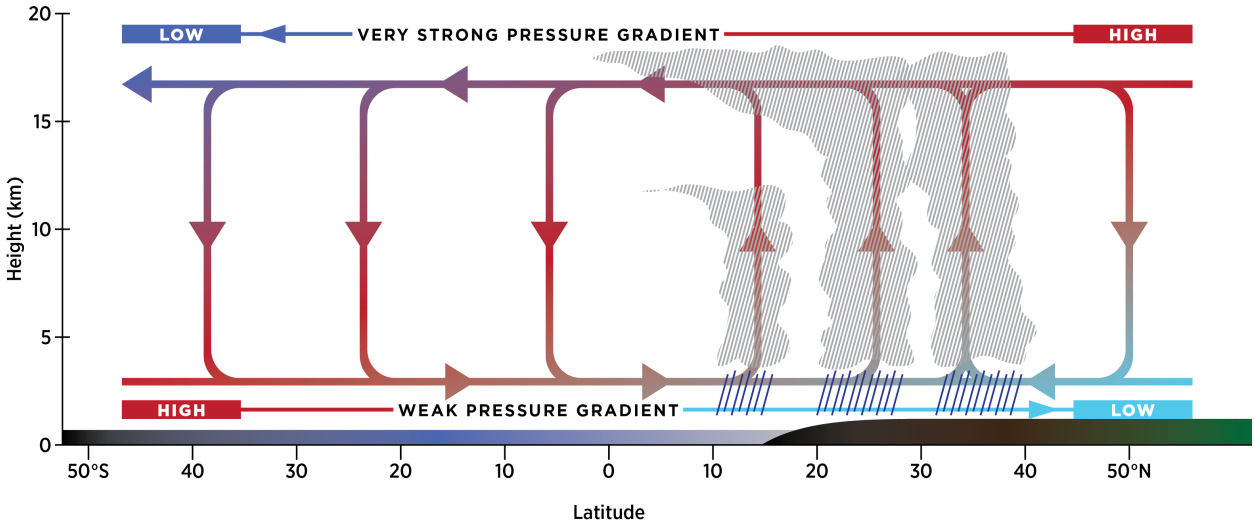

Figure 1.2: Monsoon winds are driven by differential heating of land and sea. Low pressure forms over the hotter land, driving moist air from the sea to land. This moist air convects over land, and the resulting condensation intensifies the monsoon through the release of latent heat. At high altitudes the pressure pattern is reversed, and air generally flows from land out to sea.

Once this moist air is over land, it undergoes convection. As the air rises and cools, condensation occurs, which greatly intensifies the monsoon through the release of latent heat. In effect, this condensation results in the solar energy put into evaporating liquid water in the tropical oceans being concentrated and released over land. This condensation is also responsible for the annual monsoon rains upon which hundreds of millions of people depend for their crops and ultimately their food. The intense and sustained uplift of air again creates a pressure gradient between land and sea, but this time with high pressure over land.

The final ingredient in the swirl introduced into its winds by Earth's rotation, which is most apparent at high altitudes. This swirl is one of the largest features in Earth's atmosphere and stretches from the Mediterranean ocean to the Sea of Japan east to west, and from Russia to the Equator north to south (Figure 1.3). This anticyclone has two main effects. The first is that its core is relatively isolated from the surrounding regions, and the second is that it mixes tropical and extratropical airmasses around its perimeter. Numerous other effects and feedbacks both positive and negative modulate the monsoon as it evolves throughout the late summer.

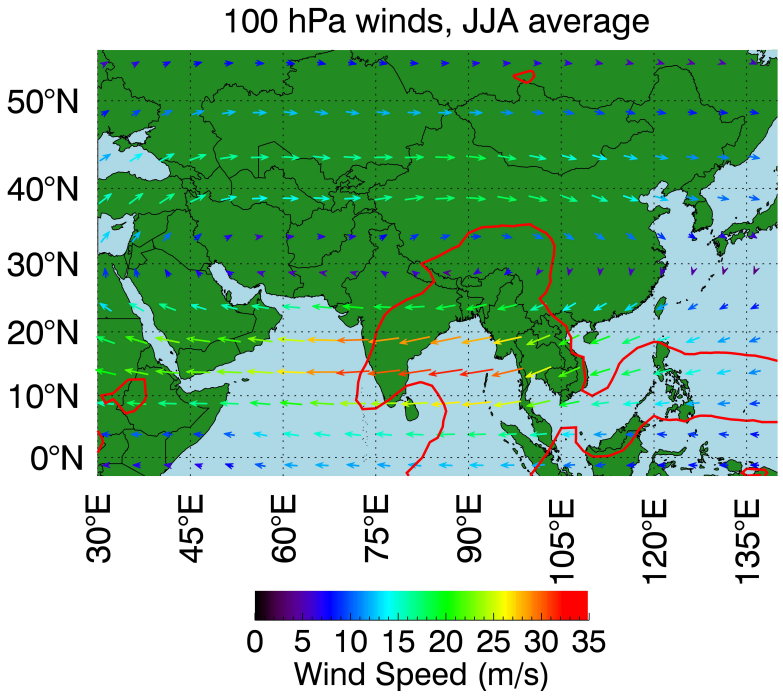

Figure 1.3: Average JJA winds at 100 hPa in the monsoon region. Regions outlined in red correspond to the areas with the least outgoing longwave radiation (OLR), which are generally taken to be the cold anvil tops of intense convective cells. The winds and maximum OLR regions are generated from NCEP reanalysis data.

Since the AM is so strongly associated with deep convection, it is thought to be one of the main pathways by which moisture enters the stratosphere. It may contribute up to 75% of the upward water vapor flux to the tropopause in northern hemisphere (NH) summer [Gettelman et al., 2004], and Kremser et al. [2009] claim it is the single largest

contributor to stratospheric water vapor. Figure 1.4 shows the relative contribution to stratospheric water vapor if $10 \times 5^{\circ}$ grid boxes during NH winter and NH summer. During summer the largest contributions is associated with monsoon convection. Understanding the extent and mechanism of this contribution is necessary because water vapor and cirrus are both important terms in Earth's radiation budget, and because the mechanism of transport affects the chemical mix of air reaching the stratosphere. Convection brings polluted air to altitude on a timescale of hours, whereas slow circulation upward in clear air takes days to weeks. Making in-situ measurements and profiles of water vapor isotopologues can help us understand convection and its importance in this region.

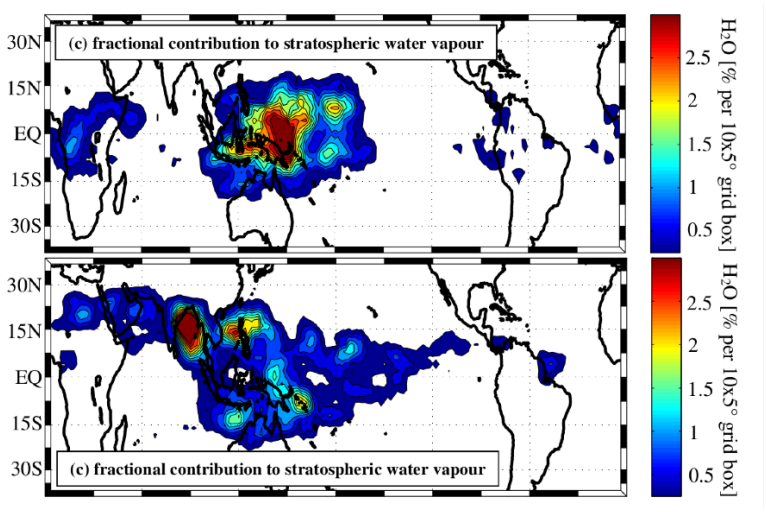

Figure 1.4: Water vapor concentrations to the stratosphere per $10 \times 5^{\circ}$ grid box during NH winter (*top*) and NH summer (*bottom*). Figure from Kremser et al. [2009]

Isotopic profiles in the atmosphere can be used to diagnose moisture fluxes. Figure 1.5 shows an isotopic profile plotted as potential temperature vs δD. The black dashed line represents the expected isotopic profile assuming Rayleigh fractionation occurs – as a parcel rises and cools all the water vapor that condenses precipitates out. This curve describes the average atmosphere reasonably well up to the TTL at about 350 K.

At this pont both tropical average profiles from the ATMOS satellite and in-situ measurements from the NAM over Costa Rica show deviations from Rayleigh fractionation. One reason for this is that in stratospheric air oxidation of CH_4 becomes a significant contribu-

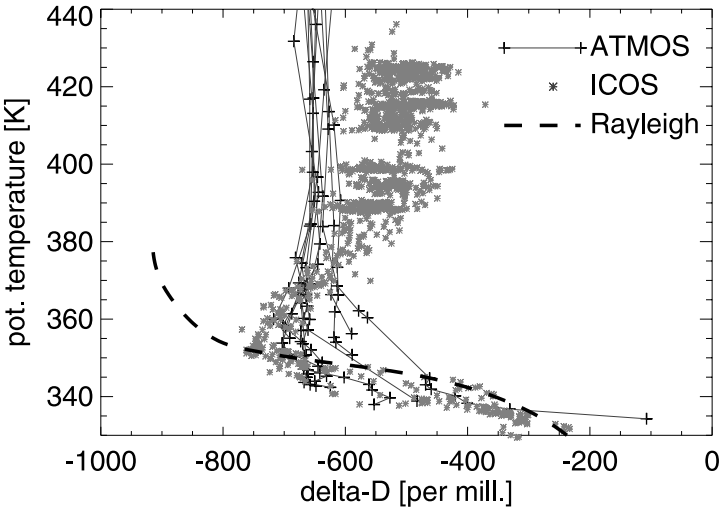

Figure 1.5: Isotopic profiles in the tropical UT/LS plotted as potential temperature vs δD. ATMOS satellite measurements are tropical averages, and in-situ measurements from the NAM come from the CR-AVE campaign. The black dashed line is the Rayleigh fractionation line which explains average profiles in the atmosphere reasonably well until about 350 K. Figure from Fueglistaler et al. [2009].

tion to the water vapor budget, and that process has its own isotopic signature. The other reason is that if ice lofted by deep convection is detrained into the dry stratosphere, it will evaporate and leave behind its signature by enhancing the isotopic ratio of the vapor, which can be seen in the CR-AVE data. The slope of this increase yields information about how important lofted ice, and by extension convection, is to the water budget of the UT/LS.

1.4 Role of Field Campaigns

Field campaigns provide a necessary check on theory and satellite measurements. Satellite measurements typically have far greater spatial and temporal coverage than in-situ measurements, but in-situ measurements can be performed at much higher resolution. Satellite retrievals are highly dependent on the factors such as the viewing geometry and assumptions about the measurement and retrieval algorithms, and as such are susceptible to biases. Field campaigns typically try to incorporate a set of measurements that overlap with a satellite retrieval, which provides a way to check retrieval bias and validate its uncertainties.

In-situ measurements can also easily be co-located with other types of measurements to construct a full and detailed picture of the properties of a particular airmass. Acquiring a full suite of simultaneous measurements including temperature, humidity, isotopic composition, trace gasses, particle size, and particle number can greatly increase the total value of all the measurements when taken together.

1.5 Outline of Thesis

Chapter 2 provides a review of the fundamental physics behind molecular absorption spectroscopy, and a brief treatment of 3 spectroscopic techniques used in this work to increase signal-to-noise ratio through longer pathlengths. In Chapter 3 results from cloud chamber studies in the AIDA cloud chamber at the Karlsruhe Institute of Technology showing no evidence of anomalous supersaturation and metastable ice are presented. This measurement campaign paved the way for the development and construction of the airborne version of the Chicago Water Isotope Spectrometer (ChiWIS), which is discussed in Chapter 4. An in depth treatment of the non-axially symmetric optics used to increase output collection efficiency is given in Chapter 5. Chapter 6 gives an overview of the Stratoclim campaign and its science goals, then discusses the AM field campaign, and finally describes the other water vapor instruments in the science payload.

CHAPTER 2

REVIEW OF MEASUREMENT TECHNIQUES

Absorption spectroscopy encompasses any experimental method which results in an absorption profile as a function of wavelength. The goal of such spectroscopy is often to extract the concentrations of one or more trace gasses in a gaseous sample [Hodgkinson and Tatam, 2013] or the temperature of the sample itself, e.g. [Farooq et al., 2008], but other fundamental quantities of a species such as line position and broadening widths are also of interest, e.g. [Toth and Brault, 1983]. Absorption profiles can be acquired with a broadband source and a monochromator that selects the detected wavelength, or more commonly with a tunable source of narrow frequency range. The advent of Tunable Diode Lasers (TDLs) with narrow line widths and high power densities has made the latter method much more common. Section 2.1 reviews the fundamentals of absorption spectroscopy and TDL sources, mainly following the works of Ebert and Wolfrum [2001] and Tittel et al. [2003].

In a situation where one wishes to measure an extremely scarce trace gas, such as water vapor at low temperatures, the most straightforward way to increase the measured absorption and maintain a high data acquisition rate is to increase the beam's path length within the instrument. Various methods exist to increase the path length, and can broadly be divided into open-path methods and cavity-enhanced methods. Three such methods used in the course of this research are described in section 2.2.

2.1 Tunable diode laser absorption spectroscopy

Tunable Diode Laser Absorption Spectroscopy (TDLAS) allows the retrieval of concentrations of one or more absorbing species from a gas sample. As a laser's emission frequency is tuned over a proscribed range, its light interacts more or less strongly with the absorbing species depending on its proximity to the absorber's spectral lines. These lines correspond to quantum mechanical transitions between energy levels of the molecule, and photons that

are close to the energy of a particular transition are more likely to be absorbed. If the sample's pressure, temperature, certain fundamental properties of the absorber, and laser beam path length are known, then a concentration can be extracted from the measured absorption profile of a spectral feature.

2.1.1 Molecular absorption spectra

Molecular absorption spectra are the result of quantum mechanical transitions of electrons between a molecule's energy levels. The spectra of molecules are significantly more complicated than those of atoms due to extra degrees of freedom introduced by the vibrations between constituent atoms and rotations. Typically electronic transitions are in the ultraviolet and visible range, vibrational transitions are in the near- to mid-infrared range, and rotational transitions are in the far-infrared range. In practice, rotational and vibrational transitions are coupled to each other because the vibration of a molecule changes its bond length which affects its moment of inertia[Svanberg, 2004]. Vibrational transitions are much more energetic than rotational ones, and observationally rotational transitions add 'fine structure' to vibrational transitions. The combinations of these transitions are referred to as ro-vibrational bands, and their obeservation is often called to as ro-vibrational spectroscopy. This section will briefly discuss the origin of the rotational and vibrational energy levels typically encountered in near- and mid-IR spectroscopy in the context of diatomic molecules, then discuss the extension of these ideas to the more complicated case of water.

Vibrational Transitions

Predicting the absorption spectra of a particular molecule requires a quantum mechanical treatment to find its energy eigenstates. For individual atoms and simple molecules, the energy states can be written out analytically, but more complicated molecules require numerical simulations in order to be comparable to obeservations. Figure 2.1 shows a schematic of the energy levels for molecules and the typical energy level spacings for electronic, vibrational,

and rotational transitions. Electronic transitions are typically found in the UV and are not discussed here.

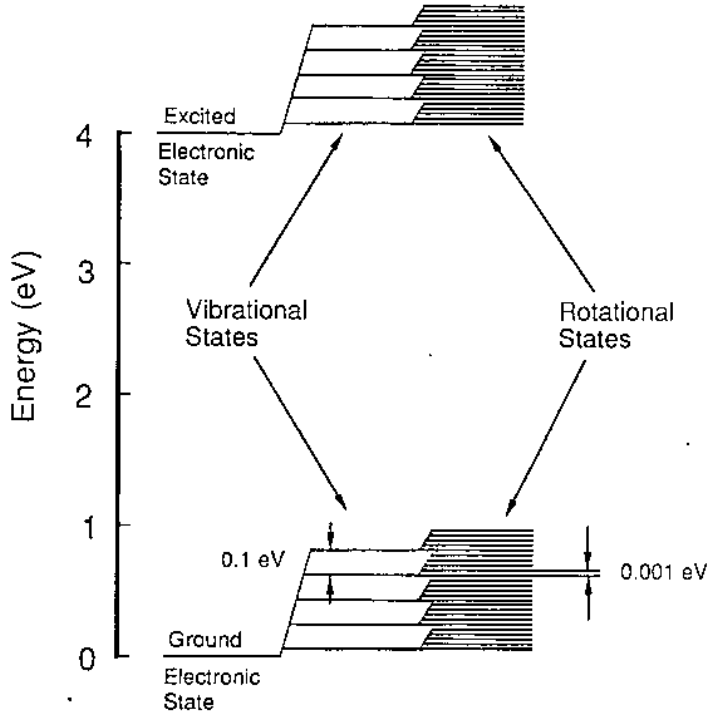

Figure 2.1: Schematic of the energy level structure of a molecule. Rotational energy levels are typically separated by about 0.001 meV, and vibrational energy levels by about 0.1 eV. Figure from Svanberg [2004].

A diatomic molecule's potential energy can be described in a variety of ways, but the Morse potential is one common method:

$$V(r) = D\left(1 - e^{-\alpha(r-r_0)}\right)^2 \tag{2.1}$$

Here D is the dissociation energy and r_0 is the equilibrium separation of the atoms in the molecule. Although an exact quantum mechanical solution for the allowed energy levels of this potential is available [Morse, 1929], for most applications it is sufficient to Taylor

expand the potential around $r = r_0$, which yields

$$V(r) \approx D\alpha^2 (r - r_0)^2 . \tag{2.2}$$

This is the form of the familiar harmonic oscillator and can be easily treated within the framework of quantum mechanics to give an approximation to vibrational energy levels close to equilibrium. It can deviate significantly from the better approximation given by the Morse potential at higher energy levels and does not capture the dissociation energy of molecules.

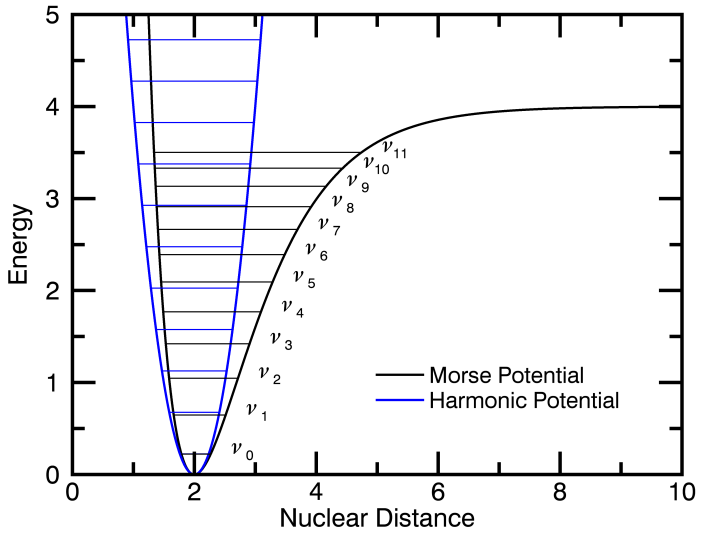

Figure 2.2: Comparison of Morse and harmonic potential energy levels. Here $\alpha = 1$, $\hbar = 1$, and $D = 4$. The spacing between Morse potential energy levels decreases as the quantum number increases, but stays constant for the harmonic potential.

Working in the harmonic oscillator approximation, the interatomic force is approximated by $F(r) = -k(r - r_0)$, and the frequency of the oscillator is given by $\omega = \sqrt{k/m} = \sqrt{2D\alpha^2/\mu}$, where μ is the reduced mass of the atoms and k is the force constant. The allowed vibrational energy levels are

$$E_\nu = \hbar\omega \left(\nu + \frac{1}{2}\right), \qquad \nu = 0, 1, 2, ... \tag{2.3}$$

The transition from $\nu = 0$ to $\nu = 1$ is called the fundamental transition, and all transitions from the ground state to higher levels are called overtones. Anharmonic terms can be included as necessary to better approximate the observed energy levels of a molecule, and in that case the observed energy levels take the form

$$E_\nu = hc\omega_e \left[\left(\nu + \frac{1}{2} \right) - x_e \left(\nu + \frac{1}{2} \right)^2 + y_e \left(\nu + \frac{1}{2} \right)^2 + ... \right]. \tag{2.4}$$

Here $\omega_e = \omega / (2\pi c)$ and is given in units of wavenumbers. The anharmonicity coefficients x_e and y_e are dimensionless constants and can be found in the literature along with ω_e. A schematic example is given in Figure 2.2 of the typical differences in energy levels between the harmonic potential and an anharmonic one, in this case the Morse potential. Deviations from the harmonic energy levels are typically small for low values of the quantum number.

For polyatomic molecules of the form AX_2 like water, there are three fundamental vibrational modes, the symmetric stretch, bend, and asymmetric stretch, which are denoted by the independent quantum numbers ν_1, ν_2, and ν_3. In the case of water, the fundamental transition energies are 3657 cm^{-1}, 1595 cm^{-1}, and 3756 cm^{-1}, respectively. The two stretching modes have nearly the same transition energies, the result of which is that their associated ro-vibrational spectra significantly overlap.

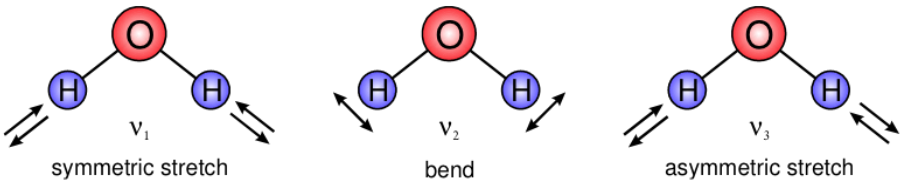

Figure 2.3: The water molecule has three fundamental vibrational modes, the symmetric stretch (ν_1), the bend (ν_2), and the asymmetric stretch (ν_3). Transition energies for H_2O and HDO are given in Table 2.1. Figure from Skrotzki [2012a].

Each atom in a molecule has 3 degrees of freedom due to the 3 coordinates necessary to describe its position, so a molecule with N atoms has $3N$ total degrees of freedom. Of

Table 2.1: Energies for the fundamental transitions of H_2O and HDO. Energies are given in wavenumbers (cm^{-1}). Values from Tennyson et al. [2009, 2010, 2013].

Isotopologue	ν_1	ν_2	ν_2
H_2O	3657.1	1594.7	3755.9
HDO	2723.7	1403.5	3707.5

these, three correspond to rotation about the inertial axes of the molecule, and another three describe the translational motion of the atoms, so in general a molecule has $3N - 6$ vibrational degrees of freedom, unless it is a linear molecule, in which case it has $3N - 5$ degrees of freedom since there are only two independent rotational axes.

Rotational Transitions

Diatomic molecules can be modeled as elastic rotors, where the molecules moment of inertia increases in the higher rotational states, decreasing the energy slightly from that found for a rigid rotor. If a rotating molecule is composed of atoms with masses m_1 and m_2, which are distances r_1 and r_2 from the center of mass, respectively, then its moment of inertia can be written as $I = \mu r^2$, where μ is the reduced mass and r is the distance between the atoms. Classically the angular momentum $\mathbf{L} = I\omega/\hbar$ is related to the energy by

$$E = \frac{\mathbf{L}^2\hbar^2}{2I}, \tag{2.5}$$

where ω is the angular frequency. In quantum mechanics, the $\mathbf{L}$ operator is given by

$$|\mathbf{L}| = \sqrt{J\,(J+1)}, \qquad J = 0, 1, 2, ... \tag{2.6}$$

and therefore the quantized energy states of a rigid rotor are given by

$$E_J = \frac{\hbar^2}{2I} J\,(J+1) = BJ\,(J+1) \tag{2.7}$$

Elasticity of the atomic bonds under rotation can be accounted for in the rotor's energy by

$$E_J = BJ\left(J+1\right) - DJ^2\left(J+1\right)^2 \tag{2.8}$$

Here D is a positive constant that is very small compared to B. Referring back to equation 2.7 shows that for a given quantum number, increasing the moment of inertia must decrease the energy of the rotor.

The coupling between the rotational and vibrational modes occurs because higher vibrational modes increase the moment of inertia of the rotating molecule. This can be accounted for by writing

$$B = B_e + \alpha_e\left(\nu + \frac{1}{2}\right), \tag{2.9}$$

where B_e and α_e are both constants particular to the molecule in question. Combining equations 2.9 and 2.8 yields the full expression for the rotational energy levels:

$$E_j\left(\nu\right) = \left[B_e + \alpha_e\left(\nu + \frac{1}{2}\right)\right] J\left(J+1\right) - DJ^2\left(J+1\right)^2. \tag{2.10}$$

The constants B_e, α_e, and D are available for many molecules in the literature.

As for the vibration modes, each rotational degree of freedom is associated with a quantum number. The quantum number J still refers to the total angular momentum, but the other two rotational quantum number generally cannot be expressed in closed form for asymmetric rotors like the water molecule.

Ro-vibrational bands of water

The ro-vibrational band structure is very complex, and covers a broad range of wavelengths, from millimeters to hundreds of nanometers. This complexity arises from the polyatomic nature and permanent dipole of the water molecule, combination bands, and Fermi resonances, to name a few. Figure 2.4 shows the ro-vibrational bands of the 5 most common water iso-

topologues. The High Resolution Transmission database for spectroscopy (HITRAN) [Gordon et al., 2017] linestrengths in units of $cm^{-1}/\left(molecule \cdot cm^{-2}\right)$ of lines between 1000 and 10000 cm^{-1} are plotted against the linecenter wavenumber. The energies of stable electronic excited states are higher than the dissociation energy of the molecule, so absorption occurs in the ground electronic state [Barber et al., 2006].

The complexity of water's ro-vibrational spectra is not just due to its being an asymmetric rotor, but also to its own peculiarities as a molecule. The low mass of hydrogen implies small moments of inertia about the rotational axes, and large rotational constants (cf. equation 2.7). The rotational energy level spacings for a rigid rotor are twice the rotation constant, which explains the very broad rotational features of water's absorption spectrum.

Similarly, the hydrogen atoms often vibrate far from equilibrium, making the anharmonic contributions to the molecule's vibrational spectrum important, and allowing quantum transitions in which more than one quantum number changes.

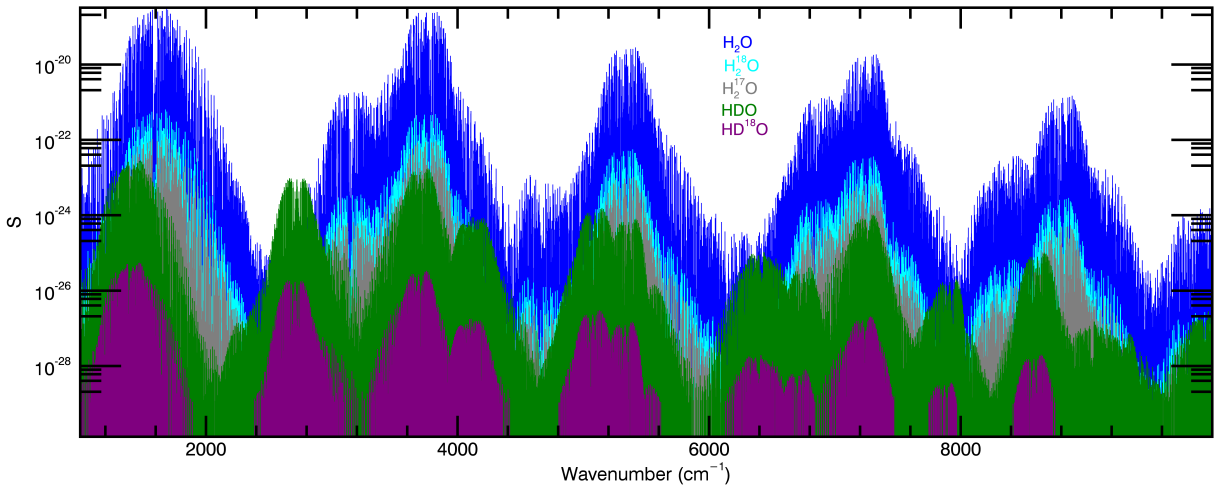

Figure 2.4: Ro-vibrational water bands in the near-and mid-IR for the 5 most common water isotopologues. HITRAN linestrengths ($cm^{-1}/\left(molecule \cdot cm^{-2}\right)$) are plotted against the line center wavenumbers. Linestrengths are scaled by the natural abundance of the isotopologue. Higher wavenumber (shorter wavelength) bands are overtones and combinations. ChiWIS operates at around 3777 cm^{-1} to access the strong HDO lines in that region.

2.1.2 Linewidth broadening

The absorption of photons associated with a particular energy transition typically happens over a range of wavelengths. This linewidth broadening is the result of several processes. Natural broadening is due to the finite lifetimes of energy transitions, and is therefore intrinsic to the molecules. Doppler and collisional broadening depend on characteristics of the molecules environment such as temperature, pressure, and the presence of other molecules. The following subsections discuss common broadening mechanisms and their application to observable line profiles.

Natural Broadening

A transition's natural linewidth is a consequence of the Heisenberg uncertainty principle, $\Delta E \cdot \Delta t \approx \hbar$. The value of Δt corresponds to the natural lifetimes of the upper and lower states involved in the transition, and results in a Lorentzian lineshape with natural linewidth[Graybeal, 1993]

$$\gamma_{nat} = \frac{1}{\pi}\left(\frac{1}{\tau_u} + \frac{1}{\tau_l}\right) \tag{2.11}$$

where τ_u and τ_l are the lifetimes of the upper and lower states. In the mid-infrared lifetimes are comparatively long and the natural linewitdths are several orders of magnitude smaller than the Doppler widths. Typically on the upper state lifetime is considered.

Doppler Broadening

Doppler broadening is due to the random thermal motions of molecules in a gas sample. Molecules moving towards the source of the laser beam absorb at a slightly higher frequency and those moving away at a slightly lower frequency. If a sample of gas is in thermal equilibrium at a temperature T, the thermal motion of its molecules is given by the Maxwell-Boltzmann distribution. The Doppler shifts resulting from this motion results in

an absorption profile with Gaussian shape and its width is given by:

$$\gamma_D = \left(\frac{\nu_0}{c}\right) v_p \sqrt{\ln 2} = \left(\frac{\nu_0}{c}\right) \sqrt{\frac{2kT \ln 2}{m}} \tag{2.12}$$

where $v_p = \sqrt{2kT/m}$ is the most probable velocity, m is the mass of the molecule, k is Boltzmann's constant, c is the speed of light, and ν_0 is the line center frequency.

Collisional Broadening

Collisions between molecules during photon absorption can affect the lifetimes of excited states, and therefore also the observed energy of the transition. This results in line broadening with a Lorentzian shape, in the same manner as natural broadening. Collisional broadening is highly dependent on the species involved, the quantum states of both the perturber and absorber, and the the pressure of the sample, but for the purposes of spectroscopy can usually be divided into Lorentz broadening (the result of collisions between the target species and another molecule), and Holtsmark broadening (the result of a collision between two molecules of the target species)[Svanberg, 2004]. Lorentz and Holtsmark broadening are often commonly called foreign and self-broadening, respectively. The broadening coefficient is given by:

$$\gamma_C = \left(\gamma_{C0_{self}} \cdot \frac{p_{self}}{p_0} + \gamma_{C0_{foreign}} \cdot \frac{p_{foreign}}{p_0}\right) \left(\frac{T_0}{T}\right)^s \tag{2.13}$$

Here p_0 and T_0 are typically standard pressure and temperature, the γ_{C0}'s are the self- and foreign broadening coefficients at STP, and p_{self} and $p_{foreign}$ are the partial pressures of the target species and another species, respectively. The self-broadening coefficient is typically larger than the foreign broadening coefficient, but can often be neglected in trace gas measurements due to the very low partial pressures of the target species. The exponent s describes the temperature evolution of the broadening coefficients.

Mixed Line Shapes

In many applications in Earth's atmosphere, neither Doppler nor collisional broadening completely dominates the lineshape, and the observed absorption profile is a mix of both effects. This is true in the measurements taken during the StratoClim Campaign, in which typical doppler broadenings are about 0.005 cm^{-1}, and typical collisional broadenings are about 0.004 cm^{-1}. The most straightforward treatment of this mixing is to assume that the lineshape is given by a Voigt function, which is the convolution of the Gaussian and Lorentzian functions. This function does not have an analytical form, although it is well tabulated and studied[Faddeyeva and Terentev, 1961, Armstrong, 1967], and can be well-approximated computationally[Humlíček, 1982].

The Voigt line shape is typically given by:

$$g_V = \int_{-\infty}^{+\infty} g_D\left(\nu'\right) g_C\left(\nu - \nu_0 - \nu'\right) d\nu' \tag{2.14}$$

Although this shape has no explicit representation, it can be approximated by[Whiting, 1968]

$$\begin{aligned} \frac{g_V}{l_{g_V}} &= \left(1 - \frac{\gamma_C}{\gamma_V}\right) \exp -2.722 \left(\frac{\nu - \nu_0}{2\gamma_V}\right)^2 + \frac{\gamma_C \gamma_V}{\gamma_V^2 + (\nu - \nu_0)^2} \\ &+0.016 \frac{\gamma_C}{\gamma_V}\left(1 - \frac{\gamma_C}{\gamma_V}\right)\left(\exp -0.4 \left(\frac{|\nu - \nu_0|}{2\gamma_V}\right)^{2.25} - \frac{10}{10 + \left(|\nu - \nu_0| / (2\gamma_V)\right)^{2.25}}\right) \end{aligned} \tag{2.15}$$

where

$$l_{g_V} = \frac{1}{2\gamma_V\left(1.065 + 0.477\gamma_C/\gamma_V + 0.058\left(\gamma_C/\gamma_V\right)^2\right)} \tag{2.16}$$

The Voigt width at half-width half-max is given by[Olivero and Longbothum, 1977]

$$\gamma_V = 0.5346\gamma_C + \sqrt{0.2166\gamma_C^2 + \gamma_D^2} \tag{2.17}$$

These equations are generally not suitable for extracting concentrations for observed spec-

tra, but are computationally very fast compared to other methods used to generate sample spectra, and therefore are useful tools for quickly exploring unfamiliar spectral regions.

Although this relatively straightforward treatment of lineshape mixing is generally sufficient for atmospherics measurements, it can be extended to take into other effects and generate a more accurate lineshape. In ChiWIS's StratoClim measurements, typical Voigt broadenings are about 0.008 cm^{-1}.

2.1.3 Beer-Lambert Law

The extinction of light passing through an absorbing medium is given by the Beer-Lambert law

$$I(\nu, x) = I_0 e^{-k(\nu)\cdot x}, \tag{2.18}$$

where I_0 is the intensity of the light before it enters the absorbing medium, $k(\nu)$ is the linear absorption coefficient, and x is the distance traveled through the medium. The linear absorption coefficient is related to the absorption cross section by $k(\nu) = \sigma(\nu) c$, where $\sigma(\nu)$ is the absorption cross section and c is the absorber concentration in number per unit volume. Absorption depends on the presence of absorbers in the lower energy level of the transition. In cases where there are not many absorbers in that state, or the state becomes depleted, the absorption coefficient may no longer be linear. That can occur at long wavelength where the lifetime of the excited state is long, or when intense radiation depopulates the lower state.

Concentrations can be extracted from absorption profiles by recognizing that the optical depth of the absorption medium is bound by the following relationships:

$$-\ln\left[\frac{I(\nu, x)}{I_0(\nu)}\right] = k(\nu) x = S(T) \cdot g(\nu - \nu_0) \cdot x \cdot n, \tag{2.19}$$

where $S(T)$ is the line strength, $g(\nu - \nu_0)$ is the normalized absorption profile, and n is the absorber concentration. Once the optical depth as a function of wavelength has been measured, it can be integrated to remove the lineshape (which is normalized to one) and

wavelength dependence, which yields the absorber concentration:

$$-\frac{1}{S\left(T\right)x}\int_{-\infty}^{+\infty}\ln\left[\frac{I\left(\nu,x\right)}{I_0\left(\nu\right)}\right]\mathrm{d}\nu = n \tag{2.20}$$

This equation implies the need for several pieces of information beyond just an absorption profile. The first is a tuning curve, which relates measurement time of a sample to the laser frequency at that time. This is typically accomplished by incorporating an etalon of known free spectral range into an instrument on a reference channel, then extracting $\nu\left(t\right)$ from that (see Section 4.2.8). In practice the limits of integration obviously do not extend to infinity, and usually only extend far enough to allow a good estimate of the baseline necessary to extract the optical depth from the absorption profile. In theory, full knowledge of the spectral features present and the reference power, $I_0\left(\nu\right)$, should suffice, but in practice many effects can confound an accurate estimate of the baseline. In open-path measurements (cf. Sections 2.2.1 and 2.2.2), the measured spectra can often be divided by power reference to remove unwanted curvature, correlated features, and certain types of noise from the data. From this divided data, a fit routine can estimate the baseline. In cavity enhanced methods such as ICOS (Section 2.2.3), the situation is somewhat more complicated, and the baseline must be estimated through software. This estimation proceeds best in spectra taken at lower pressures, where the absorption lines tend to be narrower, since this leaves more space with little or no absorption between the features. If it is present, optical fringing comparable to or greater than the width of the spectral features is also a major source of uncertainty in finding the correct baseline.

2.1.4 Tunable Diode Lasers

High quality laser sources have revolutionized trace gas measurements of isotopes and isotopolgues. In the broadest possible terms, every laser consists of some cavity filled with a gain medium, which amplifies input power by stimulated emission. For trace gas measure-

ments, the most important characteristics of a laser are its monochromicity and its tunability. Although no laser can be truly monochromatic, it is important that the spectral linewidth be significantly narrower than the spectral features to be measured. Tunability is necessary in order to sweep over the spectral features and build up a full absorption profile.

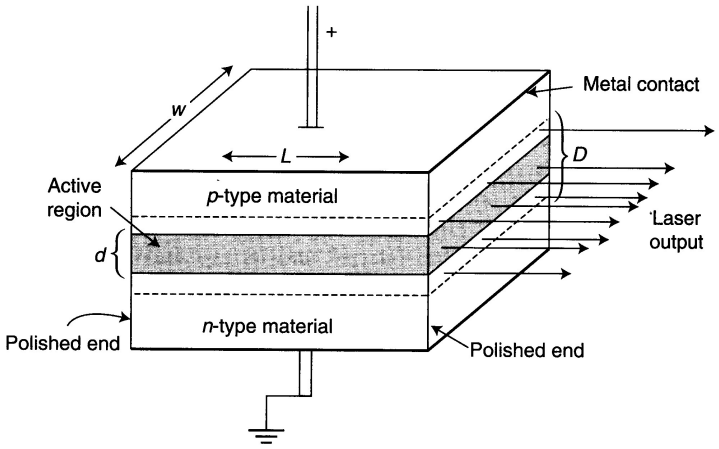

Figure 2.5: Schematic diagram of a diode laser junction. Current flows through the active region of the *pn* junction, generating electron-hole pairs. These radiatively recombine, and beyond a threshold current result in positive feedback. Power buildup is promoted by the high reflectivity off the two polished faces of the junction. Figure from Milonni and Eberly [2010].

Diode lasers are biased *pn* junctions in which the radiative recombination of electrons and holes stimulates the recombination of more electron-hole pairs. These devices are closely related to light-emitting diodes (LEDs). An injection current through the junction results in enough electron-hole pairs to produce gain, which is emitted through the polished sides of the semiconductor. (The other sides are left rough to discourage buildup of power along those axes.) Reflection back through the gain medium is accomplished through Fresnel reflection at the semiconductor-air boundaries on the polished faces, which relies on the large index of refraction typical of semiconductors.

Distributed Feedback Diode Lasers

Distributed Feedback (DFB) diode lasers are fabricated to have a periodic feature running

along their active layer, which acts a a grating. Feedback and reflection occur throughout the gain medium in this method, and the spatial period of the grating selects the wavelength of the light to be emitted. These types of lasers are easily tunable using the diode temperature and injection current, and have excellent wavelength stability.

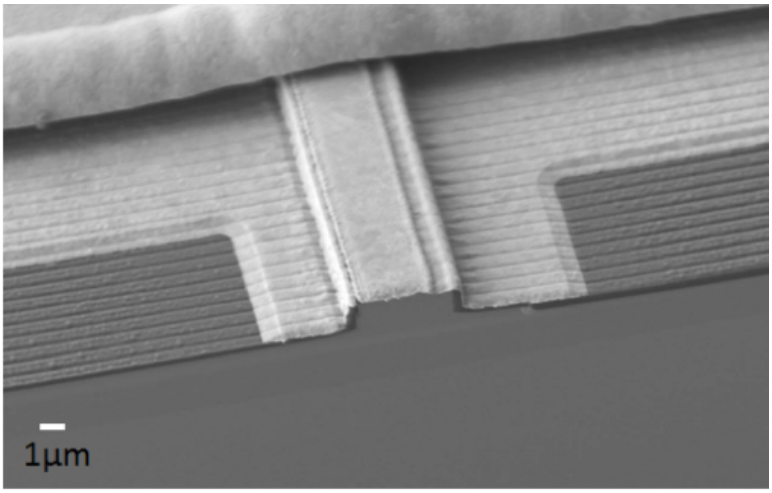

Figure 2.6: A scanning electron microscope image (SEM) of a DFB laser fabricated by the Microdevices Laboratory (MDL) at the jet propulsions laboratory. After fabrication, the lateral grating is written into the surface using electron-beam lithography. Image courtesy of Mathieu Fradet and the MDL.

2.1.5 Comparison to other methods

Until the advent of high quality laser sources, mass spectrometry was the main source of high quality measurements of isotopic abundances. Isotope Ratio Mass Spectroscopy (IRMS) works by generating and accelerating ions into a magnetic field, which bends their trajectories along paths of radii $r = \sqrt{2Vm/B^2q}$, where V is the accelerating voltage, B is the magnetic field, m is the mass of the ion, and q is its charge. Upon leaving the magnetic field the ions have be separated by their momenta, and can be observed individually by adjusting the position of a collector.

High-quality mass spectrometry can provide measurements of D/H ratio with sensitivity of roughly 100 ppt, which is more than two orders of magnitude better than spectroscopic

methods. However, mass spectrometers are typically large and heavy, preventing easy use in the field. Thus samples are typically collected in the field and brought back to the spectrometer, which prevents a high data acquisition rate. Furthermore, measurements of gas samples are for the most part infeasible using IRMS.

2.2 Long-path optical cells

This section provides brief description of the spectroscopic techniques used in the course of this research. Each of these methods uses carefully placed mirrors to increase the pathlength of light through a gas. White cells and Herriott cells are open path techniques, and ICOS is a cavity-enhanced technique.

2.2.1 White Cells

The White cell[White, 1942] is a method of increasing the path length of light through an absorbing medium using a set of three concave, spherical mirrors with the same focal length. These mirrors are arranged as in Figure 2.7 so that the centers of curvature of the far mirrors (A and A$'$) are on the surface of the field mirror (B), and the center of curvature of the field mirror is halfway between the far mirrors. This configuration exploits the fact that if an object is placed close to the center of curvature of of a mirror, its image will appear equidistant to the center, but on the opposite side. For example, in Figure 2.7 point 1 is the same distance from the center of mirror A as the source is, and point 2 is the same distance from the center of mirror A$'$ as point 1 is. The result is that the source will be continually imaged onto the field mirror until it 'walks' off the mirror at a proscribed location and into the detector, denoted by point 4 in Figure 2.7.

Since the two far mirrors are placed equidistant from the center of the field mirror, it will continually alternate forming images on them, regardless of where their centers of curvature are on the field mirror. The only requirement is that the source is correctly pointed at the

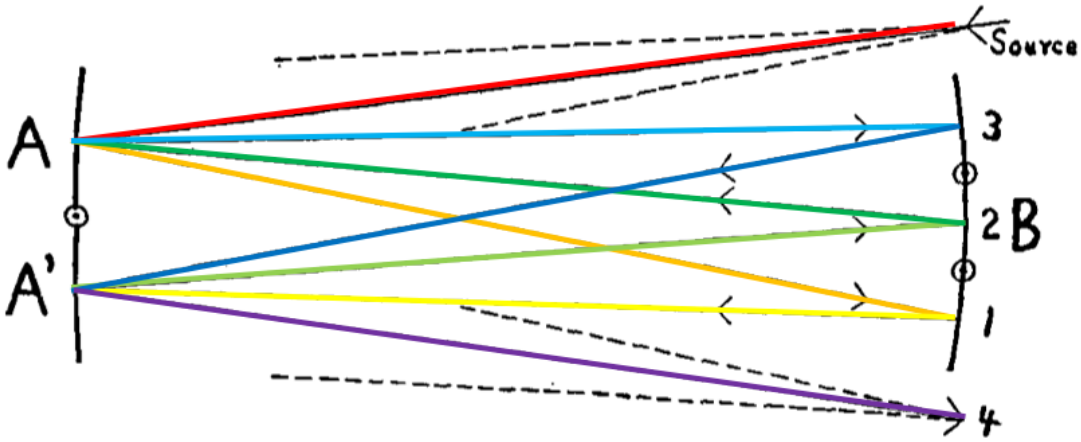

Figure 2.7: Schematic of a White cell showing the field mirror and two far mirrors. Figure adapted from White [1942]. The beam traces its path through the cell in the following order: red-orange-yellow-light green-dark green-light blue-dark blue-purple. The dot with a circle on the left is the center of mirror B, and the dot with circles on the right are the centers of mirrors A and A′.

first far mirror. The number of passes through the cell can easily be controlled by changing the orientation of the far mirrors, which changes the positions of their centers of curvature on the field mirror. This is a great strength of White cells, that their path length can be changed in a matter of minutes, which can be very useful in situations where a large range of concentrations are to be measured. This method of achieving longer optical path lengths is also very robust against small misalignments and can accept beams of high numerical aperture.

White cells are usually intentionally slightly misaligned in the vertical direction. This causes successive images on the field mirror to be raised and lowered with respect to their original positioning. This misalignment allows for more images to be packed onto the field mirror and longer path lengths to be achieved. With an appropriately placed set of diagonal mirrors, the number of passes through the cell can be increased by about a factor of 2 [White, 1976]. The mirrors are placed so that the spot pattern walks back across the field mirror, making a rectangular array of spots with 4 rows. This arrangement also place the exit beam near the entrance, which can be useful in the design of compact instruments.

2.2.2 Herriott Cells

Herriott cells[Herriott et al., 1964] use two spherical, concave mirrors with identical focal lengths to achieve long optical path lengths. These mirrors are placed on the same optical axis at opposite ends of an absorption cell. For paraxial rays, the equations governing reflections off of concave mirrors take the same form as the thin lens equation, so the cell can be analyzed as a series of co-axial thin lenses with the same focal length as the mirrors. With this approximation, Herriott derived the reentrant conditions on the position and angle of a beam entering the cavity through a hole in one of the mirrors that ensure the beam leaves the cell through the same hole after some number of passes through the cell.

The reentrant conditions are defined by the Herriot cell's geometry, and the three relevant parameters are A, the spot pattern radius; d the separation between the mirrors; and f the focal length of the mirrors. In Cartesian coordinates, the reentrant conditions are:

$$\vec{x} = \left(A\sqrt{\frac{d}{4f}}, A\sqrt{1 - \frac{d}{4f}}, 0 \right) \tag{2.21}$$

and

$$\vec{x'} = \frac{1}{\sqrt{1 + \frac{A^2}{fd}}} \left(\frac{-A}{\sqrt{fd}}, 0, 1 \right) \tag{2.22}$$

Note that equation 2.22 differs from the condition given in Herriott et al. [1964] in that it has been normalized to be a unit vector. After each pass through the cell, the beam has rotated through an angle θ given by:

$$\cos\theta = 1 - \frac{d}{2f} \tag{2.23}$$

A given Herriott geometry, defined by its ratio $u = f/d$, corresponds to a particular number of passes through the cell before the reentrant condition is met. The number of

passes is given by:

$$2\theta\nu = 2\pi\mu \tag{2.24}$$

where $\mu, \nu \in \mathbb{Z}$ and $\mu \neq \nu$. ν corresponds to the number of spots per mirror before one complete rotation through 2π radians is achieved, and μ is the number of complete cycles through 2π radians before the reentrant condition is achieved. So, for a given Herriott geometry, the number of passes before the reentrant condition is given by $N = 2\nu\mu$. In theory each geometry u has a unique number of passes associated with it, but in practice N is limited by the size of the reentrant hole necessary to accommodate the beam.

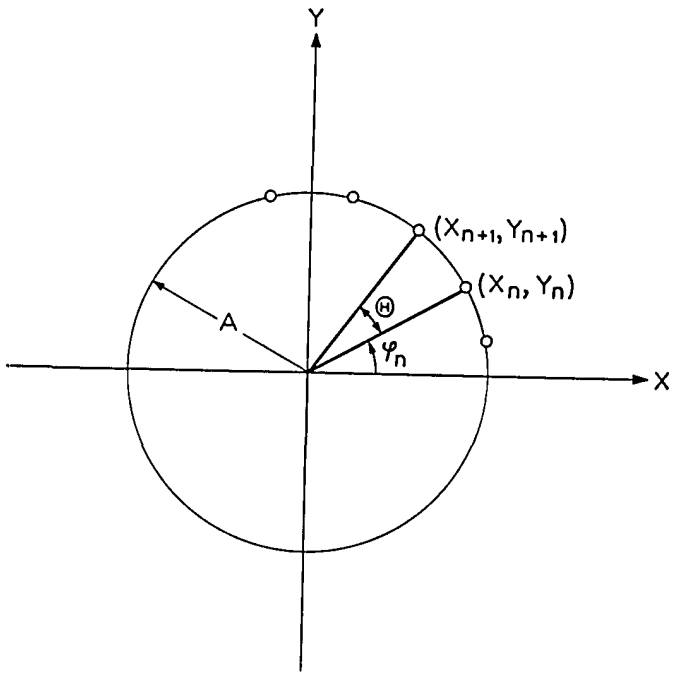

Figure 2.8: This figure, adapted from Herriott et al. [1964], shows the projection of subsequent spots in a Herriott cell onto a plane perpendicular to the optical axis. Subsequent spots are separated by an angle θ, which is determined by the relationship $\cos\theta = 1 - d/2f$. A is the radius of the circular Herriott spot pattern, and ϕ_n is the angle of the nth spot from the x-axis.

In the Herriott geometry the mirror distance must be less than four times the mirror focal length to ensure a stable beam pattern. Beyond this threshhold the configuration is unstable and the beam will eventually walk off the mirror. The reentrant conditions given in equations 2.21 and 2.22 are based on the thin lens approximation, and should be treated

with care, especially for mirrors with shorter focal lengths or especially wide spot patterns. Varying the radius of a circular spot pattern changes the effective distance between the mirrors, and the effective focal length due to spherical abberation. Engel and Moyer [2007] take into account these deviations into account to derive exact equations for the Herriott cell geometry.

The path length inside a Herriott cell can be increased by a variety of methods, but using spherical mirrors with a degree of astigmatism [Herriott and Schulte, 1965] is one of the most common. Herriott cells often have path lengths in the range of tens to hundreds of meters, but path lengths are limited in two main ways. The first is by the minimum achievable spot size on the cell mirrors. The mirror's beam hole should be large enough to easily pass the beam without clipping, and small enough so that radiation from adjacent spots is at a minimum, as this unwanted light can cause fringing. The second limitation is due to the stability of the cell. Although Herriot cells are more stable than White cells, after many passes through the cell the instability due to vibrations can result in large variations in the spot position. This can become a problem for cells with long path lengths and many mirror reflections. Equation 2.23 can be used to estimate a Herriott cell's sensitivity to variations in length due to vibration. Assuming the length variation is the same for all reflections (a safe assumption for thermal variations, situationally dependent for vibrational variations), the variation in θ for variations in mirror separation d is given by

$$\delta\theta = -\frac{\delta d/d}{\sqrt{1-4f/d}} \tag{2.25}$$

This equation indicates that the nth spot has moved a distance of roughly

$$\delta s = -nA\left(\frac{\delta d/d}{\sqrt{1-4f/d}}\right) \tag{2.26}$$

from its original position. For a Herriot cell like the one described in Lamb [2015] with $d = 1.00$ m, $f = 0.84$ m, $A = 45.5$ mm, and 86 spots per mirror, a length variation of 1 part

in 1000 results in about 5 mm of motion in the beam by the time it is exiting the cell, which is enough for the beam to miss the entrance/exit aperture. For cell with an aluminum tube, such a variation could be caused by a $\approx 40^\circ$ C change in temperature, with an invar cell the same deviation would require a nearly $\approx 830^\circ$ C change in temperature.

2.2.3 Integrated Cavity Output Spectroscopy

ICOS cells have the same geometry and alignment as Herriott cells, but do not have an entrance/exit aperture for the beam. This configuration is inherently low power since laser light must be injected through the cell mirrors (typically $R \sim 99.98\%$), and consequently most of it is reflected away. However, the light that does enter the cell can have extremely long effective path length 5000 to 10000 times the length of the cell. This section will briefly summarize the principle of this measurement technique.

ICOS is a type of Cavity Ringdown Spectroscopy (CRDS), and can be aligned to operate as such. The technique was developed independently by Engeln et al. [1998] and O'Keefe [1998], and has since been applied to trace gas measurements from ground level up to the stratosphere [Hodgkinson and Tatam, 2013]. The Herriott cell alignment of the cavities means that many passes through the cell occur before the reentrant condition is met, and the optical properties are similar to Fabry-Perot interferometer with length $2nL$ [Paul et al., 2001], where n is the number of mirror spots before the reentrant condition is met and L is its length. This analogy provides an avenue by which to understand the behavior of an ICOS cavity.

The long path length in the cell before the reentrant condition means that the cavity has an extremely short free spectral range (FSR). The FSR of an optical cavity is the distance in frequency space between its transmission modes. For example, a 90 cm cavity with 312 passes before the reentrant condition is met has an FSR of $\sim$ 500 kHz. If the linewidth of the laser is wider than the cavity FSR, then the laser excites several cavity modes at the same time. The effect of this is that the cavity transmits power through several modes

simultaneously, averaging the laser power. Provided the cavity FSR and laser linewidth are both much less than the width of any absorption features to be measured, then distortion of an absorption feature's line shape from either of these will be negligable.

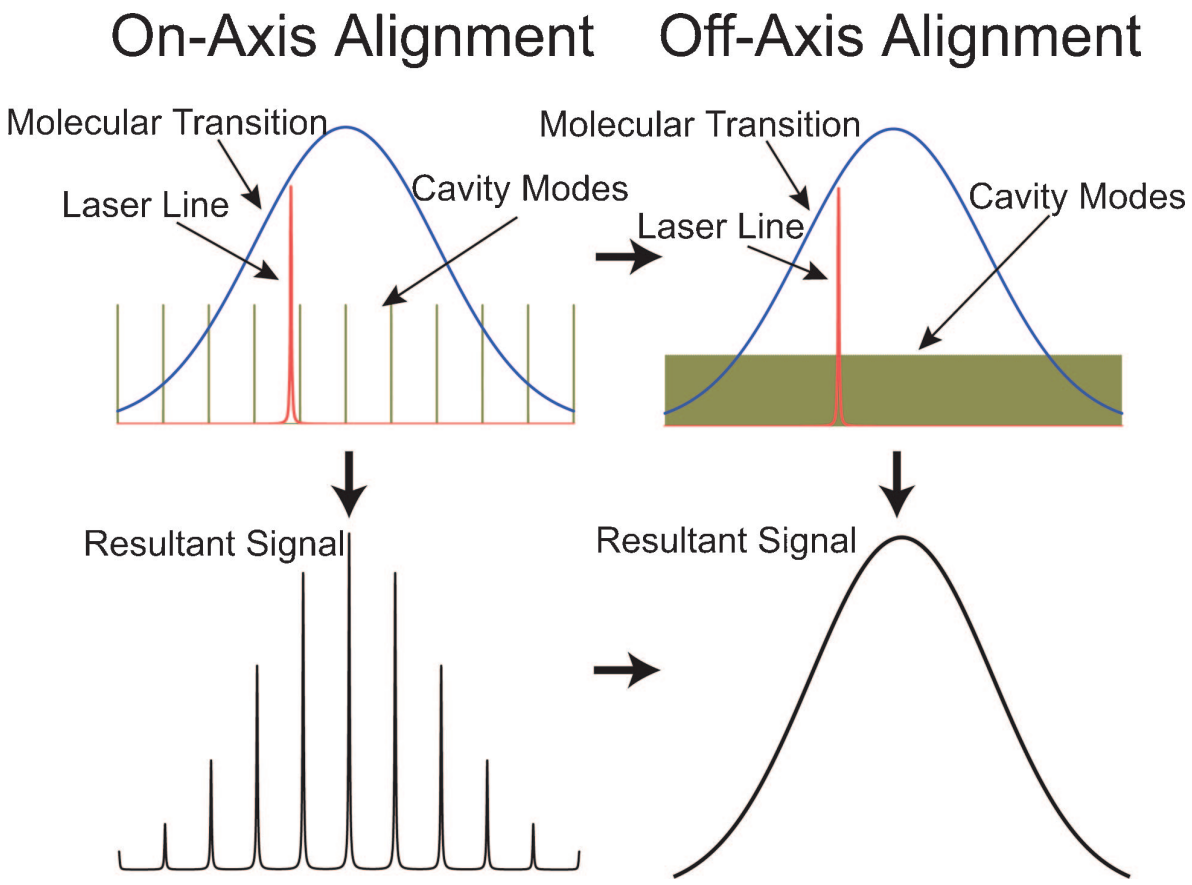

Figure 2.9: This figure, adapted from Engel et al. [2006], shows the effective transmission across an absorption feature of a cavity for an instrument aligned on-axis (left) and off-axis (right). The dense cavity-mode structure of an off-axis ICOS instrument means that absorption features can be observed continuously and without distortion provided the laser linewidth is much narrower than the absorption feature.

Cavities with high reflectivities can have effective path lengths of as much as ten kilometers, and in-cavity light residence times longer than 20 microseconds. The amount of time that light spends in the cavity on average is given by the cavity time constant

$$\tau = \frac{L}{c\,(1-R)}. \tag{2.27}$$

If an absorber is present in the cavity, then the time constant becomes

$$\tau = \frac{L}{[1 - R + \alpha(\nu)]} \tag{2.28}$$

and the cavity time constant decreases.

Unlike CRDS, in which measurements of τ at a series of wavelengths are used to construct absorption spectra, in ICOS a laser is frequency-tuned across the absorption features of interest, which results in a continuous absorption spectrum at the detector. However, the observed absorption spectrum at the detector is complicated by the fact that the light that bleeds out at each mirror reflection has a different path length and intensity. After i reflection on the output mirror, the intensity of the beam transmitted through the output mirror is

$$I_{out,j}(t) = I\left(t - \Delta t_j\right) R^{2j} T^2 e^{\left(-(2j+1)L \cdot S \cdot n \cdot g_V(\nu(t-\Delta t_j))\right)} \tag{2.29}$$

Here S is the temperature dependent linestrength, n is the absorber concentration, g_V is the normalized Voigt line profile as a function of frequency, $\Delta t_j = (2j+1)\,L/c$, t is the time of observation, R is the mirror reflectivity, and T is the mirror transmission. Both the power and the frequency at the time of the laser light's emission have an effect on the observed power after $(2j+1)$ passes through the cell. $\nu(t)$ is the tuning curve of the laser. It should be noted that in general $1 + R \neq T$ due to the effects of mirror absorption and scatter.

The total power observed at the detector at time t is the sum of all the light bleeding out of the cavity mirror

$$I_{obs}(t) = \frac{T^2}{R} \sum_{j=0}^{\infty} R^{2j+1} I\left(t - \Delta t_j\right) e^{-(2j+1)L \cdot S \cdot n \cdot g_V\left(\nu\left(t-\Delta t_j\right)\right)} \tag{2.30}$$

The relationships between cavity characteristics, the laser ramp, absorption, and observed power are not simple, but are computationally tractable [Sayres et al., 2009]. In order to extract the absorber concentration in the cavity, the experimenter must also supply a

tuning curve for the laser ramp and the mirror reflectivity. The former can be acquired by periodically introducing an optical fringe of known FSR onto the reference detector 4.4.2, and the latter can be acquired by taking ringdown spectra 4.4.3.

The tuning curve can have a profound effect on the shape of the observed spectra and the noise characteristics of an ICOS instrument [Moyer et al., 2008]. In the case that the laser frequency scans over spectral features much more slowly than the cavity ringdown time, the shape of the spectral features is very similar to that of the direct absorption case. However, if the scan rate is comparable to or faster than the cavity ringdown time the features can become significantly skewed. The skewness arises from the fact that for faster scan rates the detector sees a wider range of wavelengths at the same time. Absorber concentrations can still be extracted from skewed spectra with appropriate software.

One benefit of scanning quickly over the target frequency range is decreased optical noise. In this context, optical noise refers to rapid changes in the number of cavity modes the laser is coupled to, or the efficiency of those couplings. Fluctuations in either can cause rapid changes in observed power. Since scanning the laser faster increases the range of wavelengths observed, it also increases the average number of cavity modes accessed at that moment.

Figure 2.10 shows part of the spectral region used in the StratoClim campaigns simulated with different tuning rates. The black curve represents an open path measurement with path length equal to the effective path length of the ICOS measurements, $L_{eff} = 6$km. The features are simulated assuming 50 ppm water vapor, 40 mb cell pressure, and cell temperature of 296 K. The features here are an HDO line at 3776.9 cm^{-1} and a cluster of $H_2^{18}O$ lines and others between 3770 and 3777.1 cm^{-1}. Increasing the tuning rates 'smears' out the spectral features, giving them a skewed shape, and also makes them broader and shallower.

Although faster scan rates can reduce optical noise, there are other effects that limit the gains to be had. The first is that spectral features that are close to each other can become

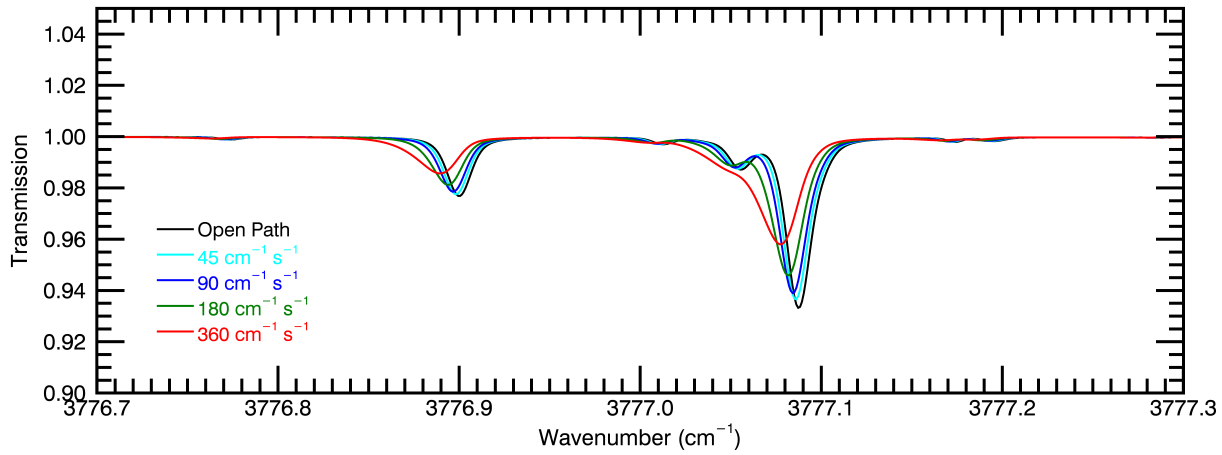

Figure 2.10: Simulated ICOS spectra at different tuning speeds. The reflectivity used in these calculations is $R = 0.99985$ and the cavity length is 90 cm. The effective path length of the cavity is 6 km, and the black curve is a simulated spectrum for an open path measurement with path length 6 km. Increasing the tuning rate makes the spectral features skewed, and they become broader and shallower as well. The features are simulated assuming 50 ppm water vapor, 40 mb cell pressure, and cell temperature of 296 K. The features here are an HDO line at 3776.9 cm^{-1} and a cluster of $H_2^{18}O$ lines and others between 3770 and 3777.1 cm^{-1}.

skewed together to the point of indistinguishability, as is the case with the cluster of $H_2^{18}O$ at the highest tuning rates. Fitting routines have a very difficult time extracting concentrations from heavily overlapping spectral features. The second problem is that it is harder to specify a baseline for broad spectral features. Fitting routines assume a baseline, and the baseline is much more constrained if the spectral feature to be fit is surrounded by ranges with little or no absorption. Increasing the ramp rate broadens the spectral features and decreases the range of low-absorption baseline to be used in the calculations. This is especially difficult for instruments that have large baseline power fluctuations or broad optical fringes.

CHAPTER 3

WATER VAPOR MEASUREMENTS AT AIDA

This chapter will discuss results of a campaign at Aerosol Interactions and Dynamics in the Atmosphere (AIDA) made with a custom-built mid-infrared TDL absorption spectrometer, operated in the AIDA facility't open-path White cell. This instrument was also called ChiWIS, but is separate from the aircraft instrument discuss in the next chapter. This instrument also measured HDO and H_2O, but only the H_2O measurements will be discussed in this chapter.

3.1 Abstract

High-altitude cirrus clouds are climatically important: their formation freeze-dries air ascending to the stratosphere to its final value, and their radiative impact is disproportionately large. However, their formation and evolution are not fully understood, as multiple *in-situ* aircraft observations have suggested that ultracold cirrus ($T < 205$ K) are frequently associated with anomalous supersaturation (water vapor up to 170% of saturation even in the presence of ice particles.) A variety of explanations for these observations have been put forth, including that ultracold cirrus are dominated by metastable ice which has a vapor pressure that exceeds that of hexagonal ice.

The 2013 Isotopic fractionation in Clouds (IsoCloud) campaign at the AIDA cloud chamber allowed explicit testing of the dynamics of cirrus formation at these low temperatures. IsoCloud data allow robust estimation of the saturation vapor pressure over ice in a series of 28 experiments with initial temperatures between 189 and 235 K with a variety of aerosols and ice nuclei. We show that over the entire temperature range, saturation vapor pressures are fully consistent with expected values for hexagonal ice and inconsistent the highest values postulated for metastable ice. The rapid nature of these experiments ($\approx$ 10 minutes) means that if formed, metastable ice would not have a chance to anneal to hexagonal ice, a process

which takes hours or longer over the whole experimental temperature range.

3.2 Introduction

Anomalous supersaturation within ice clouds has been measured by several in-situ measurement campaigns working in the upper troposphere and lower stratosphere (UT/LS). These supersaturations are most common in ice clouds at or below 205 K [Krämer et al., 2009]. Numerous explanations have been proposed for this phenomenon, including low particle numbers [Krämer et al., 2009], organic coatings on ice crystals [Cziczo et al., 2004a,b], glassy states [Zobrist et al., 2008, Kärcher and Haag, 2004], surface uptake interference due to ice binding with HNO_3 [Gao et al., 2004], metastable forms of ice [Peter et al., 2006], and instrumental error [Fahey et al., 2014]. During the recent ATTREX campaigns supersaturations of up to 70% were observed in low-concentration clouds ($< 100\ L^{-1}$), but not observed in cirrus with high concentrations up to 10000 L^{-1} [Jensen et al., 2013], suggesting that anomalous supersaturation may be attributable to slow vapor uptake is low density cirrus. Here we report vapor pressure measurement made in the presence of dense cirrus which show no evidence of anomalous supersaturation.

The coldest regions of the UT/LS play a strong role in setting the water vapor concentration of the stratosphere as a whole. The majority of stratospheric water vapor is transported across the TTL, and is dehydrated as it crosses this cold region in the atmosphere [Kremser et al., 2009]. Incomplete dehydration due to persistent supersaturation as ice crosses the TTL could result in misrepresentations of stratospheric water in chemistry models and radiative forcing calculations. Laboratory measurements have shown metastable ices with saturation vapor pressures as much as 10.5% higher than hexagonal ice at temperatures below 200 K [Shilling et al., 2006]. At 190 K, this corresponds to a difference of about 0.5 ppm H_2O. Surface radiative forcing of stratospheric water vapor has been estimated at about 0.2 W m^{-2} for a stratospherically uniform increase in water vapor of 0.7 ppm [de F. Forster and Shine, 1999]. In addition, metastable forms of ice are thought to have different radiative

properties than hexagonal ice, which may further affect Earth's radiation budget [Murray et al., 2015].

Electron diffraction [Blackman and Lisgarten, 1958, Honjo and Shimaoka, 1957], x-ray diffraction [Shallcross and Carpenter, 1957, Murray and Bertram, 2006, Malkin et al., 2012], and neutron diffraction [Steytler et al., 1983, Kuhs et al., 1987, 2012] measurements provide a way to probe the crystal structure of ice, which determines its thermodynamic stability, crystal habit, and vapor pressure. In Earth's atmosphere, ice forms layers of puckered hexagonal rings referred to as Ice I [Hobbs, 1974]. Two adjacent layers can either be mirror images (hexagonal ice, I_h) or shifted by half the ring width (cubic ice, I_c). Ice crystals can be characterized by their cubicity, χ, defined as the fraction of cubic stacking sequences in a sample. Diffraction measurements distinguish three forms of Ice I: I_h with a cubicity of zero, I_c with a cubicity of one, and I_{sd} in between (Malkin and/or Hansen).

Measurements by Murray et al. [2005], Murray and Bertram [2006], Murray [2008], and Malkin et al. [2012] have observed homogeneous nucleation of I_{sd} from micron-sized water and solution droplets suspended in oil between 170 and 240 K, and measurements by Amaya et al. [2017] observed I_{sd} in supercooled nanodrops homogeneously frozen during expansion of N_2 carrier gas. Depending on factors including freezing temperature, droplet size, and aerosol type and content, cubicity values can be as high as 75% in atmospherically relevant temperature ranges. Malkin et al. [2015a] observed cubicity values of up to $\approx 50\%$ in ice formed by heterogeneous nucleation of water containing solid inclusions. Simulations of ice crystallization by Moore and Molinero [2011] indicate that ice frozen at 180 K should have 2 cubic ice layers for every one hexagonal ice layer. Under atmospherically relevant conditions, it appears I_{sd} should form crystals with three-fold symmetry [Hallett et al., 2002, Kobayashi et al., 1987] (Furukawa), and crystals with trigonal symmetry have occasionally been observed in Earth's atmosphere Murray et al. [2015].

The transformation time from metastable ice into I_h depends strongly on the surface area of the sample [Murray et al., 2005], but for low surface area samples such as frozen

droplets the time can be quite long. Mayer and Hallbrucker [1987], Murray and Bertram [2006], and Kuhs et al. [2012] report annealing times of tens of minutes to hours over the IsoCloud temperature range, and observe that the transformation to I_h is often not complete, especially at lower temperatures. Laboratory evidence of I_{sd} formation, the absence of observations of I_h formation below 190 K [Kuhs et al., 2012], and secondary indicators like crystal habit suggest that metastable forms of ice may nucleate and persist for some time in the coldest parts of Earth's atmosphere like the TTL [Murray and Bertram, 2006], the polar stratosphere [Lowe and MacKenzie, 2008], and possibly elsewhere in the solar system [Jenniskens and Blake, 1994].

Although x-ray diffraction experiments have shown that I_{sd} can form through homogeneous nucleation and heterogeneous nucleation on droplet inclusions, none of these experiments have addressed the form of ice grown through subsequent deposition onto these crystals. Recent modeling work on ice growth by deposition [Hudait and Molinero, 2016] indicates that at moderate supersaturations ice should grow exclusively hexagonal layers in the temperature range of 200-260K, although there may be some degree of stacking disorder at temperatures below 200 K in the TTL, polar stratosphere, mesosphere, and noctilucent clouds. Modeling work by Hudait et al. [2016] suggests a free energy difference of 5.6 ± 1.2 J mol^{-1} due to stacking faults. Such a low value cannot account for the wide range of observed free energies and enthalpies in the literature for I_{sd} samples, and suggests that stacking disorder itself is probably not responsible for observations of increased vapor pressure [Lupi et al., 2017]. Rather, the presence of other imperfections like dislocations, line defects, and ice-liquid or ice-vapor interfaces make free energy contributions that can be orders of magnitude larger than that of stacking disorder. The presence of these types of imperfections seems to be strongly influenced by the method and rate of sample growth, which may explain the spread of values in the literature. Since most vapor pressure observations in cirrus clouds occur after at least some growth has occurred, regardless of nucleation method, it is important to understand how these crystals behave as new ice layers are added.

Dense cirrus quickly draw the ambient vapor pressure down to the saturation vapor pressure of ice. Our measurements use that fact to address the type of ice formed during post-nucleation growth of a crystal. The IsoCloud 4 experiments with the densest clouds have vapor relaxation times that ensure vapor will reach an equilibrium (or pseudo-equilibrium) value during the experiment. Stacking disordered ice that is rich in interfaces and defects should have a vapor pressure significantly higher than that of Ice I_h, which is assumed to be given by the Murphy-Koop (MK) parametrization [Murphy and Koop, 2005] in this work. We use a simple model and observed properties of the ice cloud and chamber gas to reconstruct the saturation vapor pressure over ice as cirrus grow and dissipate. The analysis of this data set shows that the saturation vapor pressure is consistent with the MK values over the whole experimental temperature range. This consistency indicates that ice formed through deposition in atmospheric conditions is relatively free from interfaces and defects.

3.3 Methods

The 2012-2013 IsoCloud campaigns took place at the AIDA cloud chamber at the Karlsrühe Institute of Technology (KIT). This work will discuss only the aspects of the campaign relevant to the measurements presented here, but an in depth discussion of the experiments, methods, and instruments used in the campaign can be found in Lamb et al. [2017]. During the campaign, instruments measured water vapor, total water (ice + vapor), ice particle number, pressure, and temperature. The chamber was seeded with Arizona Test Dust (ATD), Sulfuric Acid (SA), nitric acid (HNO_3), and Secondary Organic Aerosols (SOA) which allowed the study of both heterogeneous and homogeneous nucleation. The chamber's pressure and temperature can be varied to replicate conditions throughout the UT/LS, and rapid pumping on the chamber simulates updrafts and can initiate nucleation. Cirrus growth draws the chamber vapor pressure down to a constant value, which then allows the estimation of saturation vapor pressure over ice for clouds at a range of temperatures. Due to wall outgassing, high effective updraft speeds, and relatively low particle numbers in

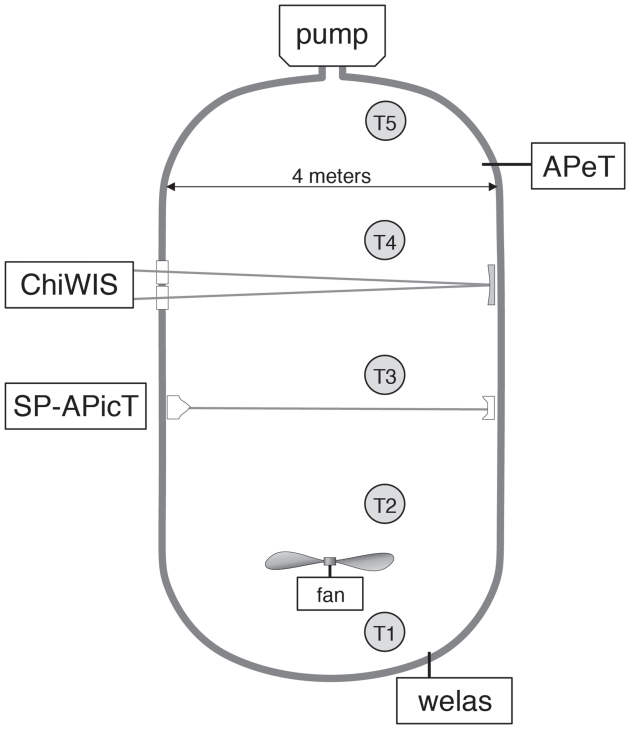

Figure 3.1: Layout of the instruments used in this analysis during the IsoCloud campaigns at the AIDA chamber. ChiWIS and SP-APicT, both open path tunable diode laser absorption spectroscopy (TDLAS) instruments, provided primary and secondary water vapor measurements, respectively. APeT, an extractive TDLAS instrument, provided total water (ice + vapor) measurements, and welas provided ice particle concentrations. Gas temperature is the average of thermocouples 1 through 4. The whole chamber is within a thermally controlled housing that sets the base temperature of an experiment. The pumps draw gas out of the chamber in a pseudo-adiabatic expansion.

certain experiments, vapor pressure does not always reach saturation, and we use a simple ice growth model to retrieve the saturation vapor pressure over ice (e_i). In the IsoCloud 4 campaign 28 pseudo-adiabatic expansion experiments at temperatures between 185 and 235 K and pressures between 300 and 170 hPa were suitable for analysis. The remainder of this section is divided into subsections discussing the characteristics of the instruments used, the experiments used and the criterion for their inclusion, and the model used to retrieve the saturation vapor pressure.

3.3.1 Instruments

Modeling ice growth to retrieve saturation vapor pressure requires measurements of water vapor, total water (vapor + ice), and ice particle number, in addition to pressure and temperature. Primary water vapor measurements come from the Chicago Water Isotope Spectrometer (ChiWIS), although in optically thick ice clouds we use a secondary water vapor measurement, the Single-Path AIDA PCI in cloud TDL (SP-APicT), to provide a backscatter correction. Total water measurements are provided by the AIDA PCI extractive TDL (APeT) instrument, and ice particle number comes from the Welas 1 instrument, an optical particle particle counter.

ChiWIS is a tunable diode laser instrument operated in open path mode using one of AIDA's White cell mirror systems. The instrument had a typical precision of 22 ppbv in H_2O through the IsoCloud 4 campaign. The the H_2O line at 3789.63 cm^{-1} has 5% uncertainty on its HITRAN line strength [Rothman et al., 2013]. Concentrations are retrieved from recorded spectra using ICOSfit, a non-linear, least-squares fitting algorithm.

During warm experiments which form very dense ice clouds, ChiWIS simultaneously experiences signal attenuation of up to 95% and backscattering of light off the cloud into the detector. These two components of the detector signal have very different path-lengths, and it is not possible to reliably retrieve only the full path-length component. In these cases we rely on the SP-APicT instrument to provide water vapor measurements because that

instrument's single-pass optical arrangement is not sensitive to backscatter. This correction was applied to all experiments at temperatures above 210 degrees, which comprise 13 of the 28 experiments considered in this analysis. (Details of the correction procedure can be found in Lamb et al. [2017].)

Total water measurements are provided by APeT, an extractive, tunable diode laser instrument [Lauer, 2007]. Based on previous comparisons of AIDA instruments [Skrotzki, 2012b], we assume APeT measurements are delayed by 17 seconds with respect to *in-situ* ones. Chamber ice content is the difference between the total water and vapor phase measurements. Below 200 K the signal-to-noise ratio of SP-APicT is very low due to its short path length, so for better precision we use ChiWIS to calculate ice mass at all temperatures. However, ChiWIS and APeT use different spectral lines and measurement methods, so care must be taken to ensure that ice mass is calculated correctly. At temperatures above 200 K, APeT and SP-APicT (which use the same spectral line to retrieve H_2O concentrations) report mixing ratios about 2.5% lower than ChiWIS during ice-free periods. This difference is likely due to HITRAN linestrength errors, and to correct them the APeT total water measurement is scaled up by 2.5%. After applying this universal scaling factor, if there is still an offset between the two instruments prior to the expansion (when there should be no ice cloud in the chamber), that offset is subtracted from the whole experiment. These offsets are most significant below 200 K, which may be due to water outgassing within the instrument, or in the case of APeT, ice forming in its inlet. See supplemental materials for details of instrument comparisons.

Ice particle concentrations come from the Welas 1 instrument, which counts ice particles between 0.7 and 46 μ m [Wagner and Mhler, 2013] in diameter. In addition to counting errors, the conversion of this instrument's count rate into a number concentration has a 10% uncertainty. Ice particle number concentration is used to estimate the average radius of particles in the chamber and the average, per-particle growth rate.

Temperature measurements are the average of four thermocouples suspended at different

heights in the chamber. These measurements have an accuracy of 0.3 K during pumpdowns and 0.15 K between pumpdowns. A mixing fan at the bottom of the chamber is always operational and ensures the uniformity of the chamber. Figure 3.2 shows the positions of the instruments used during IsoCloud in the AIDA chamber, as well as the locations of the thermocouples.

3.3.2 Experiments

In a typical IsoCloud experiment ice clouds are formed by pumping on nearly-saturated chamber air, which causes rapid cooling and ice nucleation. Air was kept close to saturation before pumping by preparing the chamber walls to be ice-covered. Pseudo-adiabatic expansion experiments were performed at base temperatures between 189 and 235 K in IsoCloud 4. During the first part of each experiment the temperature falls off nearly adiabatically, but eventually heat flux from the walls balances the cooling. The total amount of cooling varies from 5-9 K and is controlled by the pump speed. Effective updraft speeds are typically several meters per second, which are much faster than those typically associated with cold cirrus. Before each experiment the chamber can be seeded with different aerosols or ice nuclei. Most experiments in IsoCloud 4 used ATD, but in several experiments the chamber was seeded with aerosols to explore homogeneous nucleation.

Wall ice keeps the chamber at 80-90% of saturation before the expansions, which implies that the wall ice is 0.5-2 K colder than the chamber air. After nucleation occurs, the ice cloud draws the chamber vapor pressure below the saturation vapor pressure over the wall ice, and it becomes a source of vapor for the growing cirrus cloud. Despite loss to the pumps, chamber total water is often observed to be larger at the end of pumping than at the beginning due to mass transfer from wall ice to cirrus cloud. Once the pumps cease the cirrus cloud dissipates and its mass is transferred back to the walls.

Of the 48 IsoCloud 4 experiments, 6 were reference expansions, and four others lacked measurements of one of the physical quantities required for analysis. Of the remaining 38

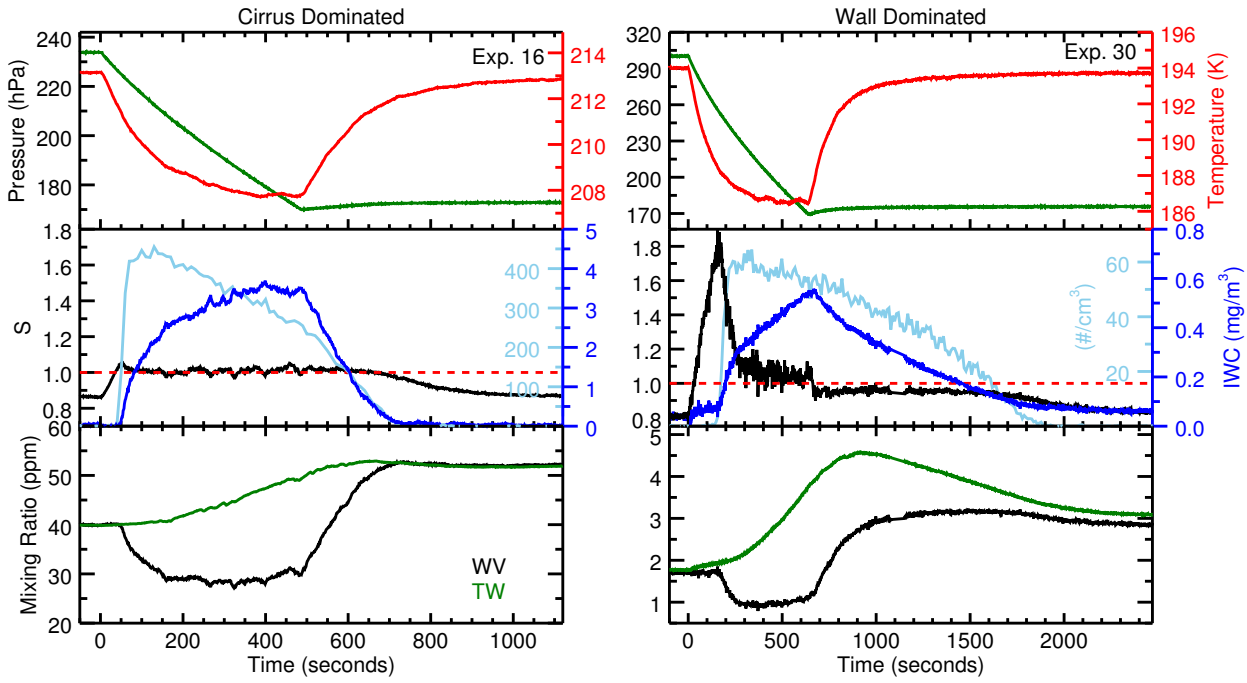

Figure 3.2: Examples of experiments in which vapor is controlled by cirrus uptake (*left*) and wall flux (*right*). Experiment 16 is a heterogeneous nucleation experiment onto ATD, and experiment 30 is a homogeneous nucleation experiment with SA aerosol. The top panels of each plot show the pressure (green) and temperature (red) evolution of each experiment. The action of the chamber pumps results in a pseudo-adiabatic expansion which cools the chamber gas rapidly at first, then more slowly as the cooling is balanced by heat flux from the chamber walls. The chamber gas rapidly warms once the pumps have stopped. The middle panels show MK saturation (red, dashed line), measured saturation (black), ice particle number (light blue), and the cloud's ice water content (dark blue). Ice nucleation starts at the peak in saturation, and is followed by a sharp increase in particle number and rapid cloud growth. Saturation relaxes back to a constant value, where it stays until the pumps turn off. In the cirrus dominated experiment, that value is the saturation vapor pressure over ice. In the wall flux dominated experiment the saturation tends to a value determined by the wall flux, about 8% in the experiment shown. When the pumps stop the the vapor pressure returns to the wall controlled value in the cirrus controlled experiment, but in the wall flux controlled experiment the decay rate is limited by wall uptake. The bottom panels show total water (green) and water vapor (black). The small data gap in experiment 30 at around 1100 seconds is due to realignment of the White Cell mirrors.

experiments, this analysis uses 28 and excludes ten. The criteria for including an experiment in the analysis are relatively short relaxation times back to saturation and preparation of the chamber walls with ice. For each experiment a relaxation time is calculated following Korolev and Mazin [2003], which takes into account effective updraft speeds, ice particle number, and particle size to estimate a relaxation time to a pseudo-equilibrium value. Due to the relatively short length of the expansion experiments we exclude any experiments with typical relaxation times greater than 250 seconds during the growth phase of the expansion. Table 3.1 outlines the characteristics of experiments that are included in the analysis.

Dry wall preparation poses a problem for our analysis because there is relatively little information about growth in these experiments. In experiments prepared with ice-covered walls, the ice cloud takes up water vapor at the expense of the walls until the pumps turn off. In dry wall experiments, this source of water vapor is not present, and almost all ice growth happens immediately after nucleation until the supersaturation is drawn down. After that, the ice cloud's mass decays nearly in proportion to the pump's action on the chamber until it turns off, after which it decays rapidly as the chamber warms. Table S1 in the supplementary material shows the excluded experiments and the reasons for their exclusion.

Experiments used in this analysis fall into two broad categories: 1) those in which water vapor loss to cirrus ice uptake dominates any contribution of the wall flux, and 2) those in which ice uptake is nearly balanced by wall flux. Figure 3.2 shows the evolution of relevant variables in each type of experiment. In cirrus dominated experiments, water vapor concentrations draw down quickly to saturation (left); in wall dominated ones, water vapor concentrations remain above saturation during the growth phase (right).

In experiments dominated by ice cloud uptake there is a brief period of supersaturation before nucleation occurs, followed by rapid ice growth and a corresponding drawdown of vapor pressure to a value close to the MK value. In the heterogeneous nucleation experiment shown in Figure 3.2 the ice particle number reaches about 400 cm^{-3}, then decreases nearly in proportion to the action of the pump. Although the supersaturation appears to be almost

zero in this experiment, the ice cloud continues to grow until the expansion ceases. The water necessary for this growth is provided by the ice-covered chamber walls. After the expansion stops, the ice cloud decays over a roughly 200 second period, after which the vapor pressure returns to the wall-controlled value.

In the wall flux dominated experiment, the chamber was prepared with sulfuric acid, so the supersaturation peaks at about 85% before homogeneous nucleation occurs. Ice cloud growth draws the supersaturation down to a constant value of about 8%, which is the value required to drive a growth rate high enough to balance the wall flux. This supersaturation persists until the expansion stops, when it rapidly jumps to $RH_{ice} \approx 95\%$. The evaporation of the cloud is balanced by wall uptake and the saturation stays roughly constant until the cloud is nearly dissipated, at which point it returns to the wall-controlled value.

3.3.3 Analysis

All experiments that meet the criteria outlined above reach a nearly constant supersaturation, but as experiment 30 in Figure 3.2 makes clear, this value can vary significantly and sometimes reflects processes other than simple draw down to the saturation vapor pressure. Figure 3.3 shows the average observed saturation during the last 200 seconds of pumping, when the cirrus mass is at its greatest and the saturation has relaxed back to a nearly constant value. Above about 195 K, the saturation are clustered between about 1.00 and 1.03, but below this range, there is large variation. Clearly, assuming that the vapor pressure relaxes back to the saturation vapor pressure set by the ice cloud is overly simplistic. To retrieve this quantity we model the vapor pressure evolution, and take as inputs the ice mass, particle number, growth rate, pressure, and temperature, all of which are directly measured or derived from measured quantities. The model uses these quantities to predict the chamber vapor pressure, and we fit that prediction to the observed H_2O vapor pressure, letting the saturation vapor pressure be the free parameter. In this subsection we discuss details of the model, the criteria that define the fit region for each experiment, sources of uncertainty, and

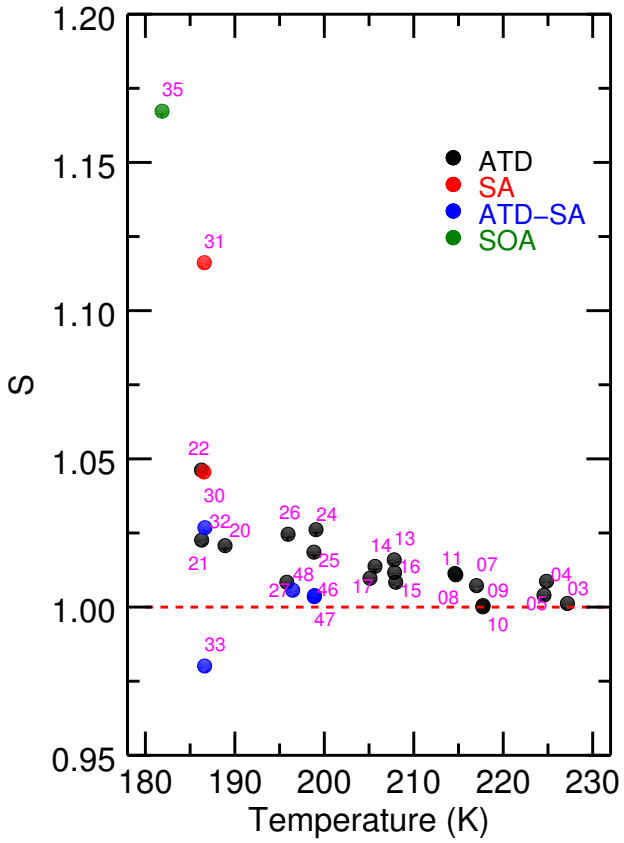

Figure 3.3: Average measured saturation of included experiments after relaxation back to a constant value. Cirrus dominated experiments ($T \geq 195$ K) typically show saturation values from 1.00 to 1.02. Wall dominated experiments (below ≈ 195 K) show supersaturations up to about 17%, which are necessary for the cirrus growth rate to match the mass flux off the chamber walls. A simple ice growth model is necessary to extract the saturation vapor pressure required to account for the observed vapor pressure and growth rate.

the generation of error bars.

To retrieve the saturation vapor pressure from the experiments, we rearrange the diffusional growth rate equation over ice [Pruppacher and Klett, 1997] to calculate the far-field water vapor pressure, and treat the saturation vapor pressure over ice as a free parameter in a fit to the measured vapor pressure:

$$e = xe_i\big(1 + \frac{\dot{m}L_i}{4\pi r k_a^* T_\infty}(\frac{L_i M_w}{RT_\infty} - 1)\big) + \frac{\dot{m}RT_\infty}{4\pi r \alpha D_v^* M_w} \tag{3.1}$$

In this formulation e_i is taken to be the MK saturation vapor pressure and x is a constant scale factor for each experiment. Here $\dot{m}$ is the per particle growth rate, M_w is the molar mass of water, L_i is the latent heat of sublimation, D_v^* is the diffusivity of water in air with kinetic corrections, T_∞ is the gas temperature in the chamber, and k_a^* is the thermal accommodation coefficient, which is taken here to be unity. We also identify the measured vapor pressure e with the far-field vapor pressure.

We assume the particles are spherical, which is a reasonable approximation for small, micron-sized particles. We also assume that the accommodation coefficient α is 1, consistent with Skrotzki et al. [2013]. In the range of 0.2 to 1, the calculation is quite insensitive to changes in α, but assuming values below 0.2 results in very low estimates of the saturation vapor pressure (see supplementary material).

The Welas particle counter has a lower size cutoff of 0.7 μ m, which may result in undercounting when the average particle size is low, and especially when the cloud is first growing or finally dissipating. Some of the coldest experiments have very small ice crystals, and show an abrupt increase in the calculated mass-average ice radius as the cloud dissipates, which is likely due to undercounting as the cloud evaporates and a significant number of particles are missed by the particle counter. Regions with such unphysical behavior are removed from the fit by excluding times when the calculated radius is less than 0.85 μ m.

Although we explicitly exclude from analysis time intervals where the ice particle num-

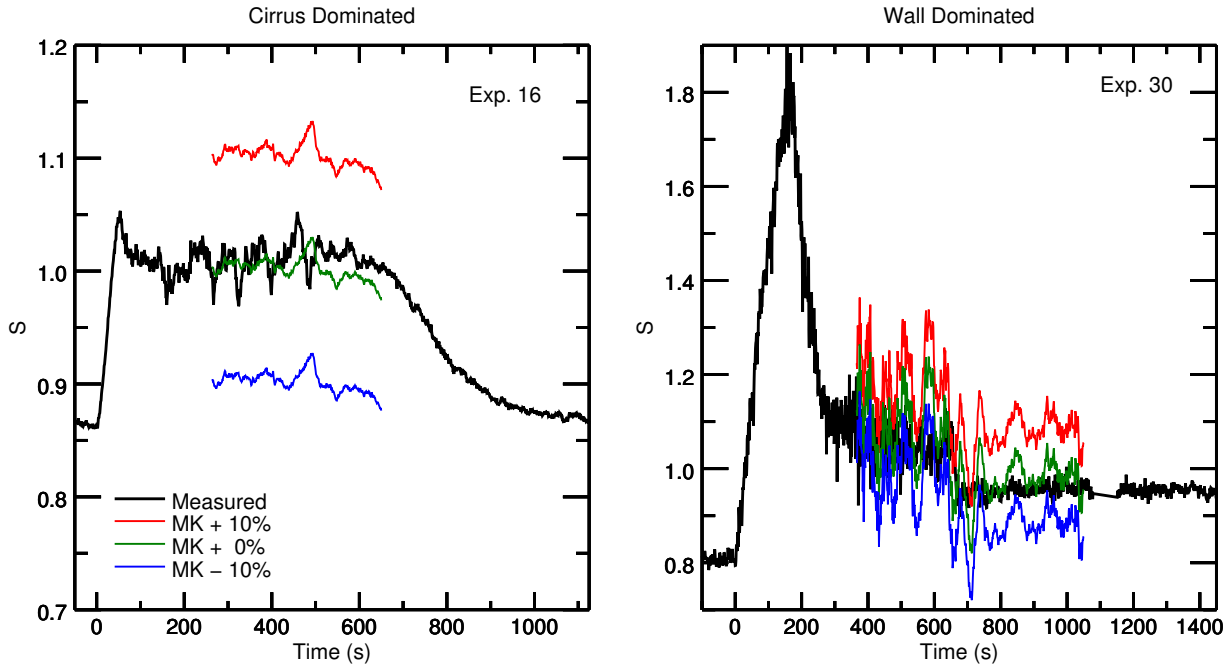

Figure 3.4: Model output for experiments 16 and 30. Each output is calculated using observed quantities under different assumptions about the 'true' saturation vapor pressure of cirrus. The red line assumes the true value is 10% higher than the MK saturation vapor pressure, the blue line assumes it is 10% below, and the green line assumes MK is the true saturation vapor pressure. Calculated saturations are smoothed by 30 points ($\approx$ 30 seconds). Measured saturations are unsmoothed. Cirrus dominated experiments are very sensitive to the assumed vapor pressure, which is reflected in their relatively small uncertainties due to instrumental error. Wall controlled experiments are less sensitive and show correspondingly larger error bars in the final analysis.

ber is known to be low, it is possible, especially at lower temperatures where the particle sizes are typically small, for systematic undercounting to occur throughout an experiment. Rough estimates of the log-normal size distribution for the coldest temperatures indicate that undercounting in the fit window can be up to 50%. If undercounting occurs, then the per-particle growth rate is an overestimate. This depresses the estimate of the saturation vapor pressure and results in a low bias. To test the sensitivity of our results to particle number, we artificially increased the particle number given to the fit routine by factors of 1.5, 2, and 5 then re-ran the analysis. For temperatures above 210 K, there is almost no change in the results. Below 210 K, the largest changes are found in the three homogeneous nucleation experiments, which are the experiments that fall farthest below the MK saturation line to begin with. The largest increase in retrieved vapor pressure is about 2.5%. Heterogeneous nucleation experiments in this temperature range show changes of less than 0.5%. This effect is small and does not change the conclusions of this analysis. See supplementary material for more details.

In each time interval, the ice cloud can change mass by sublimation/deposition to/from the vapor, or by the action of the pumps removing particles. In calculating the per-particle growth rate, we correct for pumping loss by subtracting the second of the effects from the derivative of the cirrus ice mass. The pumps remove a constant volume of gas from the chamber in each time interval, and we assume that they act in the same manner upon the small ice particles found in our experiment.

Figure 3.4 shows the model's sensitivity to changes in the assumed saturation vapor pressure. The observed saturation is plotted in black, and the model output for three different assumptions about the saturation vapor pressure is plotted in color. Model outputs are plotted over the same time intervals used in the analysis. The model is quite sensitive to different assumed saturation vapor pressures. As the functional form would suggest, 10% changes in xe_i result in $\approx 10\%$ changes in e. The wall dominated experiment shows a sizable periodic feature with distinct periods during the pump-on and pump-off intervals. These

oscillations correspond to periodic variation of temperatures in the chamber, and are not captured by the model.

In experiments with high ice particle number where ice cloud growth dominates, the calculations done above are not significantly different from simply assuming that value to which the saturation relaxes is the vapor pressure over ice. (See supplementary material.) The analysis above is only strictly necessary in situations where the chamber is not dominated by by ice cloud growth, but for consistency all results presented are from the calculations.

3.3.4 Uncertainty Analysis

Error bars are calculated for each experiment and reflect both instrumental uncertainty in measurements and systematic offsets, such as linestrength errors. Horizontal error bars represent a simple standard deviation of the temperatures corresponding to the fit region. Fits at higher temperatures typically have much smaller horizontal error bars since typical fit regions at in that regime are almost completely within the time interval when the wall heat flux balances adiabatic cooling. At lower temperatures the ice cloud often persists for some time after the pumps turn off and the chamber begins to warm back to its base temperature. Fit regions in these experiments generally include some of this temperature swing resulting in the larger horizontal error bars at lower temperatures.

The error corresponding to instrumental uncertainty is calculated using a Monte-Carlo method. Each physical parameter used in the calculation has a known measurement uncertainty which we use to generate new data for each parameter. For each experiment, we generate 2000 such parameter sets, and run the fit routine on each set, yielding a distribution of saturation values. These distributions are nearly normal (see supplementary material), and the standard deviation of each experiment's distribution gives the component of the error bar associated with measurement uncertainty.

The other major source of uncertainty is due to HITRAN linestrength errors, which arises in two ways. The first is raw uncertainty on the linestrength at the reference temperature of

296 K, and the second is the uncertainty in the gas temperature measurements manifesting in the calculated linestrength at the experimental temperature. The H_2O line Chi-WIS uses has a raw uncertainty of 5%, temperature fluctuations of 0.3 K result in linestrength fluctuations of less than 0.1% and are not included in this analysis. Raw linestrength errors are added directly to the calculated error bars and in most experiments they are the dominant source of uncertainty.

3.4 Results

The data show no evidence of anomalous supersaturation, and instead suggest that cirrus formation is consistent with expected microphysics. Figure 3.5 shows the results of our analysis on the 28 experiments which met the criteria outlined above; all experiments are consistent with MK saturation and inconsistent with the saturation given by Shilling for metastable ice. These experiments should provide constraints on ice growth in the real atmosphere, because our experiment featured faster cooling rates than would be seen in atmospheric cirrus, and would therefore be more susceptible to effects on ice growth or to metastable forms of ice. We conclude that prior reported observations of anomalous supersaturation reflect either measurement error measurements in clouds with extremely long relaxation times back to saturation.

These conclusions are unchanged within the estimated uncertainties. For most experiments the $\pm$ 5% linestrength error is much larger than the model uncertainty due to random measurement errors. All experiments except 20-22, 30-33, and 35 have model uncertainties of less than 0.5%. Model uncertainties for experiments 20-22 and 30-33 have errors between 0.5 and 2%, and for experiment 35 the value is 9.4%. In Figure 3.5 the error bars shown are the sum of the one-sigma model uncertainties and the linestrength errors.

The retrieved vapor pressure does appear to show some dependence on the type of aerosol/IN used. ATD experiments appear to be 101-102% of the MK saturation vapor pressure at all temperatures, while experiments performed with SA-ATD under the same

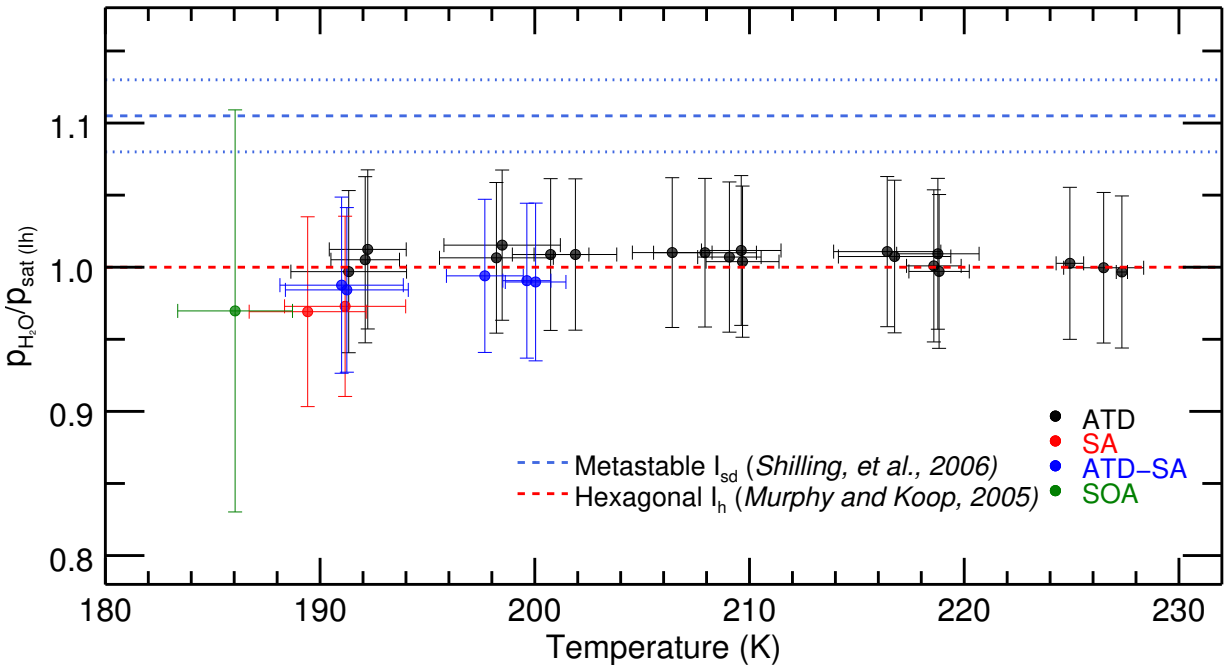

Figure 3.5: Retrieved saturation vapor pressures for each experiment as a fraction of MK saturation plotted vs average experiment temperature. Experiments are colored by aerosol/IN type. Heterogeneous nucleation occurs for ATD (black) and SA-ATD (blue) experiments. SA (red) and SOA (green) experiments undergo homogeneous nucleation. Horizontal error bars are the standard deviation of the temperatures found in the fit region. Vertical error bars reflect errors from measurement uncertainty and linestrength errors. The red, dashed line represents MK saturation. The blue, dashed line represents Shilling's value for the vapor pressure of cubic ice, and the blue, dotted lines show the errors of that measurement. Experiments are colored by aerosol/IN type.

conditions appear cluster from 98-100%. Given that line strength errors should affect all these measurements in the same way, this clustering appears to be significant. In Figure 3.6 just the experiments below 205 K are shown. To emphasize the difference between ATD experiments and experiments containing SA, the component of the error bars due to linestrength errors has been removed. (This error would affect all experiments in the same direction, leaving their relative positions the same.) Experiments containing sulfuric acid are on average 2.6% lower than ATD experiments in this temperature range. Due to the lower heterogeneous nucleation threshold of ATD, it is likely that in ATD-SA experiments most nucleation was heterogeneous onto dust particles. Sulfuric acid experiments also yield saturation vapor pressures several percent below the MK value, so it may be that that the presence of SA is responsible for this effect. One possible mechanism may be water uptake by hygroscopic SA aerosols keeping the observed vapor pressure lower than the model would predict using MK saturation. These aerosols would presumably contribute to the total water measurements, but would be missed by the particle counter, which may explain why artificially increasing the particle number has a much larger effect on SA experiments than any others.

3.5 Conclusions

Our results show that saturation vapor pressures in ice clouds with high ice particle concentration are consistent with the MK parametrization at temperatures above 185 K, and inconsistent with the parametrization given by Shilling. These results are consistent with growth from the vapor in these temperature ranges occurring through the addition of either: a) stacking-disordered layers relatively free of defects or interfaces, or b) hexagonal layers. In either case, since the vapor pressures are consistent with MK, the result points towards anomalous supersaturation in the coldest parts of the UT/LS being the result of some other process besides the growth of I_{sd}. The results in Jensen et al. [2013] suggest that persistent supersaturation is likely a consequence of the long relaxation times to saturation found in

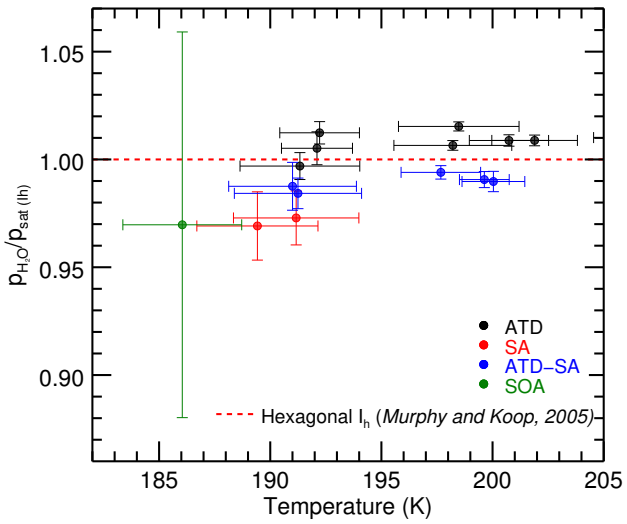

Figure 3.6: Zoomed in view of the experiments below 205 K. Linestrength errors result in the same shift for all experiments, so they are not included in the error bars here. Experiments containing sulfuric acid are $\approx 2.6\%$ lower on average than those containing pure ATD experiments. Experiments are colored by aerosol/IN type and MK saturation line is included for reference.

very thin cirrus. This is consistent with the work presented here, which focused on thick clouds with fast relaxation times. These results are also consistent with the modeling work of Hudait [Hudait and Molinero, 2016], which indicated that ice grown from the vapor should be hexagonal above about 200 K. That work leaves open the possibility of some degree of stacking disorder is present in ice formed below 200 K.

Although it seems likely that I_{sd} plays little role in anomalous supersaturation, its radiative properties may still exert some influence on Earth's climate. Preliminary findings by Murray et al. [2015] show that trigonal crystals have a lower absorption efficiency than hexagonal ones, and that for a broad range of sizes the single-scattering albedo is significantly higher for trigonal columns.

Diffraction measurements remain the best way to probe the presence of I_{sd} in ice. Future work should focus on high time resolution observations of ice nucleating and growing paired with observations of atmospherically relevant observables like water vapor pressure and crystal habit. Such measurements are needed to explore precisely how homogeneous and heterogeneous nucleation occur in the real atmosphere and how I_{sd} grows under deposition

in the ultracold regions of the UT/LS.

Future work should include a broader variety of aerosols and test them over a wider temperature range. Of particular interest would be the inclusion of aerosols known to promote the formation of I_{sd} at warmer temperatures such as $(NH_4)_3H(SO_4)_2$. These could shed light on the importance of I_{sd} nucleation to subsequent crystal habit over a broader temperature range that is more easily accessible in the cloud chambers like the AIDA facility. Aerosols that are especially favorable to I_{sd} nucleation might also promote the formation of more defects and interfaces by multiple nucleations occurring in a short time frame. Similarly, highly viscous aerosols that take a long time to freeze could have the same effect.

The underlying crystal structure of substances that serve as heterogeneous ice nuclei can promote or suppress nucleation [Houghton, 1985]. Substances with a significant mismatch between their crystal lattice dimensions and those of I_h undergo the onset of heterogeneous nucleation at lower temperatures than those with a good match. Similarly, it is possible that certain chemicals or mineral dusts could be more favorable to the nucleation of cubic ice layers than others, most likely those with cubic habit and lattice dimensions similar to cubic ice's 6.385 Å.

3.6 Supplementary Material

This section contains additional discussion of aspects of the model and experiments.

3.6.1 Instrument Comparison

In the IsoCloud campaign, three water instruments provided data used in this analysis. ChiWIS and SP-APicT both provided water vapor measurements, and APeT provided measurements of total water (vapor + ice). SP-APicT and APeT both spectrometers and use the same spectral line to make their measurement, but SP-APicT is a single pass in-situ instrument and APeT is an extractive instrument that uses an Herriot cell for increased path

length. ChiWIS is a multi-pass in-situ instrument that uses a different spectral line to make its water vapor measurement. Before these instruments can be used in the data analysis, some differences between them must be reconciled.

Low Temperature Performance

Water measurements are notoriously difficult to make at low temperatures due to the 'stickiness' of the water molecule and the large of H_2O concentrations in the atmosphere. In IsoCloud 4 the ice-wall experiments provide a way to gauge the low temperature performance of the instruments. In such experiments water is added to the chamber until a large enough coating of ice is formed on the wall to hold the saturation at 80-90% of the MK value calculated from the chamber gas temperature. Figure 3.7 shows the fractional deviation of ChiWIS (black) and SP-APicT (blue) against the saturation vapor pressure of the chamber gas. At temperatures above 200 K SP-APicT and ChiWIS show a nearly constant deviation, but at temperatures below 200 K, SP-APicT becomes almost 10% higher. This pattern indicates contamination at low water or perhaps the presence of data retrieval errors for a small spectral line.

The behavior of the APeT instrument is very similar to that of SP-APicT at temperatures above 200 K, but it shows larger deviations at low temperatures. At the lowest temperatures, ice lingers in the chamber for a very long time, and there is even residual ice present at the start of the subsequent experiment. (The experiments for which this is the case also lack Welas 1 data and they are not included in the analysis.) However, even in experiments for which this is not the case, APeT shows a larger increase than SP-APicT at low temperatures, which may be due to ice forming on the instrument's inlet.

Linestrength Errors

Spectrometers are subject to linestrength errors which typically manifest as multiplicative offsets between instruments. To quantify the magnitude of this error between the instruments

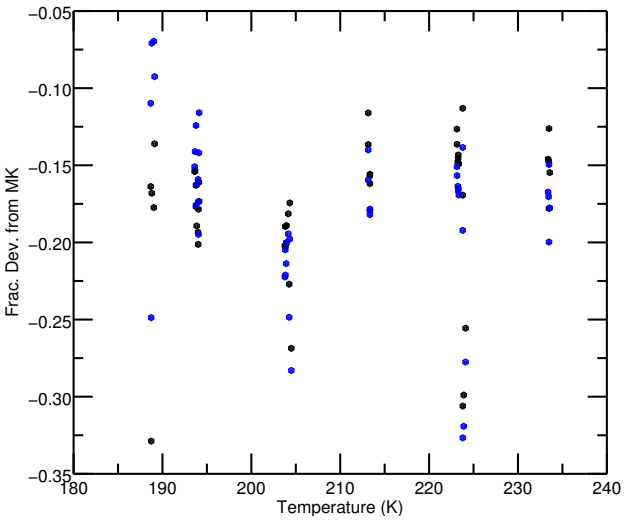

Figure 3.7: Fractional deviation of ChiWIS and SP-APicT against MK saturation. The deviations and temperatures are the average values of the 60 second period before the pump turns on. The 45 experiments for which there is suitable data to calculate this average are plotted here.

used here, we look at at their pre-experiment values when there is no ice in the chamber. Figure 3.8 shows the percent deviation between ChiWIS and SP-APicT during the 60 seconds before pumping begins for all experiments in the IsoCloud 4 campaign. For temperatures above about 200 K, this deviation is quite linear, and on average SP-APicT is 2.5% below ChiWIS. Below 200 K, the deviation increases strongly, probably due to contamination within the SP-APicT instrument. We take this value of 2.5% to be the linestrength error between the ChiWIS and SP-APicT spectral lines.

Absolute Errors

Due to its relative lack of contamination and higher precision at low temperatures, ChiWIS is used to calculate chamber ice content and growth rate. To make this calculation, APeT is first scaled up by 2.5% to account for linestringth errors. However, there is typically still a small, apparently random difference between the instruments at temperatures above 200 K, and a larger difference at lower temperatures due to APeT reporting higher values at low temperatures. These remaining differences are taken to be constant, absolute offsets, and

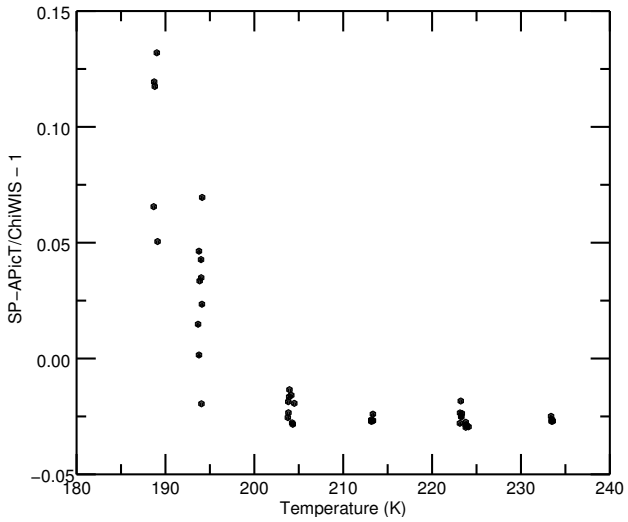

Figure 3.8: Fractional deviation between SP-APicT and ChiWIS plotted vs temperature. The average deviations and temperatures are calculated in the 60 seconds before the pump turns on.

are subtracted from the whole experiment.

3.6.2 Experiments

IsoCloud experiments are strongly influenced not only by the properties of the ice cloud (number concentration, temperature, etc.), but also by the preparation and behavior of the wall. This section lays out the different ways in which wall flux can affect an experiment and quantifies these effects.

Types of Experiments

Figure 3.9 shows the change in S that occurs after turning the pumps off. The change is calculated as the average S of the 200 seconds before the pump turns off minus the average S of the 200 seconds after it turns off. This difference reveals several different categories of experiment. Those with negative ΔS are typically ones that show a 'bump' in S after the pumps turn off and the chamber rapidly warms. This bump may indicate that the ice cloud is not decaying uniformly across the chamber. Since heat flux enters the chamber through the

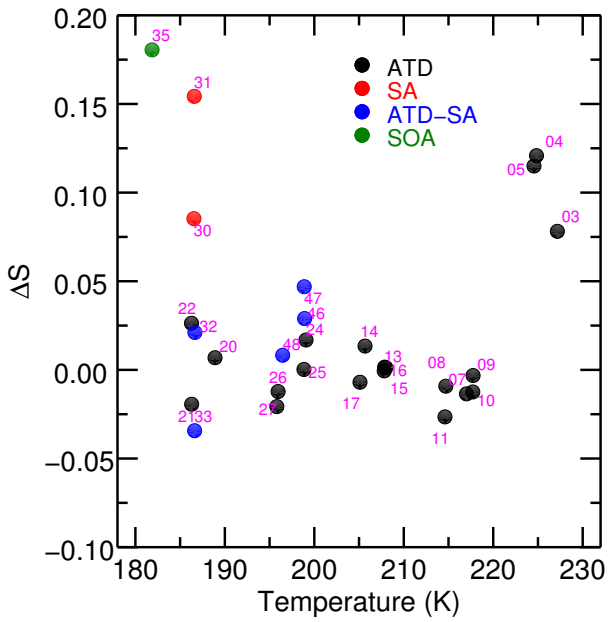

Figure 3.9: Difference between pre- and post-pump-turnoff values plotted against pre-turnoff average temperature. The difference is calculated by averaging the saturation values for 200 seconds before the pump turns off and 200 seconds after the pump turns off, then subtracting the post-turnoff value from the pre-turnoff value. Experiments are labeled by number and colored by aerosol/IN type.

walls, it follows that cirrus near the walls would be the first to sublimate, although the mixing fan will mitigate this behavior. However, the net effect of this inhomogeneous sublimation across the chamber will be to report a concentration (which is, roughly speaking, an average across the laser's path) which is higher than the expected saturation value calculated from the chamber's thermocouples, which are close to the centerline of the chamber. Experiments 8, 11, 17, and 21 are good examples of this type of experiment, which occurs at all temperature ranges. However, the magnitude of the effect is quite small and it only occurs when the cloud is rapidly warming and sublimating, so its overall effect on retrieved saturation vapor pressures is small.

Some experiments like the $\approx$ 230 K day and 46-48 show a large positive ΔS because the cloud has already partially decayed in the latter time interval. These are experiments in which the wall's influence on the ice cloud is relatively unimportant, which may be due to relatively low wall flux (cf. Figure 3.10), which implies that relatively little ice mass is

added to the cloud beyond that which is available in the vapor.

The large positive ΔS in the colder experiments is the wall-dominated pattern that is most apparent in experiments 30, 31, and 35. In these experiments the flux from the wall is quite large compared to the uptake capacity of the ice cloud, and a significant supersaturation is necessary to drive enough growth to balance the wall flux. In all ice-wall experiments included in the analysis the ice flux roughly balances the ice growth by the end of pumping, as evidenced by the measured saturation settling to a nearly constant value.

Wall Flux

In experiments with ice covered walls, the wall flux drives cirrus growth as long as the vapor pressure of the chamber gas is less than the saturation vapor pressure set by the wall ice. This is typically the case whenever there is a reasonably thick, established ice cloud in the chamber and its temperature is lower than that of the walls.

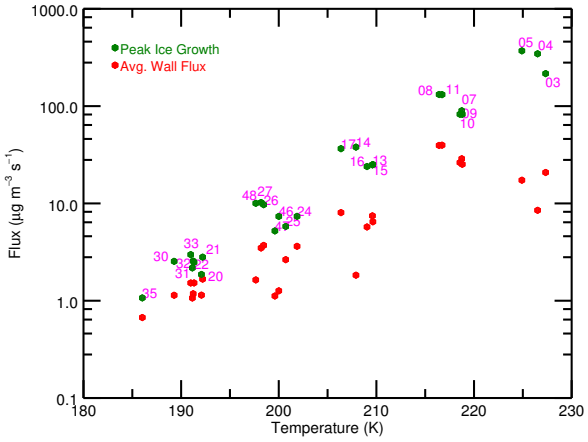

Figure 3.10: Maximum depositional flux onto cirrus (green) and typical wall flux (red) for the 28 experiments included in the analysis. The maximum depositional flux occurs shortly after ice nucleation. The typical wall flux is the average of the wall flux during the 200 seconds prior to the pump turning off. The temperature of each point is the average temperature during the fit window. Experiments are labeled by their experiment number.

Figure 3.10 shows the maximum cirrus depositional flux and typical wall flux for each

experiment included in the analysis. The maximum depositional flux occurs shortly after the cloud nucleates and is taken to be a measure of the uptake capacity of the chamber cirrus in a given experiment. Peak deposition scales very nearly with the saturation vapor pressure over ice. The typical wall flux value is calculated as the average wall flux during the last 200 seconds of pumping. By this time in most experiments, the gas temperature has settled to a nearly constant value, which means that the difference in saturation vapor pressure over cirrus ice and saturation vapor pressure over wall ice in nearly constant as well, since the wall temperature is almost constant through experiments. This constant difference in vapor pressures is the cause of the nearly constant wall flux in this time interval.

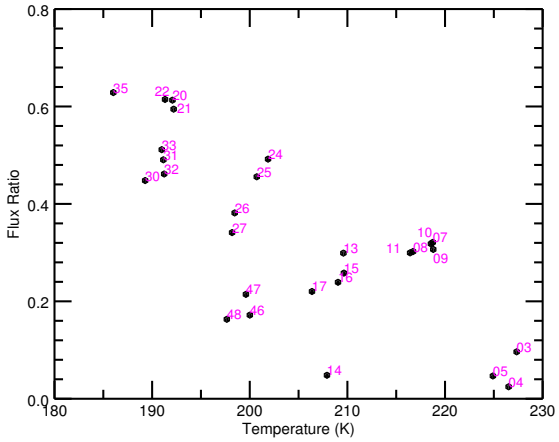

Figure 3.11: Ratio of typical wall flux to peak depositional flux onto cirrus plotted as a function of temperature. The temperature is the average temperature for each experiment's fit region, and each experiment is labeled by its experiment number. Wall flux tends to become less important as temperature increases.

Figure 3.11 shows the ratio of the average wall flux to the peak deposition for the 28 experiments included in the analysis. The wall flux becomes more important at lower temperatures because the typical wall flux does not drop off at low temperatures as quickly as cloud uptake does. There are no evident systematics in our results due to wall flux.

3.6.3 Model Details

Sensitivity to assumption of accommodation coefficient

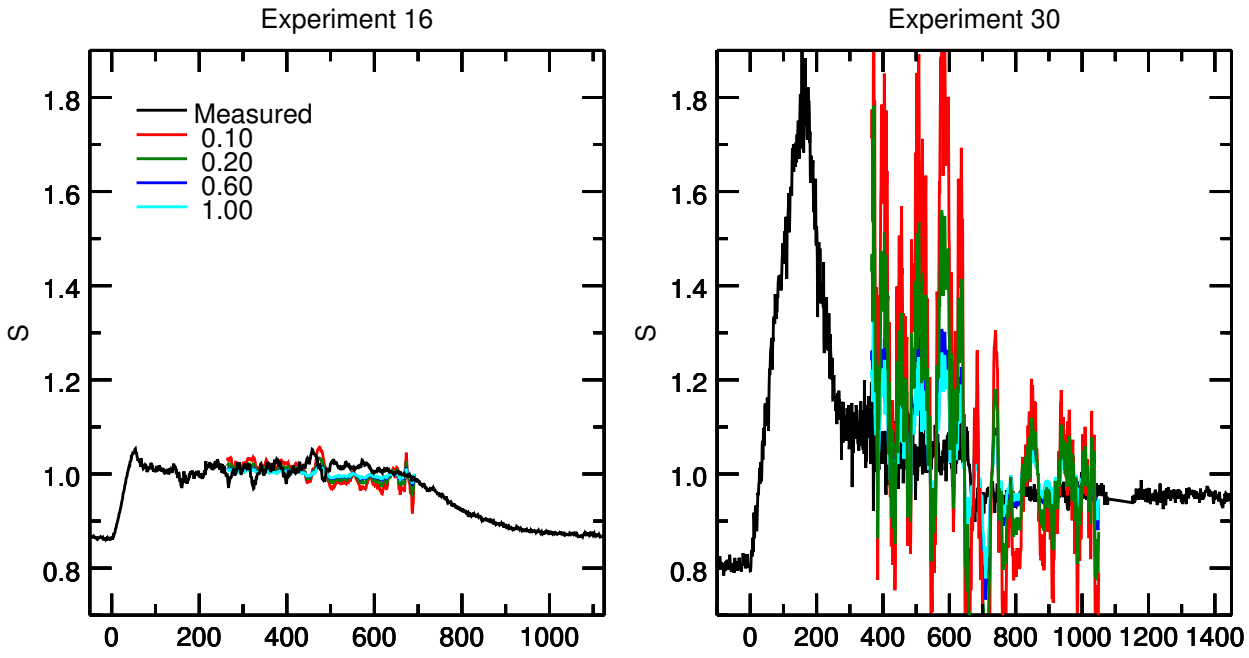

Figure 3.12: Model output for experiments 16 and 30 under different assumptions of accommodation coefficient. Measured data (black) is plotted on one-second intervals, and model output is smoothed by 30 points. Time is shown as seconds since the onset of pumping.

The model is quite insensitive to assumptions about accommodation coefficient. The model outputs for experiments 16 and 30 are shown in Figure 3.12. The overall effect of decreasing the accommodation coefficient is to make the model more sensitive to temperature fluctuations in the data and to shift the model fits to slightly lower saturation vapor pressure. Assuming an accommodation coefficient of 0.2 instead of 1 results in an average decrease of 0.5% in the retrieved saturation vapor pressure. Wall dominated experiments such as 30 and 35 experience significantly larger decreases of about 2.5%. Physically, this decrease in retrieved saturation vapor pressure makes sense because if water vapor molecules attach to ice less efficiently, then a higher supersaturation is required to drive the observed growth. The only means by which the model can create a larger supersaturation is to decrease the assumed saturation vapor pressure.

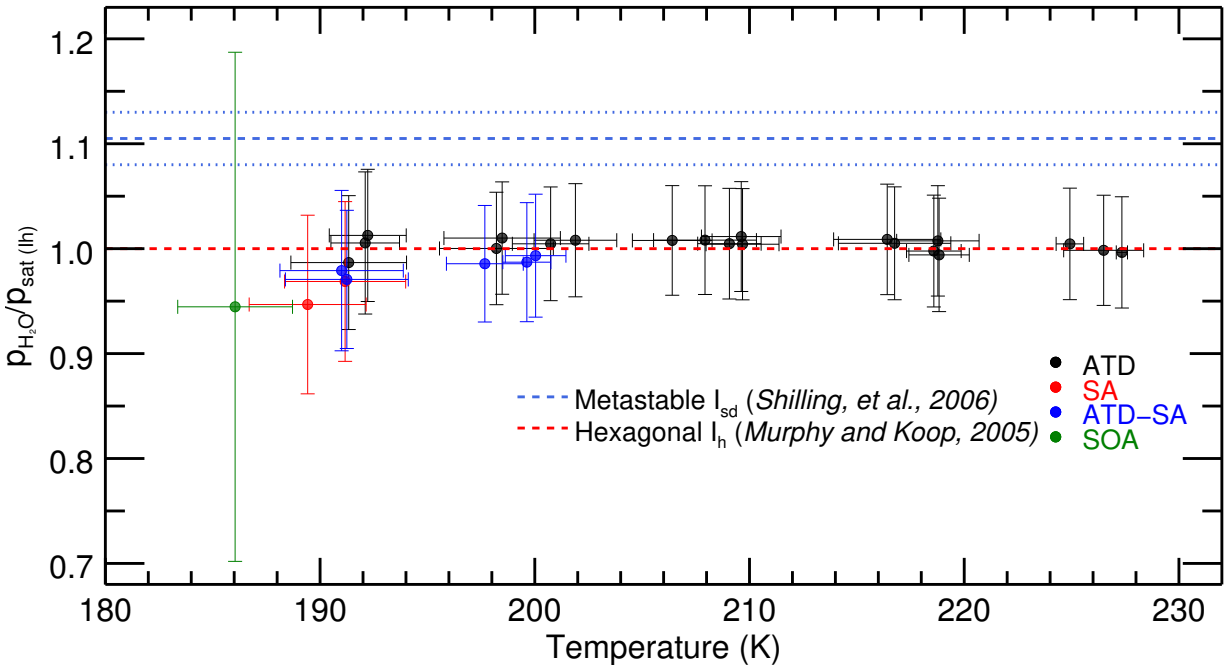

Figure 3.13: Model results under the assumption that the accommodation coefficient is equal to 0.2 instead of one. Experiments are colored by aerosol/IN type and the temperature is the average value during the fit region. On average points shift downward by about 0.5%, and there is a slight increase in model uncertainty.

Figure 3.13 shows the results of the analysis when the model is run under the assumption that the accommodation coefficient is 0.2. Aside from the general decrease in the returned value, there is an overall increase in the width of the calculated error bars, which reflects the model's increased sensitivity to temperature fluctuations. However, this increase is quite small, and overall the model is quite insensitive to changes in accommodation coefficients and the assumption that $\alpha = 0.2$ does not change our interpretation of the results.

Susceptibility to Ice Particle Number

The Welas 1 instrument has a lower diameter cutoff of 0.7 μm, which introduces some potential complications for the analysis. During both nucleation and cloud decay there are a significant number of ice particles smaller than this which will not be counted. These regions are excluded by imposing an average size cutoff of 0.85 μm on the fit range of each experiment. However, this does not address persistent undercounting which may occur for experiments

with low average particle size. Table 3.1 lists the maximum average particle radius for each experiment, and it is clear that at temperatures below 200 K particle size distributions may include a significant number of particles less than 0.7 μm in diameter. This undercounting will result in an overly large estimate of average particle size, and overestimates of per-particle growth rate as well, since fewer particles must account for the observed growth.

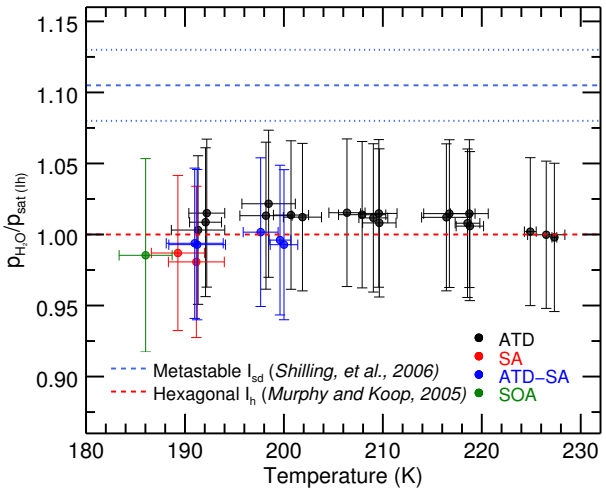

Figure 3.14: Model results under the assumption that the true number of particles in the chamber is 5 times the number measured by Welas 1. Experiments are colored by aerosol/IN type, and temperatures are the average temperature in the fit window.

To get a very rough estimate of the magnitude of this effect we estimate particle size distributions for on of the low-temperature, small ice particle experiments. This estimate is made by fitting a lognormal distribution to the observed properties of the ice cloud. In the fit, the three lognormal parameters and saturation vapor pressure are free parameters, and they are used to estimate the number of ice particles observed by Welas 1, the number of ice particles observed by Welas 2 (which measures at a higher size range), the observed growth rate, and the mass of the ice cloud. These estimates are fit to the observed quantities, and yield physically reasonable values for the three lognormal parameters and the vapor pressure. These fits were performed on 30 second averages of experiments 9, 30, and 32 over the range where Welas 1 measures particle densities greater than 5 cm^{-3}. The results of the fits to experiment 9 show the expected result that Welas 1 is counting almost all the particles

present in the chamber due to their large size. The results of the fits to experiments 30 and 32 suggest that during the period of rapid ice growth just after nucleation the Welas 1 instrument may be measuring as little as 20% of the ice particles in the chamber, and during the established phase of the ice cloud about 50% of the particles are counted.

The latter number is relevant to the fit region, and to test for the presence of bias introduced by undercounting, we rerun the analysis under the assumption that there are 1.5, 2, and 5 times more particles in the chamber than Welas measured. Figure 3.14 shows the results for the 5x particles case. As stated in the main text, there is little movement in retrieved saturation vapor pressure values except at low temperatures, and the largest increase at low temperatures is about 2.5%. These results indicated that even the largest possible undercountings due to small particle size do not change the results presented in this work.

#	Aerosol/IN	T_0	ΔT	P_0	ΔP	$\frac{dn}{dt}/n$	$M_{i,max}$	r_{max}	τ	N_{max}	S_{max}	offset
3	ATD	233.4	-6.4	300	-100	-0.065%	26.1%	6.3	54	38	1.05	1.1
4	ATD	233.4	-9.1	300	-130	-0.091%	27.8%	6.2	67	44	1.09	2.1
5	ATD	233.5	-9.1	300	-100	-0.097%	34.7%	6.0	47	50	1.09	1.8
7	ATD	223.18	-6.4	234	-64	-0.063%	47.2%	3.7	37	90	1.03	0.43
8	ATD	223.3	-8.8	300	-130	-0.095%	60.0%	4.8	34	90	1.03	0.31
9	ATD	223.3	-6.0	300	-70	-0.062%	41.8%	3.9	38	65	1.03	0.24
10	ATD	223.1	-5.6	230	-60	-0.063%	39.4%	3.9	47	70	1.05	0.78
11	ATD	223.3	-8.9	300	-150	-0.096%	61.6%	4.1	30	94	1.09	0.36
13	ATD	213.1	-5.3	235	-65	-0.060%	44.9%	1.7	26	350	1.06	0.21
14	ATD	213.3	-8.4	300	-130	-0.079%	68.0%	1.7	17	480	1.07	0.16
15	ATD	213.3	-5.6	300	-170	-0.060%	40.6%	1.5	18	400	1.06	0.01
16	ATD	213.2	-5.4	234	-64	-0.061%	36.8%	1.5	24	450	1.04	0.12
17	ATD	213.3	-8.4	300	-130	-0.090%	53.8%	1.7	16	600	1.07	0.02
20	ATD	193.7	-4.8	240	-70	-0.055%	93.7%	0.9	66	210	1.18	0.27
21	ATD	193.7	-7.6	300	-130	-0.082%	136%	0.9	40	300	1.24	0.14
22	ATD	193.6	-7.5	300	-130	-0.081%	123%	1.0	54	180	1.28	0.10
24	ATD	204.2	-5.4	300	-70	-0.057%	57.0%	1.3	33	219	1.14	0.15
25	ATD	203.7	-5.0	234	-64	-0.057%	49.9%	1.2	51	193	1.10	0.25
26	ATD	203.8	-8.0	300	-130	-0.087%	79.4%	1.2	26	352	1.10	0.11
27	ATD	203.8	-8.1	300	-130	-0.087%	76..5%	1.2	25	373	1.09	0.10
30	SA	194.0	-7.6	300	-130	-0.083%	93.0%	1.4	138	65	1.90	0.13
31	SA	194.0	-7.6	300	-130	-0.083%	82.9%	1.5	212	39	1.85	0.15
32	SA-ATD	194.0	-7.6	300	-130	-0.083%	101%	1.1	79	115	1.31	0.07
33	SA-ATD	194.1	-7.6	300	-130	-0.083%	127%	0.9	42	250	1.22	0.12
35	SOA	189.0	-7.3	300	-130	-0.080%	116%	1.2	251	50	2.00	0.22
46	SA-ATD	204.1	-5.5	300	-70	-0.057%	39.1%	1.2	44	170	1.11	0.19
47	SA-ATD	203.9	-5.2	234	-64	-0.056%	36.2%	1.2	60	170	1.08	0.24
48	SA-ATD	203.9	-7.6	300	-130	-0.082%	52.3%	1.2	33	280	1.18	0.10

Table 3.1: Table of experiment included in the analysis. T_0 is the base temperature of the experiment before expansion begins, and ΔT gives the decrease in temperature from the start of the experiment to its coldest point. P_0 is the pressure in hPa before expansion begins, and ΔP is the decrease in pressure over the experiment. $\frac{dn}{dt}/n$ is the pumping rate expressed as the percentage of chamber molecules lost per second. This can also be thought of as the percentage of the chamber's volume that is evacuated each second. $M_{i,max}$ is the maximum ice mass in the chamber as a percentage of the vapor mass at the start of pumping. r_{max} is the maximum average ice particle radius. τ is the typical relaxation time in seconds during the portion of the experiment used in the analysis. N_{max} is the maximum ice particle number in cm^{-3}. S_{max} is the maximum saturation observed, typically when nucleation begins. Offset the difference between the scaled APeT measurement and ChiWIS which is subtracted from the rest of the experiment.

Number	Reason	T_0	Aerosol	N_{max}	τ
1	High τ	234	ATD	19	960
2	High τ	234	ATD	7	280
6	High τ	234	ATD	11	176
12	Ref	213	Ref	7	970
18	No Chi-WIS	213	Ref	–	–
19	Ref	194	Ref	4	2810
23	No Chi-WIS	194	ATD	–	–
28	Ref	194	Ref	17	445
29	High τ	194	SA	14	2210
34	Ref	189	Ref	13	1110
36	High τ	189	SOA-HNO_3	3	00
37	No Welas 1	189	SOA-HNO_3	–	–
38	No Welas 1	189	SOA-HNO_3	–	–
39	Ref	223	Ref	1	–
40	Dry Wall	223	ATD	9	–
41	Dry Wall	223	ATD	15	–
42	Dry Wall	223	ATD	16	–
43	Dry Wall	223	ATD	17	–
44	Ref	204	Ref	23	251
45	High τ	204	SA	17	252

Table 3.2: T_0 is the temperature before expansion begins. Aerosol is the type of aerosol or ice nucleus the chamber has been prepared with. N_{max} is the maximum ice particle concentration observed in the chamber. τ is the relaxation time in seconds calculated at the time when N_{max} occurs.

CHAPTER 4

ISOTOPIC WATER VAPOR MEASUREMENTS IN THE ASIAN MONSOON

This chapter focuses on various aspects of the Chicago Water Isotope Spectrometer. Section 4.1 gives a brief overview of the scientific questions ChiWIS is designed to answer, then reviews the constraints on its design. Section 4.2 focuses on the 'nuts and bolts' of the instrument, and is intended to be a resource for new users of the instrument. Section 4.3 give the specifics of the instrument's spectral range and tuning rate. Finally, Section 4.4 covers the steps necessary to fit absorption spectra retrieved by ChiWIS. In general this chapter refers to the configuration of the instrument as it was during the StratoClim Asian Monsoon field campaign, although where modifications have been made as of April, 2018, those are mentioned as well. The ChiWIS discussed in this and subsequent chapters is a completely different instrument than the one discussed in Chapter 3.

4.1 Design goals and constraints

4.1.1 Science motivation

The TTL is an important region for current and future climate. It is the main pathway by which tropospheric air ascends into the stratosphere [Brewer, 1949], and is the coldest region of the lower atmosphere (at times $T < 185\ K$). Air ascending through the TTL is dehydrated by formation of high-altitude cirrus, which are radiatively important, producing a total radiative forcing of $4\ {}^{W}/_{m^2}$ over the tropics [Haladay and Stephens, 2009]. TTL cirrus distribution and amount are directly affected by deep convection, since intense convective cells carry large amounts of ice to the tropopause level and above. [Danielsen, 1982, Corti et al., 2008]. They are also *indirectly* affected by post-convective water vapor distributions: back-trajectory calculations link observed in-situ cirrus to areas of prior convective activity

[Reverdy et al., 2012]. Water vapor concentrations in convective detrainment plumes can be increased by more than a factor of two above their surroundings and appear to persist for days to weeks [Hanisco et al., 2007]. The link between deep convection and high-altitude cirrus is an important potential positive feedback in a changing climate. A warmer world may experience more frequent and vigorous deep convection, which would beget more high-altitude cirrus clouds that contribute to warming.

In-situ measurements of water isotopologues can help reveal how convective detrainment of water vapor contributes to later cirrus formation. Convectively lofted ice is isotopically heavier than surrounding vapor since the heavier isotopologues (e.g. HDO and $H_2^{18}O$) preferentially partition into the condensed phases [Wahl and Urey, 1935]. As this lofted ice sublimates, its isotopic signature is imprinted on the TTL. Both remote sensing [Nassar et al., 2007] and in-situ [Hanisco et al., 2007] instruments have measured isotopic profiles that show an increase with altitude in the TTL, likely due to the sublimation of lofted ice. These profiles provide information about the importance of convective detrainment of vapor and ice relative to other sources and sinks in the overall water budget. Isotopic measurements within cirrus can also shed light on the importance of in-cloud processes to their formation, maintenance, and distribution in time and space.

The AM is an especially interesting area for TTL water isotopologue measurements. The AM may contribute up to 75% of the upward water vapor flux to the tropopause in Northern Hemisphere summer (e.g. [Gettelman et al., 2004, Kremser et al., 2009]. Recent analysis of ACE-FTS satellite data [Randel et al., 2012] shows significant differences in water vapor isotopic enhancement between the North American and Asian monsoons (Figure 4.1), suggesting differences in water transport processes, but no in-situ water isotopologue measurements in the AM have yet verified this observation. High-altitude measurements of the AM are extremely limited in general, and StratoClim will provide a valuable new perspective on this important region.

In-situ isotopic measurements of water vapor isotopologues at near-tropopause altitudes

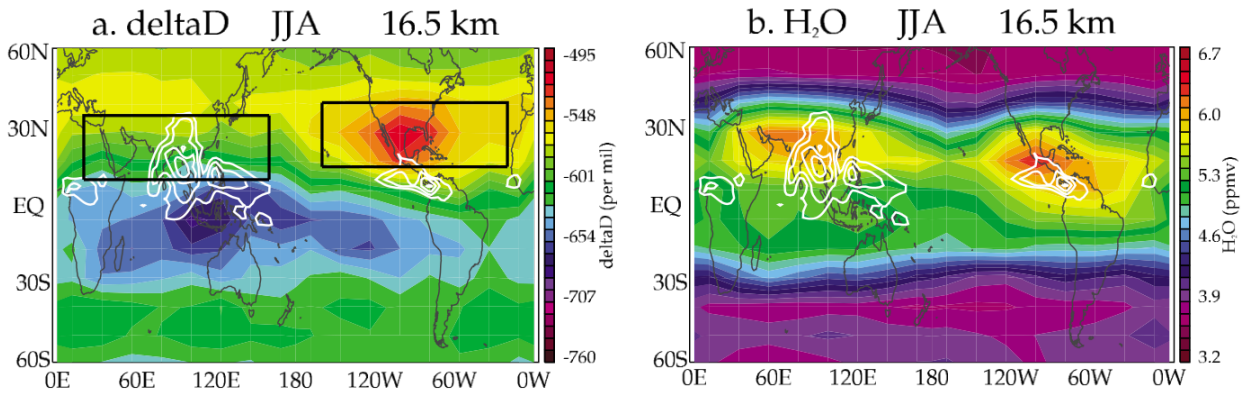

Figure 4.1: Right panel shows the JJA average 16.5 km ACE-FTS retrievals of water vapor. Both the North American and Asian Summer monsoons show strong signals. The left panel shows JJA average 16.5 km retrievals of δD. A strong enhancement is visible in the NAM, but the AM shows now enhancement over surrounding regions.

have been made outside the AM by several instruments. The ALIAS instrument [Webster et al., 1994] flew aboard NASA's ER-2 and WB-57 aircraft and made trace gas measurements via TDLAS using a 100-meter optical pathlength. ALIAS reported water isotopologue measurements to 17 km during the CRYSTAL-FACE campaign [Webster and Heymsfield, 2003], but has limited sensitivity at high altitudes. The Harvard ICOS (TDLAS with a high-finesse cavity for a 4.5 km pathlength and increased sensitivity; Sayres et al. [2009]) and HOxotope (laser-induced fluorescence; Clair et al. [2008]) instruments obtained water isotopologue measurements aboard NASA's WB-57 aircraft on campaigns from 2005-2007, and detected isotopically enhanced convective plumes in the stratosphere during the North American monsoon [Hanisco et al., 2007]. Neither instrument is however scheduled for further flights; the Harvard ICOS instrument was fully rebuilt at a different wavelength and has not been field-tested. The University of Gottingen IRIS instrument also used cavity-enhanced techniques and flew on the M55 Geophysica during the AMMA campaign to sample the African monsoon, but showed limited sensitivity even given 30-second averaging. Recently, the lightweight ISOWAT instrument (TDLAS with a 76-meter optical path, Dyroff et al. [2010]) was developed at the KIT-IMK for measurements in the mid to upper troposphere, but is insufficiently sensitive for TTL measurements. ChiWIS was developed to meet the

need for new instrumentation capable of water isotopologue detection in this scientifically important region.

4.2 The Chicago Water Isotope Spectrometer

The Chicago Water Isotope Spectrometer (ChiWIS) is an ICOS device designed to measure HDO and H_2O aboard the M55 Geophysica during the StratoClim field campaign. The remainder of this chapter is devoted to the layout and operation of the instrument.

4.2.1 Overview of the Instrument

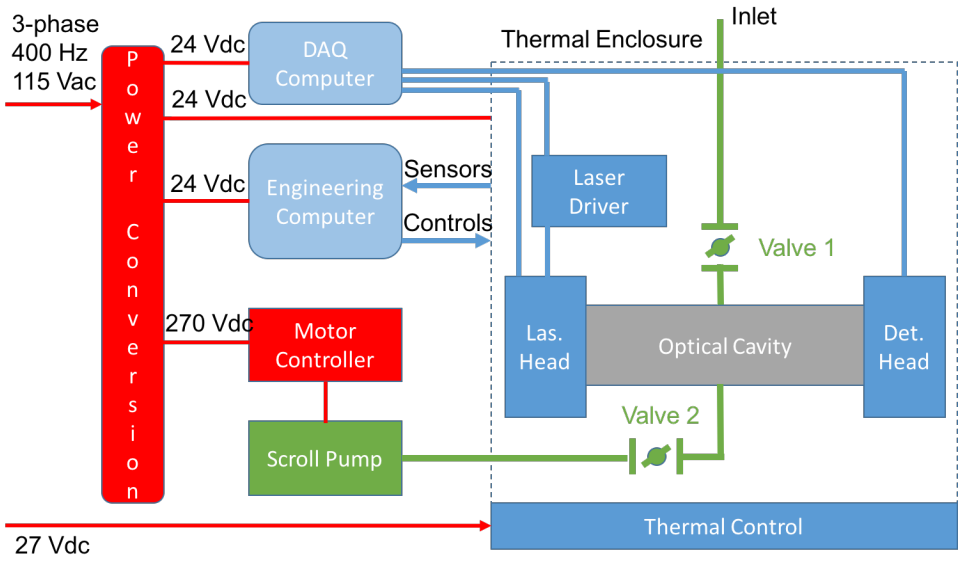

Figure 4.2: Block diagram of major ChiWIS subsystems. Aircraft interface, power conversion, and thermal control of the optical bench are addressed in section 4.2.5. The engineering computer, DAQ computer, laser driver, and motor controller are covered section 4.2.6. The optical bench is described in section 4.2.8, and the scroll pump, valves, and inlet are all described in section 4.2.9.

The ChiWIS design is, in broad terms, similar to the instrument design presented in [Sayres et al., 2009]. Both are instruments with 4" mirrors designed to operate in the dry regions of the UT/LS. Whereas that instrument operated at 6.7 microns and required the use

of such large mirrors due to the large diffraction-limited spot size and lower beam quality at that wavelength, the choice to use such large mirrors in ChiWIS was made out of an abundance of caution. Spot sizes are smaller and beam quality generally better at 2.65 microns, but it was unknown whether significantly smaller mirrors could successfully be used at this still relatively long wavelength. (In this instrument electrical noise turns out to be the limiting factor, so it seems that smaller mirrors and a smaller spot pattern would have been acceptable.)

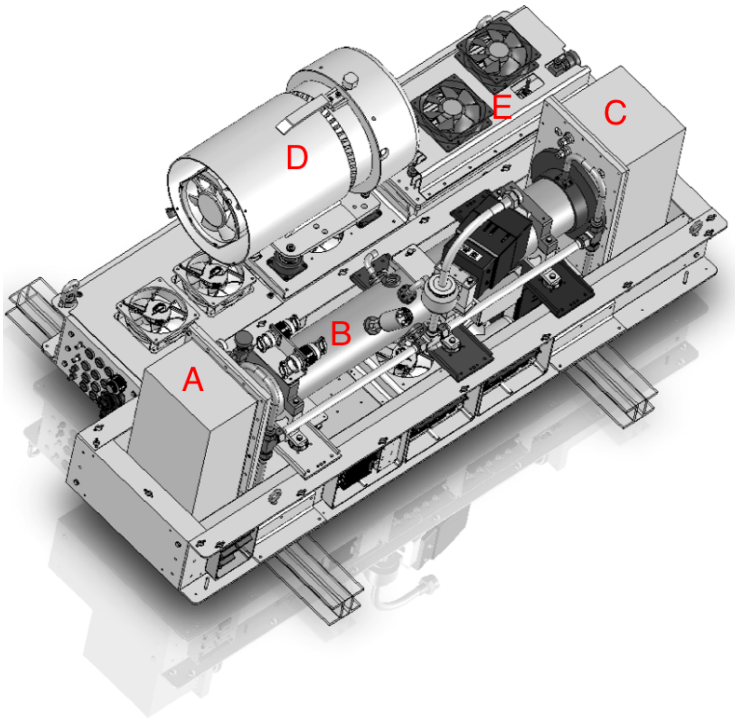

Figure 4.3: Layout of the Chicago Water Isotope Spectrometer. Visible subsystems are labeled as follows: A is the laser head pressure enclosure. B is the optical cavity. C is the detector head pressure closure. D is the modified scroll pump and E is the DAQ pressure enclosure.

The major ChiWIS subsystems include power distribution, gas handling, the optical bench, thermal control, and computers and electronic control. Each of these subsystems will be discussed below, with the goal of imparting to the reader enough of an understanding of the instrument to operate and maintain it.

4.2.2 Spectral region

The prior version of ChiWIS used at the AIDA chamber had a spectral region between 3788 and 3791 cm^{-1}, which had several H_2O lines and a relatively strong HDO line. However, the AIDA chamber used air free from contaminants like N_2O, CH_4, and CO_2, all of which can confound water vapor measurements in the mid-infrared. In fact, the HDO line used at AIDA is unusable at typical concentrations in the UT/LS due to an underlying methane line.

An exhaustive search was performed in the mid-IR for a spectral region that, a) contained an HDO line with no significant underlying spectral features that was far from any large water lines, and b) had water lines near enough to the HDO line that both could be swept over in one ramp of a laser ($\approx 2\ cm^{-1}$). The target HDO line had to be strong enough to be resolvable in the presence of $\approx 1 \times 10^{-4}$ noise at concentrations found in the coldest and driest parts of the UT/LS, where water vapor can be as low as 3 ppm and the HDO/H_2O depletion is around -700‰. Ideal spectral lines are those that have low ground state energies and therefore have linestrengths which are relatively temperature insensitive around room temperature.

The best candidate found by this search was the HDO line at 3776.9 cm^{-1}. It is uncontaminated by any other species, and its linestrength has low temperature dependence. Within the tuning range of the laser, there are two suitable water lines that can be used to retrieve H_2O concentrations. Neither of these lines is ideal (one is overly intense, and the other is overly weak), but taken together they provide enough dynamic range to cover the whole range of mixing ratios ChiWIS sees in the UT/LS.

Table 4.1: Major spectral lines used in StratoClim and selected parameters.

Molecule	ν_0 (cm^{-1})	Line Strength	$\gamma_{C0_{foreign}}$	E_0	s
H_2O	3777.94924	2.715e-21	0.0973	173.3658	0.72
HDO	3776.90008	1.639e-23	0.1046	150.1563	0.90
H_2O	3776.44401	2.610e-23	0.1005	1634.9671	0.76

Figure 4.4 shows a typical absorption profile from StratoClim, this time with mixing ratio of about 50 ppm. Even at this relatively low mixing ratio, the 'big' water line is nearing saturation. At mixing ratios higher than about this point, it is essential to have the smaller line at the top of the ramp to act as a check on the big line. Near optical saturation spectral features can become difficult to fit.

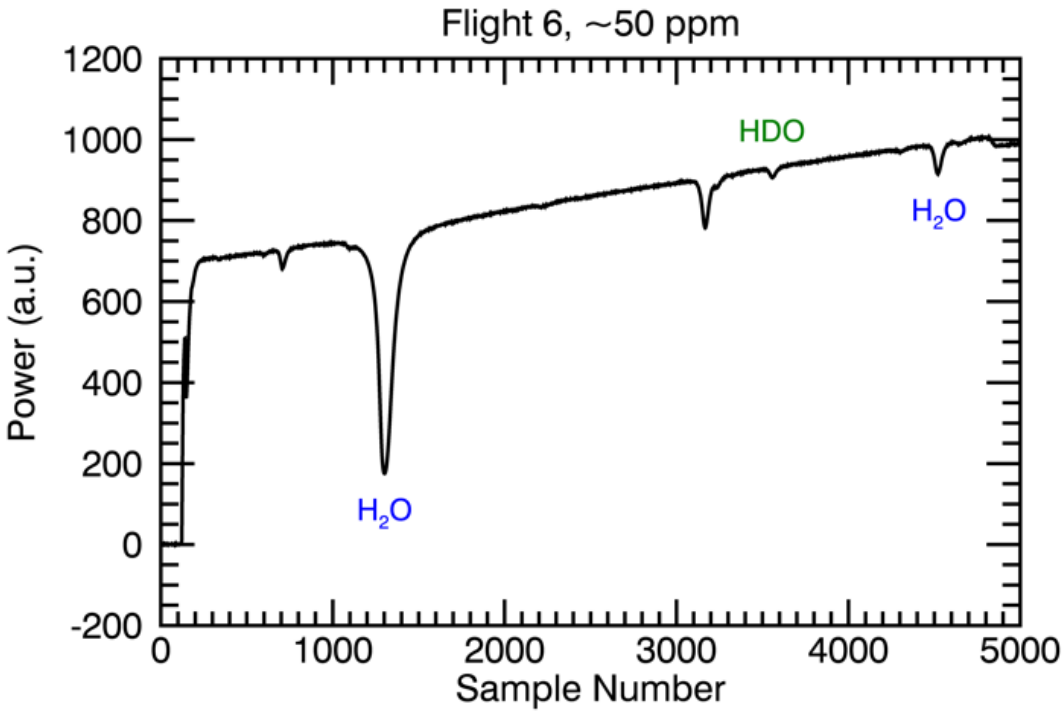

Figure 4.4: Spectrum from Flight 6 of StratoClim. This ramp shows the three important lines measured, and whose properties are shown in Table 4.1.

4.2.3 The M55 Geophysica

The M55 Geophysica is a high-altitude research aircraft designed, owned, and operated by the Myasichiev Design Bureau (MDB). The Geophysica was originally intended to hunt high altitude spy planes (like the American U-2) and balloons, but was repurposed into a geophysical research platform at the end of the Cold War. The aircraft is subsonic (M $\approx$ 0.7) and has a typical cruising altitude of 17-21 kilometers with a scientific payload. The

aircraft's range is 3500-4000 kilometers depending on its payload and cruising altitude, which corresponds to flight times of about 4.5 hours.

Figure 4.5: The M55 Geophysica in flight. ChiWIS was housed under the bubble-like dome atop the aircraft, along with the AMICA and COLD instruments.

The aircraft can accommodate about 20 instruments spread across several wing mounted pods and bays in the nose, body, and on top of the aircraft. During the StratoClim campaign ChiWIS was housed in the Bay IX, also known as the MIPAS dome or dorsal bay (Figure 4.5). This bay has a payload limit of 300 kilograms and housed three instruments during StratoClim. The aircraft was rewired before the campaign to provide 1550 Watts of 115 Vac, 400 Hz 3-phase power and 300 Watts of 27 Vdc for ChiWIS.

4.2.4 Design requirements

Several hard constraints drove the design of ChiWIS. The first was the conservative choice of 4" diameter mirrors to ensure suppression of optical noise. These large diameter mirrors increased the total volume of the cell and required a powerful pump to flush the cell once every two seconds. The second major constraint was the partitioning in Bay IX of most of the power available to ChiWIS into 3-phase, 115 Vac instead of 27 Vdc, which made it more difficult to find commercial components. The need for a more powerful pump ruled out all available commercial options and by the power available in the Geophysica's MIPAS bay.

Weight and total electrical power were not strong constraints in the design of this instrument, although the instrument did have to fit in a given footprint within the MIPAS

dome.

4.2.5 Power Distribution

Interface with aircraft

ChiWIS interfaces with the Geophysica through three mil-spec connections. One connector (p/n MS3102A22-22P) brings 27 Vdc to the instrument and another (p/n D38999/20FE6PN) brings three-phase 115 Vac, 400 Hz power to the instrument. The third connector (p/n D38999/20FB35PN) allows limited communication with the aircraft. MDB requires that each instrument outputs an instrument OK/fail signal, which ChiWIS derives from the watchdog signal on the PXIe power supply board. If the instrument fail light appears in the cockpit, there is the option for the pilot to cycle the instrument's power up to three times in order to get it to reboot. There is also the option for housekeeping data (temperature, lat/lon, altitude, etc.) to be read from the UCSE instrument over a serial connection, although this was never implemented in ChiWIS.

Power Conversion and Distribution

The power distribution system in ChiWIS is divided into two parts. One subsystem distributes 27 Vdc power from the aircraft to the Minco heaters which thermally control the optical bench, and the other converts three-phase power into 270 Vdc, which is then distributed to the motor controller and DC-DC converters which supply various subsystems.

From the 27 Vdc connector, power is routed through a 15 amp breaker to a 12 amp fuse. Power is then distributed from the fuses to the upper and lower enclosures of the optical bench. This subsystem is subject to no computer control and exists to ensure that the optical bench stays at room temperature throughout a flight, even if all computer systems fail.

The ac subsystem is significantly more complex. Power flows from the connector and passes through a 5 amp 3-phase breaker before each phase passes through a 5 amp fuse.

From the fuses, the 3-phase power passes to a custom printed circuit board (PCB) which converts 115 Vac/3-phase power to 270 Vdc. The PCB is built around around a SynQor 3-phase line filter (MACF-115-3PH-UNV-HT) and SynQor 3-phase power factor correction module (MPFC-115-3PH-270-FP).

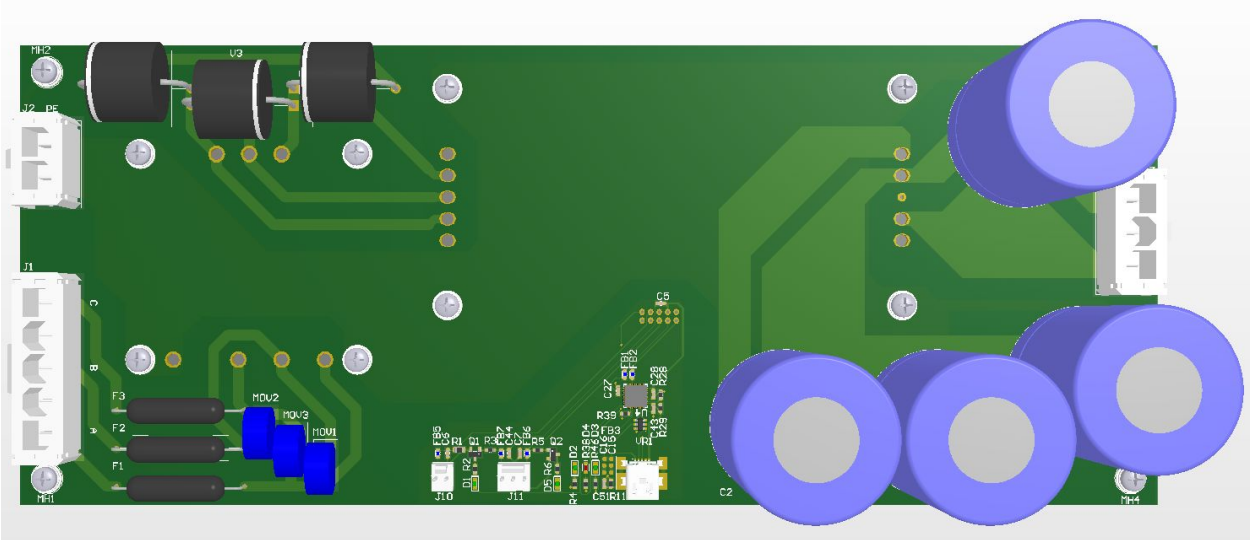

Figure 4.6: Layout of the AC-DC converter used in ChiWIS during the AM field campaign.

Figure 4.6 shows the layout of the 3-phase AC-DC converter in ChiWIS. This board was designed and layed out by Design Criteria, Inc. (Roy, UT). The large connector at bottom left takes the 3 phases, labeled A, B, and C, and the connector at the top takes the neutral provided from the aircraft. The connector for the three phases is oversized with the inputs on every other pin to minimize the possibility of arcing at high altitude. Three phase power from the aircraft is provided in a wye configuration, but the converter module doesn't need the neutral and it is only used to provide shielding on the board.

Before entering the line filter the three phases go through a network of fuses and Metal Oxide Varistors (MOVs). The fuses provide an added layer of protection beyond what is already present elsewhere in the instrument, and the MOVs suppress voltage spikes before they enter the board. Varistors are devices that are essentially non-conductive between a positive and negative clamping voltage, but highly conducting outside that range.

The 3-phase AC line filter is essentially a complicated RLC network that passes voltage

in the 60-400 Hz range, but provides 45 dB of noise suppression at 200 kHz. It has low resistance (< 200 mΩ) and can output up to 6 A_{rms}.

After passing through the line filter, current flows through a network of transient voltage suppression diodes (TVS). These diodes behave similarly to MOVs, but have a lower clamping voltage and are less prone to degradation over time. From these diodes the current passes into the SynQor MPFC module.

This module uses active power factor correction (PFC) to convert 3-phase, 115 Vac into 270 Vdc. The first stage in this unit is a PFC rectifier which converts the AC input to DC. Active power factor correction works to keep the current in phase with the voltage, resulting in less overall power consumption and more efficient delivery to the output. The second stage is a boost converter which takes the loosely regulated output from the PFC rectifier and converts it to the regulated 270 Vdc output. The midbus and VOUT+ are connected to a network of metal film capacitors which filter the output and act as a holdup capacitor in case of a power brownout. These capacitors, while overly large, were selected to safely operate up to 70,000 feet – electrolytic capacitor can explode at high altitudes due to the low pressure. *It is very important to note that the outputs are not isolated with respect to the inputs, and VOUT- should not be connected to the instrument/chassis ground, and should float to the inputs of the motor controller or Vicor Boards without any other connections.* The module can operate between -50 to +100° C, and can source up to 1.5 kW of power.

The SynQor modules are both mounted on the back of the board, and are be mounted onto a heat spreader plate and attaches to the rail of the instrument which acts as a heat sink. Thermal paste or a thermal pad should be placed between the units and the spreader plate, and thermal paste should be placed between the spreader plate and the rail to facilitate heat transport to the heat sink.

DC voltage leaves the board through the 3-pin connector on the right, and from that point is split three ways. One line goes to the motor controller, which is discussed in subsection 4.2.6, and the other two go to identical Vicor boards (ACOM536-951), which are DC-DC

converters. Each Vicor board has a 270 Vdc to 24 Vdc converter (VI-263-MU) and a ripple attenuation modulator (VI-RAM). The converters were chosen due to their rugged design and ability to operate at low pressure and their high power densities. Each converter can supply up to 200 W of power, and can operate from -55 to 85° C. The Vicor boards power the computers, optical bench, and precision heaters throughout the instrument.

4.2.6 Electronics and Control

Control of ChiWIS and measurement of engineering data and spectra is accomplished with two computers located in the pressure controlled DAQ enclosure. The computers can be accessed through a hermetic Ethernet pass-through to download data or update software without removing the enclosure lid. What follows is a description of the the basic subcomponents of each computer, the software they run, and the subsystems they control.

Engineering computer

The engineering computer is a Diamond Systems Athena III PC/104 single board computer (SBC). PC/104 is a small, stackable form factor that is often used in applications requiring a rugged computer. The Athena III combines processing, memory, and I/O management on one board, to which modular accessory boards can easily be attached. It also comes with a gigabit Ethernet port, 4 serial channels, and a 50 pin I/O header. The 50 pin header has 24 digitial in/outs, sixteen single-ended analog ins, and 4 analog outs which are used to retrieve engineering data and control subsystems elsewhere in the instrument.

In ChiWIS the Athena III is attached to five accessory boards. The first is the Jupiter-MM power supply module. This unit takes 24 Vdc, and converts it to the 5/12 Vdc levels used by the Athena III and its accesories. The remaining four boards come in two pairs. Each pair is composed of a digital multimeter (Diamond Systems DMM-32DX-AT) and a custom signal conditioning board (ACOM536-953). The DMM boards are PC/104 form factor boards which have 32 analog inputs with 16-bit resolution, 4 analog outs with 16-bit

resolution, and 31 lines of digital I/O. The inputs can be sampled at a maximum rate of 250,000 samples per second. The signal conditioning board takes the raw voltages measured from thermistors, AD-590 sensors, pressure gauges, etc, and conditions the voltages to a range compatible with the inputs on the DMM boards.

When the Athena computer is powered, it automatically loads a LabView program, ACWIS.vi. This program reads and logs data, controls subsystems of the instrument, and provides a first layer of safety in software. The program consists of three modules. The first module reads in data from sensors and gauges in the instrument and writes that data to disk. The second module takes this data and makes 'decisions' based on it. For example, if the pump head temperature has been greater than a certain value for more than a minute, then the program will decide to reduce the pump RPMs. The last module of the program loops through all the decisions taken, and executes them by sending serial commands to subsystems, adjusting analog voltages, or flipping digital outs.

This software is designed to operate independently during flight, but can also be operated in 'lab mode' for tests in the laboratory or programming. To access the Athena, a secondary laptop computer is connected to the ethernet feedthrough located on the lid of the DAQ enclosure box. Once the instrument is powered up, the computer can be accessed through Windows Remote Desktop (WRD) on the remote computer. The Athena computer is named 'pallas', and its username and password are 'Y' and 'hindsight', respectively. Once logged in, the frontend of ACWIS.vi will appear, an the user can operate the pump, valves, and laser, or stop the program and edit it. Files can be downloaded from the Athena to the laptop using WRD by copying them into a shared folder located on the laptop.

Data acquisition computer

Data is acquired using a dedicated data acquisition computer purchased from National Instruments, part number PXIe-1071. The chassis was removed from the computer and the boards assembled into a custom, vibration-isolated frame in order to fit in the computer

enclosure. The PXIe-1071 comes with three sub-components, an NI PXIe-8820 embedded computer, an NI PXIe-6124 simultaneous sampling multifunction IO device, and a backplane through which the two connect.

The PXIe-8820 runs NI Real-Time Phar Lap ETS 13.1 and provides basic I/O functionality through a DisplayPort, an RS-232 serial part, a parallel port, four Hi-Speed USB ports, and one GigaBit Ethernet jack. Typically the computer is accessed remotely through the Ethernet connection using a laptop running LabView 2016 Real-Time or NI-MAX to update software or edit the system configuration. WinSCP is used to download data to a remote laptop.

The PXIe-6124 device has 4 independent, 16-bit differential analog inputs that can sample at 4 megasamples per second, each. In StratoClim, this card sampled two channels, one from the signal detector and one from the reference detector in the laser head. It looks at two different triggers, one for regular sampling of the full spectra, and one for sampling ringdown data at the end of each ramp.

Data is acquired using the LabView program DAQDAQ.vi. This program can be edited on the remote laptop and uploaded to the PXIe using LabView Real-Time 2016. The data is recorded in the binary .bdt format, the layout of which is given below. Each file is composed of three sections. The first is a 128-byte file header that contains general information about the scans, and is layed out in Table 4.2. Default values for the StratoClim campaign are given where applicable. The reference time in bytes 2-5 is recorded in the LabView format as a number of seconds elapsed since midnight on January 1, 1904 UTC. The first 64-bit integer is the fractional number of seconds recorded as a 64-bit integer, which must be divided by 2^{64} before being added to the integral seconds contained in the second 64-bit integer. The millisecond time recorded in the sixth 32-bit unsigned integer is the value of the computer's clock in milliseconds at the moment the reference time is recorded.

The second block is a series of scan headers, one for each recorded ramp. In StratoClim these scan headers consist of 4 unsigned 32-bit integers, and their uses are shown in Table

Table 4.2: Format of file headers in the .bdt format. The offset is measured in 32-bit unsigned integers from the beginning of the file.

Offset	Type	Function	Default
0	Char x 4	File ID	Bdat
1	Byte x 4	Version	0.0.1.0
2-3	64-bit Signed Integer	Reference Time (fractional seconds)	NA
4-5	64-bit Signed Integer	Reference Time (integral seconds)	NA
6	32-bit Unsigned Integer	Reference Time (milliseconds)	NA
7	32-bit Unsigned Integer	bits/sample	16
8-9	64-bit Double	Volts/bit Channel 1	3.2043456e-05
10-11	64-bit Double	Sampling dt	2.5e-07 seconds
12-13	64-bit Double	Volts/bit Channel 2	3.2142972e-04
14-29	32-bit Unsigned Integer	Unassigned	NA
30	32-bit Unsigned Integer	Ramps/file	NA

4.3. The first integer is the number of milliseconds elapsed since the reference time. The time at which the ramp occurred can be retrieved by dividing this number by 1000 then adding it to the reference time. The next integer gives the offset in bytes from the start of the file of the data for the given ramp. The next integer gives the number of *samples* associated with each ramp. This number is the product of the number of channels used and the number of samples/channel that DAQDAQ.vi is commanded to record. The last unsigned integer is divided into three subcomponents. The first, a 16-bit integer, is reserved for linking to a potential parameter file, but was not used in StratoClim. The next 8 bits show which channels were used in recording the data. In StratoClim the active channels were 1 and 3, so this value is 9 throughout the campaign. The last 8 bits are flags, which can be set to indicate characteristics of the recorded data. In StratoClim the least significant bit of this is used to distinguish between ringdown and signal data. Ringdown data is set to '1' and signal data is set to '0'.

After the scan headers the scan data for each channel is recorded as a series of signed, 16-bit integers. In the StratoClim data, there are two recorded scans for each laser ramp.

After each flight, data is downloaded to a remote computer using WinSCP. The solid-state hard drive in the PXIe can record about 8 hours of data before it is full.

Table 4.3: Format of scan headers in the .bdt format. The offset is measured in 32-bit unsigned integers from the beginning of the file.

Offset	Type	Function
0	Time (milliseconds)	32-bit Unsigned Integer
1	Offset to data (bytes)	32-bit Unsigned Integer
2	Samples/ramp	32-bit Unsigned Integer
3	Parameter Block/channels/flags	see text

PXIe Power Supply

The PXIe Power Supply (ACOM536-957) serves two purposes. The first is to generate the +12 and +5 Volts needed to power the PXIe data acquisition computer and onboard logic, and is done using a BetaDyne DC-DC converter (150S12/24X). The second is to evaluate a watchdog signal sent from the Athena engineering computer. If this signal is not present (indicating that the engineering computer has failed), the watchdog chip outputs a FALSE signal, which goes through AND gates with on/off bits generated by the engineering computer that control critical subsystems like the laser and optical bench. This ensures that regardless of the engineering computer's failure mode, critical subsystems will be turned off. Other on/off bits simply pass through the board, and all signals are buffered before being output to the rest of the instrument.

Optical Bench Power Supply

The Optical Bench Power Supply powers several critical subsystems, including the laser driver and the thermoelectric coolers for the laser and detector chips, and passes through power and signal for pressure sensors and the MKS valves.

This board has two 24 to 12 V DC-DC Beta Dyne converters (EBL30S12/24X) which are wired to generate ±12 Volts for the laser driver board. These power supplies take the 'LAS ENA' signal from the PXIe power supply as an input on their on/off pins, and therefore can only be activated if the Athena first activates the Laser TEC.

A 24 to 5 Volt DC-DC Beta Dyne converter (EBL30S5/24X) powers the laser and detector

TECs, and mixing fans in the laser and detector enclosures. Power to the laser TEC is controlled by an electronic switch that opens and closes with the LAS TEC ENA signal.

Due to an error in design, a small voltage source had to be added to this board in order to power the logic chips. This voltage is always on, independent of the OB ENA signal.

Preamp Power Supply

The amplifiers are powered by the clean, Preamp power supply board (ACOM536-956). This board takes +24 Vdc from the optical bench power supply and generates clean, ±15 Vdc power using a BetaDyne converter (LN10D15/24X) and EMI filter (PFL100X). The Preamp Power Supply is highly configurable in terms of how grounds are connected to each other and to the instrument chassis. This is done in order to give the user options for electrical noise reduction.

Ramp Generator

The ramp generator was custom made by the University of Chicago Electronics Design Group. It is composed of two PCBs, one of which generates a voltage wave form which is then converted to current by the second board. The current is output directly to the laser diode.

Four aspects of the ramp generator's functionality are programmable: the initial current I_L, the final current I_H, the ramp length t_r, and the time between ramps t_g. The output current I given by the formula $I(t) = I_L = [(I_H - I_L)/t_r] \times t$. The ramp shapes are generated by an FPGA on the current driver control module, which can, in principle, be programmed to output an arbitrary shape. Figure 4.7 shows the waveform used in StratoClim.

The current controls can both be varied between 0 and 560 mA in 1024 steps, and the two control times can be varied from 64 microseconds to 64 milliseconds in 1024 steps. The current is calculated every microsecond with 46-bit accuracy, and the 16 most significant bits are sent to the DAC. From there, the voltage signal is amplified, then sent to the current

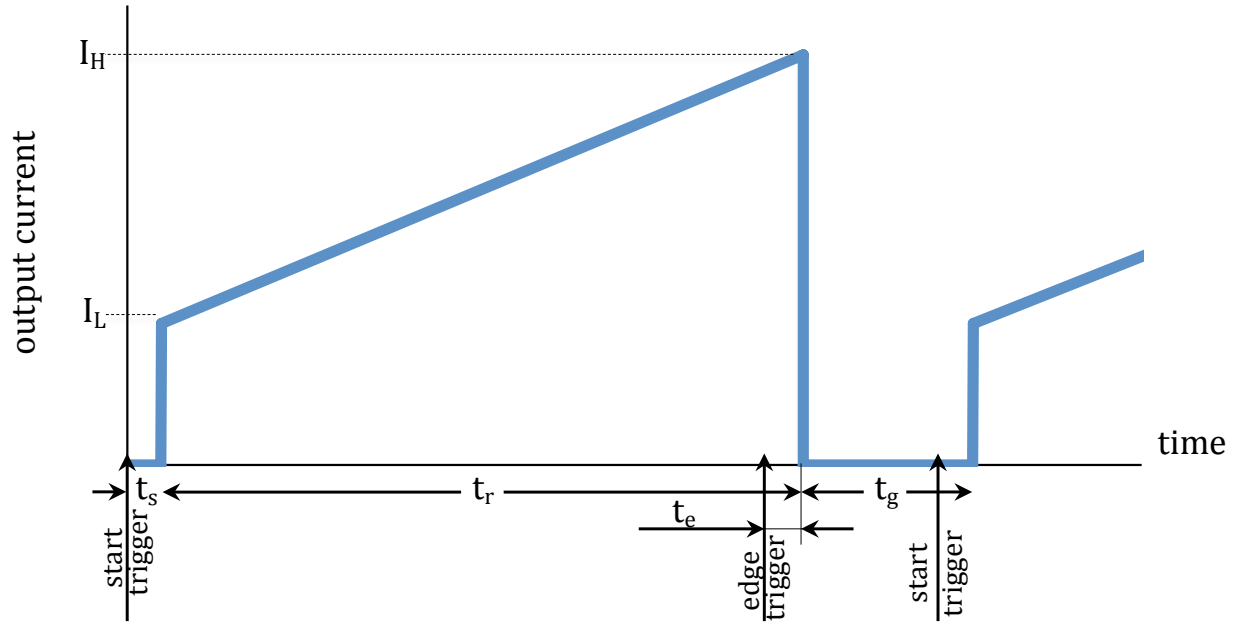

Figure 4.7: The initial current (I_L), the final current (I_H), the ramp duration (t_r), and the time between ramps (t_g) can all be programmed through ten-bit dip switches located on the current source control module.

driver, which outputs the current ramp to the laser diode.

The ramp generator also emits two timing pulses which the data acquisition computer uses to start data collection. The two pulses are denoted as 'edge trigger' and 'start trigger' in Figure 4.7. The start trigger indicates the onset of a full ramp of data, and the edge trigger indicates the ramp is about to end, at which point ringdown data can be taken. The falling edge of the ramp is generated in such a way so that it falls from the max current to 0 amps in less than one microsecond. This ensures that the observation of the cavity ringdown is not confounded by a slow falling edge to zero.

The current driver control module has two TTL inputs. Both must be set high before the board will drive current through the laser diode. The first signal comes directly from the PXIe power supply board, which ANDs together the digital signals from the Athena computer which activate the laser TEC and ramp generation. This ensures that the generator will not drive current through the laser when the laser TEC is off.

The second signal comes from the window comparator circuit on the Wavelength board,

which tests the temperature reported by the laser TEC to ensure that it is within a prespecified range. This provides another layer of thermal protection for the laser diode.

Motor Controller

The motor controller is a Sensitron configurable digital motor drive module, part number SMCV6G050-060E. This device uses pulse width modulation (PWM) to approximate variable voltages and frequencies. In this device, the 270 Vdc input is chopped at very high frequencies (6-25 kHz), and the duty cycle of the pulse width modulation can be varied. From the point of view of the motor, this PWM is averaged out, so varying the duty cycle is essentially the same as varying the voltage applied to the motor.

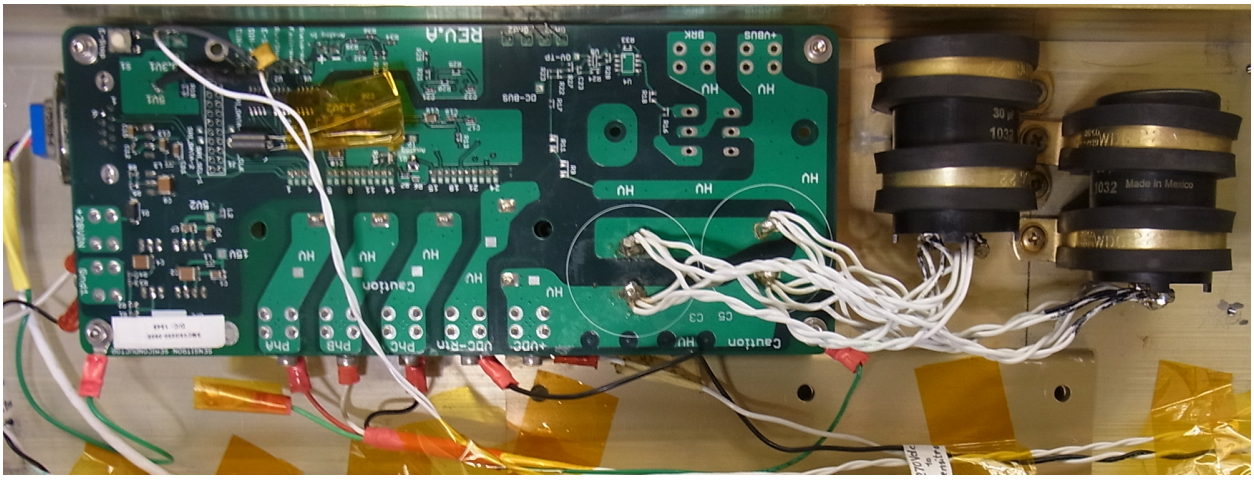

Figure 4.8: Photograph of the Sensitron motor controller. The large metal film capacitors at right were originally mounted on the board, but were subsequently removed to take up less space. The 270 Vdc and DC return are the bottom right two connectors on the board, and the 3-phase power constructed by the controller's pulse width modulation exit the unit through the connectors labeled PhA, PhB, and PhC along the bottom. The RS-232 connection and +24 Vdc power for the board are at right.

The motor controller is highly configurable through a Windows program provided by the Sensitron corporation. During the StratoClim campaigns the controller's current limit was set to 5.24 A_{rms}. This was sufficient for high altitude use, but often could not start the motor during lab use, or maintain an RPM setpoint for more than about 45 minutes at a

time. To resolve this problem the set point was set to 6 A_{rms} with the approval of Sensitron and Kollmorgen.

One major benefit of this class of variable frequency motor controller is that they do not have a large inrush current upon startup. This eases design constraints elsewhere since one no longer has to worry about big current spikes blowing fuses or interfering with other instruments upon motor startup. One drawback is that the constant high-frequency switching used to build the PWM signal can be a significant source of noise in high-precisions measurements, although the motor controller does not appear to be a significant source of noise is the case of ChiWIS.

4.2.7 DFB Laser

The Microdevices Laboratory (MDL) at the Jet Propulsion Laboratory (JPL) generously provided ChiWIS with two, 2.65 micron lasers for use in the StratoClim campaign (p/n V0954_3_29-30_62 and V0954_3_27-28_67). These lasers are high-power ($>$ 20 mW), tunable, single-mode, GaSb based distributed feedback (DFB) diode lasers. They were intentionally designed around the HDO line at 3776.9 cm^{-1}, and more detail can be found about them in [Briggs et al., 2013]. They are estimated to have coherence lengths of about 100 meters.

Both DFB lasers were repackaged with a collimating asphere (390029IR4-00, LightPath Technologies) inside the laser can. The asphere is molded from the chalcogenide optical material BD-2, which has a high index of refraction comparable to ZnSe. This asphere's coating has a reflectance of less than 1% per side. This small optical component collimates the beam well enough that no telescope is needed to shrink the beam after the asphere. The first of the lasers listed above was the one used in the StratoClim campaigns. The second laser has a mode hop which restricts the ramp that can be used due to its position very near the HDO line over a large temperature range.

4.2.8 Optical Setup

ChiWIS optics are divide up into three subcomponents. The first is the laser head, which houses the DFB laser described in section 4.2.7, the reference detector, and a free space etalon for determining the tuning curve. The second subcomponent is the optical cavity itself, which is composed of two highly reflective mirrors which trap light and result in very long path lengths in the cell. The last component is the detector head, which houses the ZnSe collection optics and the detector. The laser and detector heads are both within environmental enclosures which maintain pressure in order to preserve optical alignment and promote heat transfer. Each subcomponent will be described in detail below.

The wavelength of light at which ChiWIS operates also interacts very strongly with OH bonds found in impurities in most optical materials. All thick optical components had to be constructed out of very pure materials like Infrasil and ZnSe to avoid significant transmission losses.

Laser Head

The laser head is electrically accessed through three pass throughs and has two valves through which dry air can be passed before measurements. The laser optics are all mounted on black anodized aluminum breadboard which has been cut down to fit within the pressure enclosure. After collimation the beam is reflected through a wedged window and into a beam splitter, which reflects about 5% of the incident light into reference detector, and passes the other 95% into the injection mirror. The wedged window is used to spatially separate the back reflections off the beam splitter so that light does not go directly back into the laser.

The reference detector signal exits the enclosure and is amplified by a Femto variable gain high speed current amplifier (p/n DLPCA-200). This amplified signal goes directly to the DAQ box through a shielded, twinax cable.

The light that is reflected towards the reference detector passes through another beam splitter before being reflected off of a 45° mirror and down onto the detector. This beam

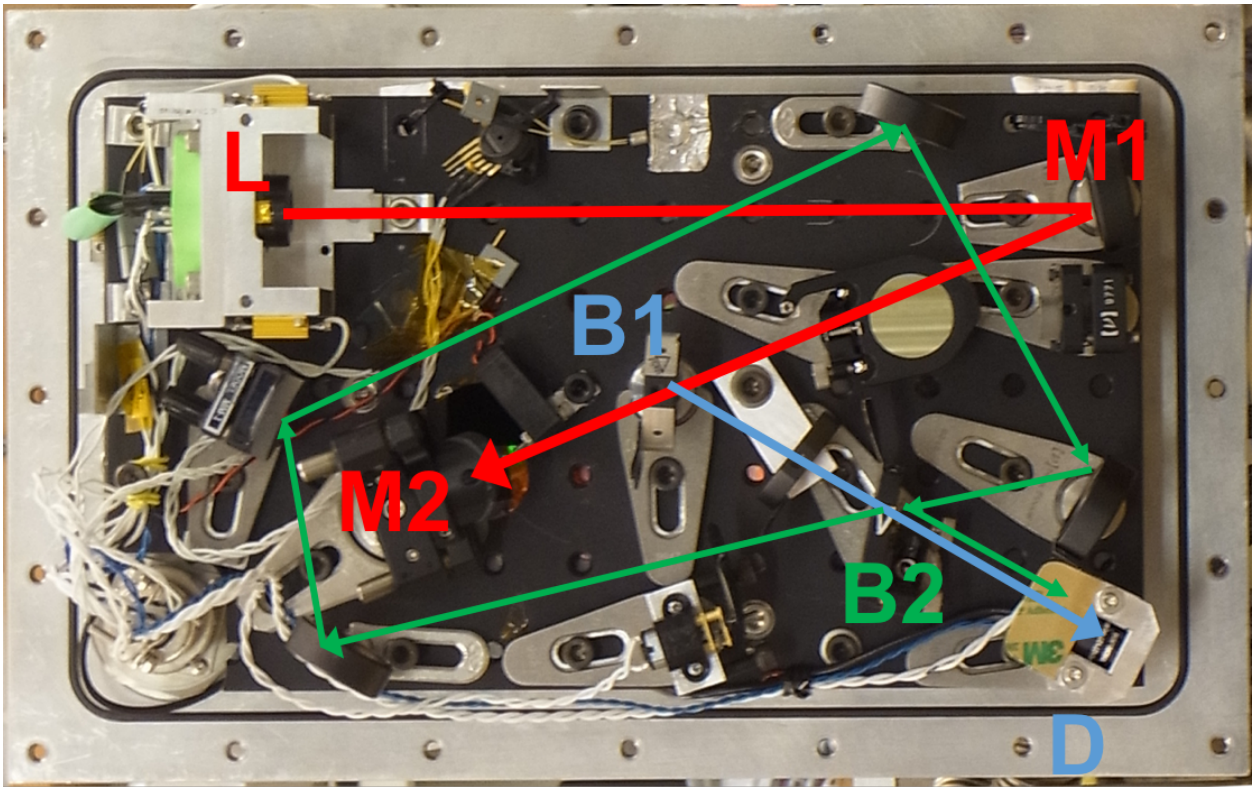

Figure 4.9: Photograph of ChiWIS laser head. Beam leaves laser (L) and reflects off of two mirrors (M1,M2) before entering the optical cavity. Some power is broken off by a beam splitter (B1) and enters a local power monitor (D). When the green optical path is unblocked by a shutter, some power reflects off the second beam splitter (B2), traverses the 4-mirror loop and falls onto the local power monitor, creating an interference fringe which can be used to generate a tuning curve for the laser.

splitter reflects light around a free space etalon with path length 57.871 cm. Upon making a full circuit around the etalon the beam passes through the beam splitter again, and some of the light is reflected onto the detector as well, resulting in the observation of an interference fringe with free spectral range (FSR) $0.0172798 = \text{cm}^{-1}$ which can be used to measure the laser's tuning curve. Light passing through the etalon can be blocked with a shutter that is controlled by the engineering computer.

The FSR and path length of the etalon were measured by flooding the optical head with a mixture of helium and N_2O, which has several regularly spaced spectral lines in the target spectra range. At STP in air these lines can be very hard to localize due to the collisional broadening they undergo, but helium has a very low cross section and when used as a carrier gas results in significantly less broadening. These measurements had to be carried out at STP since it is not safe to pump the laser head and its sensitive components down to a pressure at which collisional broadening would be suppressed. Since the line spacing is well known, once the number of etalon fringes between the line centers is know, an accurate estimate of the etalon FSR and etalon path length can be made.

N_2O is an oxidizer, so it would be safer to use a more inert gas such as CH_4, CO_2, or even water vapor should this measurement need to be repeated in the future.

The light that passes through the first wedged window strike a 45° mirror which reflects light down through a hole in the Al breadboard and into the optical cavity. The injection mirror is mounted on a two-axis stage, and adjusting the orientation of the mirror controls the injection angle of the beam into the cavity.

The cavity is aligned by reflecting a pair of co-aligned green and red laser beams into the laser head, then flipping up a mirror which reflects the beam along the IR beam's path and into the cell. The red light essentially passes through the cell unaffected, and is used for gross adjustments. Under low light conditions the green laser light can be observed on the detector side of the cavity (after the red laser has been blocked), which allows for the fine adjustments necessary to achieve a circular Herriott alignment. The adjustments are made

using the two-axis controls on the 45° mirror which reflects light into the cell.

Optical Cavity

The optical cavity is composed of two highly reflective mirrors with face centers separated by 902.02 mm. The identical mirrors have focal length 784.15 mm and are placed so that their optical axes are co-linear. The mirror substrates are 25.4 mm thick at their centers, and are made of Heraeus Infrasil 302 optical glass. This glass was chosen for its lack of OH and other impurities, which give it excellent transmission characteristics at 2.64 microns. At the target wavelength of 2.647 microns Heraeus Infrasil 302 transmits $\approx 98\%$ of light, excluding losses due to Fresnel reflection, which can be suppressed with an appropriate coating. The Plano-

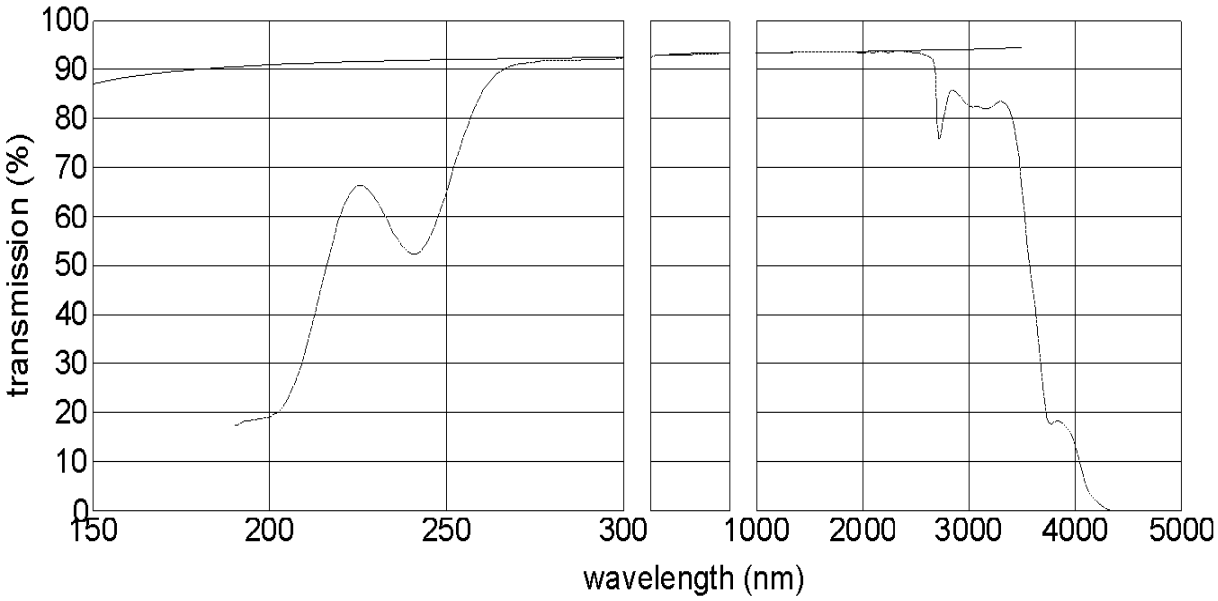

Figure 4.10: Transmission curve for Heraeus Infrasil 302 plotted as a function of wavelength. The transmission shown here is for a 10 mm thick sample and takes into account the Fresnel reflection losses at two uncoated surfaces. The top curve is the maximum transmission possible for two uncoated surfaces given the index of refraction of Infrasil. Image from Heraeus catalog.

Concave (PCV) mirror substrates were manufactured by Optimax Systems. The plano face is AR coated to $R < 0.5\%$ at 2647.7 nm, and the concave side has a max reflector coating with $R \geq 99.98\%$ and $T \approx$ 70 ppm. The coating is designed to have an overtone at $\approx$ 560 nm

which allows easy alignment of the cavity with a visible laser co-aligned with the IR beam. The theoretical mirror transmission is less than 100 ppm over the whole range from 2550 to 2750 nm.

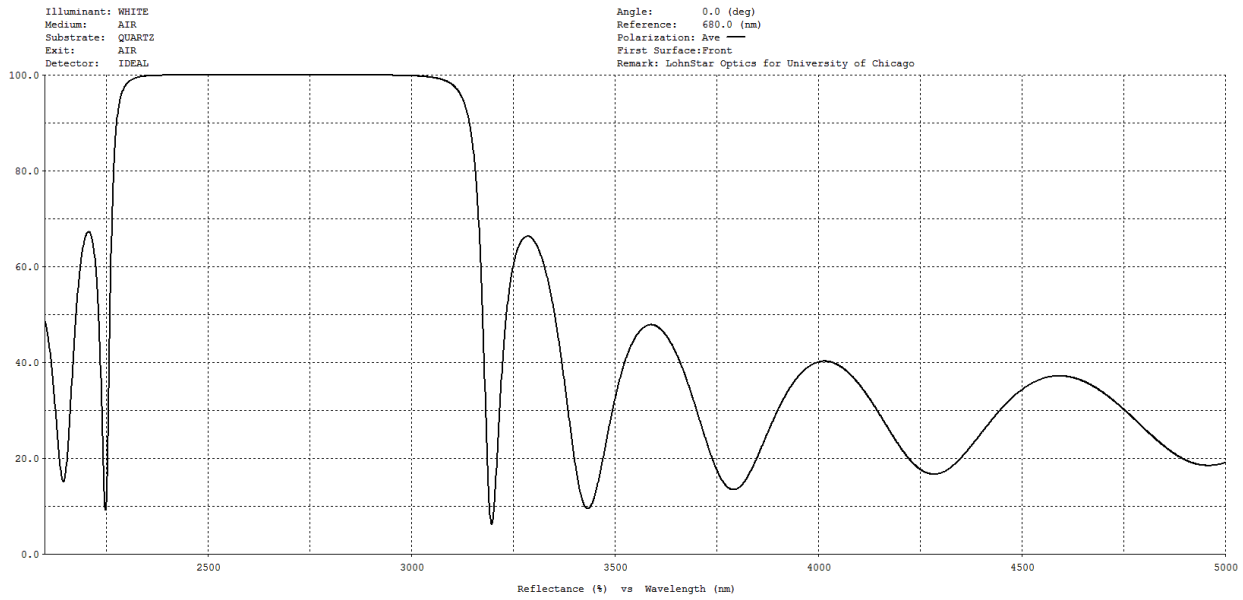

Figure 4.11: The max reflector coating on the ChiWIS mirrors is highly reflective over a range of several hundred nanometers. Image courtesy of Lohnstar optics.

The mirror geometry was carefully chosen to result in 322 spots per mirror before the reentrant condition is met, and to maximize the spatial separation between spots with short pathlength differences, as these are the primary source of broad fringes with frequency comparable to the width of target spectral features.

Detector Head

Light leaving the optical cavity passes into the detector head, then through three custom ZnSe optics before falling on the 2 mm diameter Judson detector. The three optical components are the non-axially symmetric optical component (discussed in detail in Chapter 5) and two ZnSe Plano-Convex (PCX) collection lenses. General characteristics of these components are given in Table 4.4. These components are optimized to concentrate cavity output from the cavity output mirror down onto the 2 mm Judson detector within the limited space

available. More detail about the novel nonax component can be found in Chapter 5. The detector head is sealed to maintain constant pressure during flight, and has two electrical feedthroughs and two valves through which dry air can be flushed.

Table 4.4: **Dimensions of ChiWIS optical components.** All dimensions are in mm.

Component	R_1	R_2	Diam.	CT	Material
M	-1496.3	plano	112	25.4	Infrasil 302
Nonax	NA	plano	110	7.65	ZnSe
PCX1	119.9	plano	112	16.36	ZnSe
PCX2	71.46	plano	38.1	4.586	ZnSe
Detector	plano	NA	2.0	NA	InAs

The signal detector is a InAs 2 mm diameter Judson detector (p/n J12TE3-66D-R02M) mounted on a 3-stage TEC cooler. Although better noise characteristics could be had from a smaller detector cooled to a lower temperature, raw capture of cavity output by a larger detector was more important than noise in this case. This particular detector combined a large area with a wide field-of-view, which allow output rays to make a steeper approach to the detector and thus to be focused into a smaller area.

The detector diode voltage is amplified by a Femto variable gain high speed current amplifier (p/n DHPCA-100). This device was removed from its housing to better fit into the detector environmental enclosure, and the low-voltage portions of the PCB were outfitted with copper shielding to reduce noise. The transimpedance amplifier is DC-coupled, set to 10^6 Ω gain on the low noise setting, and set to full bandwidth.

Thermo-electric Coolers

The two detectors and the laser are temperature controlled with thermoelectric coolers. The laser temperature is controlled by a Wavelength electronics temperature controller (p/n PTC2.5K-CH), which is powered from the optical bench power supply. The temperature setpoint is set via the potentiometer labeled 'TEMP SET' at the top left of the device. Adjusting this controls the base temperature of the laser diode, which consequently shifts

the observed spectral region around.

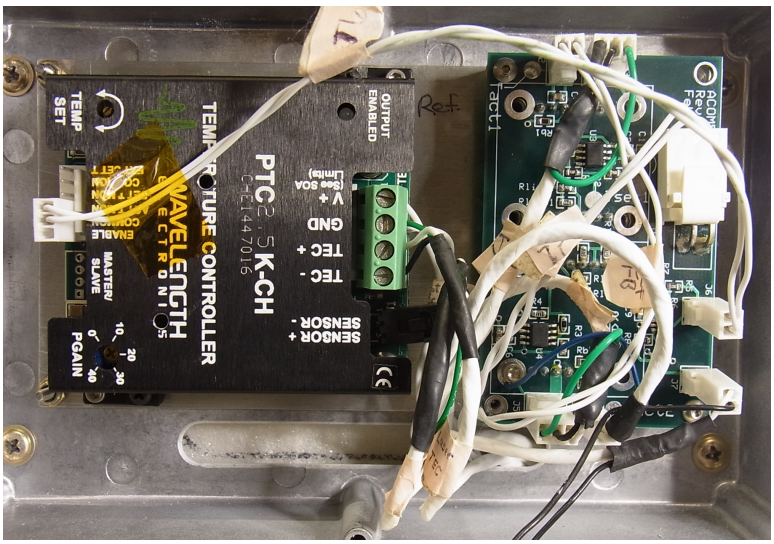

Figure 4.12: Photograph of ChiWIS Thermo-electric coolers. The device at left precisely controls the temperature of the laser diode. The temperature is controlled via the potentiometer labeled 'TEMP SET' at the top left. The board at right (ACOM536-953) has three subcircuits. Two identical circuits are anchored around Wavelength temperature controllers that cool the reference and signal detectors, and the other ensures that the laser temperature is within a certain range.

At right is the Wavelength board, which consists of three subcircuits. Two identical circuits are anchored around Wavelength temperature controllers (p/n WTC3243). These subcircuits control the temperature of the reference detector (top) and signal detector (bottom). (The controllers are not visible as they are mounted to the board from beneath and thermally anchored to a heat spreader plate.) The current limits, temperature setpoints, and PI values are all controlled by resistors soldered onto the circuit board. The third subcircuit reads a voltage from the laser TEC, and makes sure that it falls within a voltage range which corresponds to a temperature range known to be safe for the laser. This voltage range is controlled by resistors soldered to the board. The board is powered with a 5 Volt input from the optical bench power supply.

4.2.9 Gas handling

The gas handling system is composed of the heated inlet, the top valve, inlet manifolds, the optical cavity, the exhaust manifolds, the bottom valve and the pump. This section will discuss each of these subsystems.

The inlet is composed of three parts. The first is 5/8 inch stainless steel tube coated with a highly inert SilcoNert 2000 coating. The tube is welded to a BVCO fixture (also coated) on the end internal to the dome, and has no fixture on the external end. The BVCO fixtures use an L-ring to minimize dead volume in trace gas applications. The tube is integrated into the MIPAS dome cover along with inlets for the AMICA and COLD instrument which are also in Bay IX. The whole inlet assembly is supplied with its own power separate from ChiWIS. The inlet is rear-facing in order to avoid inhaling ice particles.

During operation on the Geophysica, the MIPAS inlet is connected to ChiWIS through a short length of 1/2 SynFlex tubing which has the appropriate BVCO connector on one end and a Swagelok nut and ferrule on the other. SynFlex is a flexible tubing composed of an inner layer of aluminum with an inert coating, surrounded by a black plastic cladding that protects the inner layer.

The ChiWIS-specific gas handling starts with a SilcoNert coated 90° elbow that has a 1/2 inch SwageLok fixture on one end and a KF-40 flange on the other. This part is thermally controlled (Section 4.2.10) by the Athena engineering computer.

The KF flange connects to one of two MKS Type 153D Throttle Valve Controller used in ChiWIS. These controllers consist of a type 253 butterfly valve, control electronics, and an RS-232 interface. The valve operates by rotating a metal disk with an O-ring around it within a cylinder that has KF-40 flanges at both ends. Unfortunately the valve body is not coated. The controllers operate semi-independently from the engineering computer.

The top valve regulates the pressure within the optical cavity of ChiWIS. It is directly connected to a MKS Baratron pressure gauge (p/n 722B12TCE2FA), which measures a pressure range from 0-100 Torr. When the MKS valve receives a pressure setpoint from the

engineering computer, it independently runs a PI algorithm to change the valve angle in order to match the pressure measured by the Baratron to the setpoint.

After the top valve, air enters the fore and aft manifolds, two identical coated 1/2 inch stainless steel tubes which run parallel to the optical axis of the cavity then branch and introduce air into the chamber adjacent to the cavity mirrors. The manifolds are also heated to 30°. The inlet ports are modified VBCO ports that attach to ports custom-machined into the cavity body. These ports inject air into the cavity slightly off-axis, under the assumption that this will more efficiently sweep air throughout the volume of the cavity resulting in faster overall flush times.

The cavity itself is a nominal 4" schedule 40 (4.5" OD, 4.025" ID) stainless steel steel pipe, with the interior surface hand polished to a mirror finish, then coated with SilcoNert 2000. The pipe is machined to have 4 inlet ports, 4 outlet ports, a port for the Baratron pressure gauge, and has an optical flange for mounting the mirrors and optical enclosures on either end.

Gas exits the optical cavity through 4 ports located along the centerline of the pipe. These ports again utilize custom BVCO flanges that can be rotated at increments of 45° to allow flexibility in the orientation of the tubing that handles gas that is leaving the chamber. Each flange is welded to a coated stainless steel elbow that has a 1/2 inch Swagelok flange welded to the other end. The elbows are attached to SynFlex tubing that is routed to a coated stainless steel exhaust manifold that has four SwageLok input ports and one KF-40 flange that connects to the bottom MKS valve.

The bottom valve sets the flow rate through the instrument, provided the pump can handle the commanded flow. The valve receives a command from the Athena engineering computer to open to a particular angle, then stays there until it receives another command. During flight, a flow rate is maintained until the control program is satisfied that the pump does not struggle, then the valve is opened a little more. At typical altitudes during the StratoClim campaign the bottom valve rapidly opens all the way to 90°.

Below the bottom valve gas flows through a tee and into the pump. On the right angle portion of the tee is a second Baratron pressure gauge (p/n 722BRDTCE2FA) which provides a reading of throat pressure. The pump is a modified Agilent Triscroll 300 scroll pump. In this particular unit, the original motor has been removed and replaced with a Kollmorgen (p/n AKM33H-ACDNC-00) servo motor, which has higher torque than the original and windings that are safer for high altitude use. After the scroll pump, the gas is exhausted to the atmosphere.

4.2.10 Thermal Control

Thermal control is divided into parts controlled by the engineering computer and parts that are independent of it, of which there are two. The first is environmental control for the optical bench, which runs off of the aircraft's 27 Vdc and is independent of the engineering computer. This thermal control system keeps the optical bench at roughly room temperature throughout a flight, and protects it from getting too cold in case the engineering computer fails. This system is composed of 10 independent circuits, each of which is controlled by a Minco CT325 Miniature DC temperature controller. These on/off controllers mearuser the resistance across a platinum RTD sensor and attempt to match that to a user specified setpoint. When the measured temperature is below the setpoint, the controller switches to put the full 27 Volts across the strip heaters mounted on aluminum panels on the interior portion of the optical bench base and the optical bench cover. The resulting current must flow through a thermal cutout (TCO) which fails at 70° C to prevent runaway heating in case of controller failure.

The second independent part is the pair of fans that are screwed onto the lid of the DAQ environmental enclosure. These are wired to 24 Volts from one of the Vicor boards through a normally open thermal switch. When this switch (which is located under the fin shroud located on the the lid) goes above 50° C, it closes which activates the fans. This is done to protect the two computers in the DAQ enclosure from getting too hot.

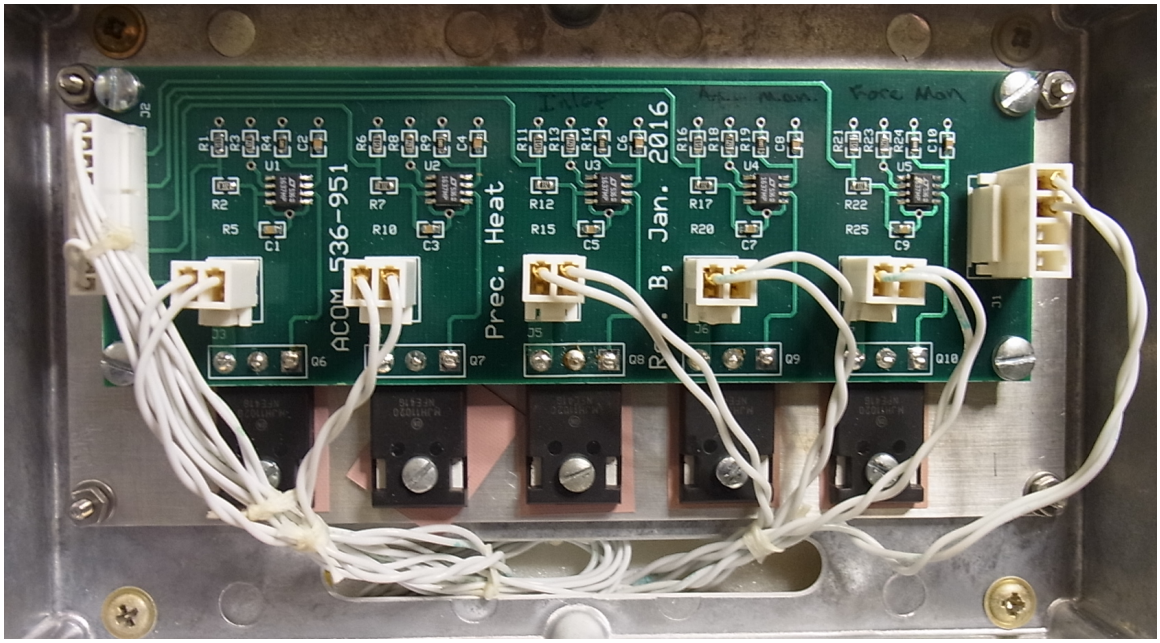

Figure 4.13: Precision heater boards which receive a setpoint command from the Athena engineering computer which controls the current output through the heater in question. Each board has 5 subcircuits, for ten subcircuits total. During StratoClim only the subcircuits controlling the ChiWIS inlet heater and the manifold heaters were used.

The second thermal control system is controlled by the engineering computer. It outputs analog voltages to two precision heater boards (ACOM536-951), which then source current to the heater in question. Each heater circuit is safety protected with a TCO to prevent runaway heating in case of a computer failure. In Figure 4.13 board is powered with +24 Vdc through the big molex connector at the right, and the analog inputs enter the board through the 10-pin connector at the left of the board. Each board has five identical subcircuits which condition the analog input to the appropriate voltage range, and a Darlington transistor which outputs current to the heater it is connected to. The transistors are heat sunk to a heat spreader plate, which is thermally anchored to the instrument's structural rail through the Bud box it is housed in. A thermistor is mounted on each component to be heated, and the engineering computer tries to match the temperature derived from the thermistor to the setpoint temperature through a software PI algorithm coded in LabView.

During the StratoClim campaign only three subcircuits were used, and they controlled

the ChiWIS inlet and the two manifold tubes. The wiring is in place to control the optical breadboard, the laser mount, the laser enclosure, the detector enclosure, and the fore, middle, and aft portions of the optical cell, although in practice the Minco controllers do a good enough job.

4.2.11 Safety

In ChiWIS any circuit that could potentially short and draw a dangerous mount of current is fused, and any element that could overheat has a safety cutout which cuts power to the element if it gets too hot. Wherever possible there is also software feedback that reduces the power through an element if it gets too warm, and eventually shuts it off before it gets dangerously hot. Here several of the most important safety systems will be described.

The thermal behavior of the pump at high altitudes was of great concern due to the relative lack of convection at high altitudes where pressure is 100 mb or less. The first line of defense against the pump overheating is implemented in software. An AD590 temperature gauge is mounted to the pump head, and if it reports a temperature beyond a user defined value set in the ACWIS control program, it decreases the pump's rotation rate. If the pump head's temperature increases further beyond a second temperature, the pump is completely stopped. There is also a second, hardware safety which is wired through the Sensitron motor controller. This device has an E-Stop pin, and the board will operate as long as this pin is pulled low (its exact behavior is configurable through the software that accompanies the device). The pin is wired to ground through a TCO which is embedded in the pump head. If this TCO gets too hot, it breaks and results in an open circuit, and the E-Stop pin floats high, which turns off the controller.

4.3 Ramp characteristics

The characteristics of the laser ramp have a large on measurement quality, and careful choice is necessary. The tuning range and tuning rate both depend on the laser heat sink temperature, initial and final laser current, time of the ramp, and time between ramps, so achieving the right range and rate is often an iterative process.

4.3.1 Tuning Range

The tuning range used in StratoClim was chosen to include the target HDO line at 3776.9 cm^{-1} and two water lines: the 'big' H_2O line at 3777.9492 cm^{-1} and the 'medium' H_2O line at 3776.444 cm^{-1}. These big water line is approximately 100 times more intense than the medium line, and provides extremely precise measurements at even the driest levels of the atmosphere, but is nearly saturated above about 50 ppm. The medium line is more comparable in strength to the HDO line, and provides useful measurements up to hundreds of ppm. This spectral region spans about 1.5 wavenumbers, although the lasers themselves are capable of much broader ramps. The typical laser TEC voltage setpoint during StratoClim was 2.177 Volts.

4.3.2 Tuning Rate

Once the desired tuning range is known, the tuning rate is chosen as a tradeoff between suppressing optical noise and increasing noise in the retrieved concentrations by smearing the lines out and making the estimate baselines more uncertain (see Section 2.2.3 and Figure 2.10). In StratoClim, the ramp rate was chosen to be about 192 cm^{-1} s^{-1}, which results in a ramp repetition rate of about 62 ramps per second.

The settings shown in Table 4.5 correspond to a ramp that starts at 324.3 mA and ends at 505.3 mA, with a ramp length of about 12.1 ms and a gap time of about 3.8 ms. During the campaign the I-final value was sometimes varied in the least significant 3 bits to better

Table 4.5: **Typical Ramp Generator Dip Switch Settings in StratoClim.** These quantities correspond to t_g, t_r, I_H, and I_L respectively in Figure 4.7.

T-end	T-pulse	I-final	I-initial
0	0	1	1
0	0	1	0
0	1	1	0
0	1	0	1
1	0	0	0
1	0	1	1
1	0	1	0
1	0	1	0
0	0	0	0
0	0	0	1

place the big water line and adjust the position of a mode hop.

4.4 Fitting data to extract concentrations

Before concentrations can be extracted from the data, several steps must happen. First, the data must be reduced to a manageable size for the fitting routine to handle. Then a mirror loss value must be extracted from the cavity ringdown time. This piece is essential for the fitting routine to estimate the average number of passes light makes through the cavity. Lastly, a tuning curve must be generated from the reference data so that the area of the spectral features can be properly integrated.

4.4.1 Data Reduction

The PXIe computer (Section 4.2.6) recorded each ramp in the StratoClim campaign as a series of fifty thousand 16-bit integers at a rate of ≈ 62 hertz. The ramps are recorded 1400 per file in two channels. The first channel is from the signal detector and the second is from the reference detector. The spectral features are heavily oversampled to achieve better noise characteristics through rebinning. StratoClim data are rebinned to one second and 5000 samples per ramp.

4.4.2 Tuning curves

The tuning curve is the laser's wavelength as a function of time, or more commonly, sample number. This curve is derived from the reference detector signal. Periodically during Strato-Clim, a small fraction of laser light is allowed to traverse a free space etalon within the laser head, which results in the observation of an interference pattern on the reference detector. This 'fringing' pattern, or etalon, can be extracted from the reference signal by dividing a reference signal with fringing by a signal just before or after the onset of fringing.

The FSR of the etalon is known (see Section 4.2.8), so counting the number of fringes from a specified sample, then multiplying that by the FSR of the etalon gives the relative difference in wavenumbers between two samples in the ramp. Once discrete data for relative wavenumber as a function of sample number have been generated, that can be fit to the following functional form, which is accepted by ICOSfit:

$$x' = \frac{x - E\,[0]}{1000} \tag{4.1}$$

$$\nu = FSR\left(E\,[1] + E\,[2]\,x' + E\,[3]\,x'^2 + E\,[4]\,e^{x'/E[5]} + E\,[6]\,e^{x'/E[7]}\right). \tag{4.2}$$

Here x is the raw sample number, and E is the set of parameters to be fit to the data. Once E satisfactorily represents the observed fringe, it can be fed into ICOSfit. Note that this tuning curve only gives the relative wavenumber. The fit routine retains the degree of freedom that allows the tuning curve to shift in order to match the lines it is required to fit.

4.4.3 Cavity ringdown times

Each ramp has a very abrupt turnoff, with a time from maximum current to minimum current less than one microsecond. Due to the long residence time of power in the cavity, the signal detector sees this sharp edge as an exponential decay, from which the cavity ringdown time can be estimated. The cavity ringdown time is related to the reflectivity of the cavity

mirrors through Equation 2.27, and once R is know the per pass mirror loss can be input into the fit routine.

For signal ramps, data acquisition ends before the ramp is cut off. During StratoClim every 200th file (starting with zero) was composed solely of ringdowns.

4.4.4 ICOSfit

ICOSfit [Sayres et al., 2009] is a multi-variable, non-linear, least-squares fitting algorithm written in C++ by Norton Allen in the Anderson Group at Harvard University. This fitting routine is optimized for absorption spectra from Herriott and ICOS instruments, although it can be easily used for White cell and open-path measurements as well.

CHAPTER 5

IMPROVED LIGHT COLLECTION IN ICOS CELLS USING NON-AXIALLY SYMMETRIC OPTICS

High effective path lengths and stable optical configuration make Integrated Cavity Output Spectroscopy (ICOS) a useful spectroscopic technique for measuring trace gases. However, the skewed nature of the output ray geometry of ICOS cavities makes it difficult to collect the already weak cavity output onto small detectors. We derive the constraining effect of skewness in ICOS cavities with Herriott alignments, which limits light collection efficiency for compact instrument designs, and show how this constraint can be overcome by addition of a non-axially-symmetric optical component. We demonstrate the efficacy of this approach with the ICOS-based Chicago Water Isotope Spectrometer (ChiWIS), which incorporates a skew-correcting optical element consisting of eight ZnSe wedges, and show that it increases collection efficiency by approximately a factor of six.

5.1 Introduction

ICOS is an absorption spectroscopy technique in which light is injected off-axis into a resonant cavity consisting of high-reflectivity mirrors to provide a very long optical path length [O'Keefe, 1998, Engeln et al., 1998]. For example, a 1 m cavity with mirror reflectivity of 99.98% will have an effective pathlength of 5 km. ICOS instruments are routinely used to measure trace atmospheric constituents with concentrations as low as parts per trillion [Hodgkinson and Tatam, 2013], and their relative insensitivity to alignment and environmental vibration make them an attractive choice for measurements in the field. Compact instruments with low cavity volumes and short flush times can yield sampling rates of ≈ 10 hertz [Sayres et al., 2017]. However, since laser light must pass through the cell mirrors to enter the cavity, it is attenuated by a factor of (1-R), making this an inherently low power technique and placing a premium on efficient light collection of the cavity output.

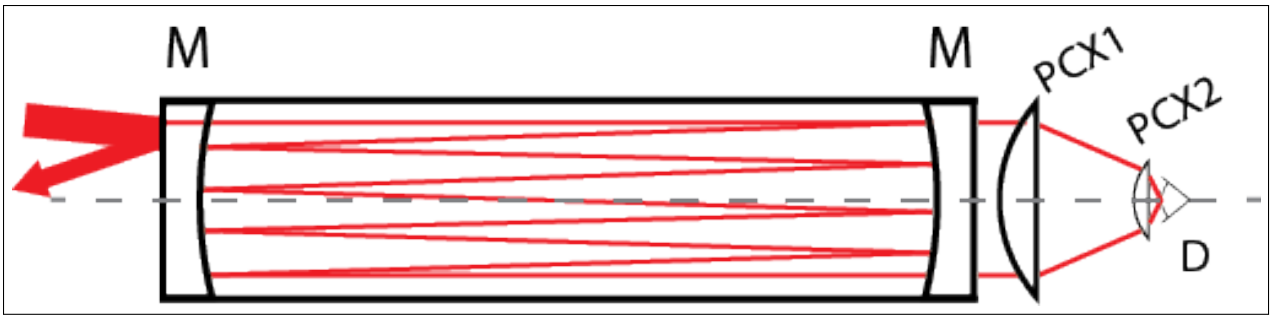

Figure 5.1: Two identical cell mirrors are labelled M, the plano-convex collection lenses are PCX1 and PCX2, and the detector is labelled D. Most power is reflected away before it enters the cavity, making ICOS a low power technique. All optics are axially symmetric and share the same optical axis, represented by the gray dashed line.

ICOS cells are typically aligned with a circular Herriott pattern [Herriott et al., 1964], in which beam paths are innately divergent and skewed. For an axially symmetrical optical system with off-axis alignment, the divergence of the beam is its component co-planar with the optical axis, and the skewness is the component that is not co-planar with the optical axis (Figure 5.2). Divergence is easily handled by standard optical components, but skewness cannot be completely removed by axially symmetric lenses. While skewness may be an advantage for Herriott cells, allowing for greater separation between cavity input and output beams and their associated optics, it is a detriment in ICOS cells, in which light does not exit the cell through a single aperture, but through all points on the Herriott pattern. For ICOS, skewness places strict lower limits on how focused cavity output can be and therefore hinders light collection. Due to the limited sizes of commercially available detectors, this constraint can limit output collection efficiency for ICOS instruments.

In direct analogy to angular momentum and central forces, skewness is conserved by axially symmetric optics, and the skew invariant

$$h = nS \sin \gamma \tag{5.1}$$

remains unchanged under any interactions with axially symmetric components [Winston et al., 2005]. Here n is the index of refraction of the medium, S is the minimum distance

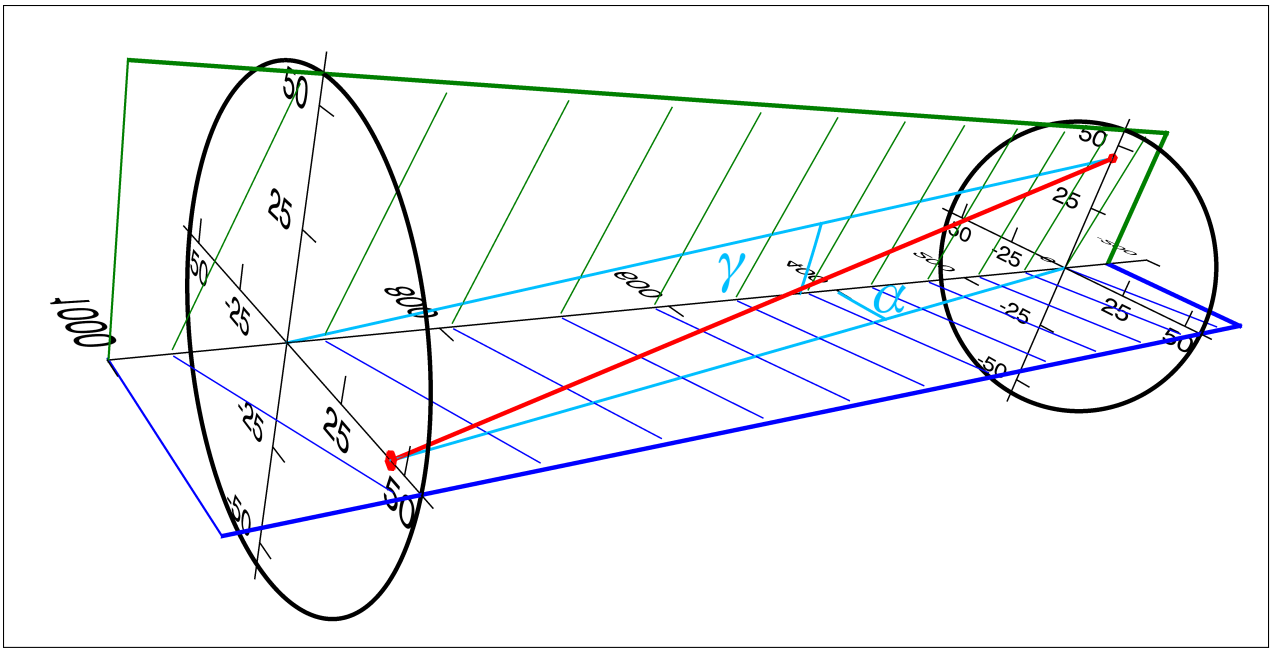

Figure 5.2: The thick red line is a ray propagating from one mirror to another, and the blue red lines are its projections into the tangential (blue) and sagittal (green) planes. The divergence angle α is the angle between the optical axis the ray's projection into the tangential plane, and the skew angle γ is the angle between the optical axis and the ray's projection into the sagittal plane.

between the skew ray and the optical axis, and γ is the skew angle between the ray and the optical axis. Interaction with axially symmetric components can only trade between S and $\sin\gamma$, and we see that h/n is the theoretical minimum approach a skew ray can make to the optical axis.

In ICOS instruments the cavity mirrors and collection optics typically share the same optical axis (see Figure 5.1), so the Herriott reentrant conditions of the cavity define a skew invariant for the whole system. The skew and divergence angles are identical for every output ray in the circular Herriott spot pattern, so for this geometry the skew invariant h defines the minimum radius to which the mirror spot pattern can be focused by axially symmetric optics.

In an optical cavity aligned in a reentrant Herriott pattern, the skew angle is fully determined by two dimensionless cavity geometry parameters. The Herriott pattern is set by $u \equiv f/d$, the ratio of mirror focal length to mirror separation, and the cavity aspect ratio

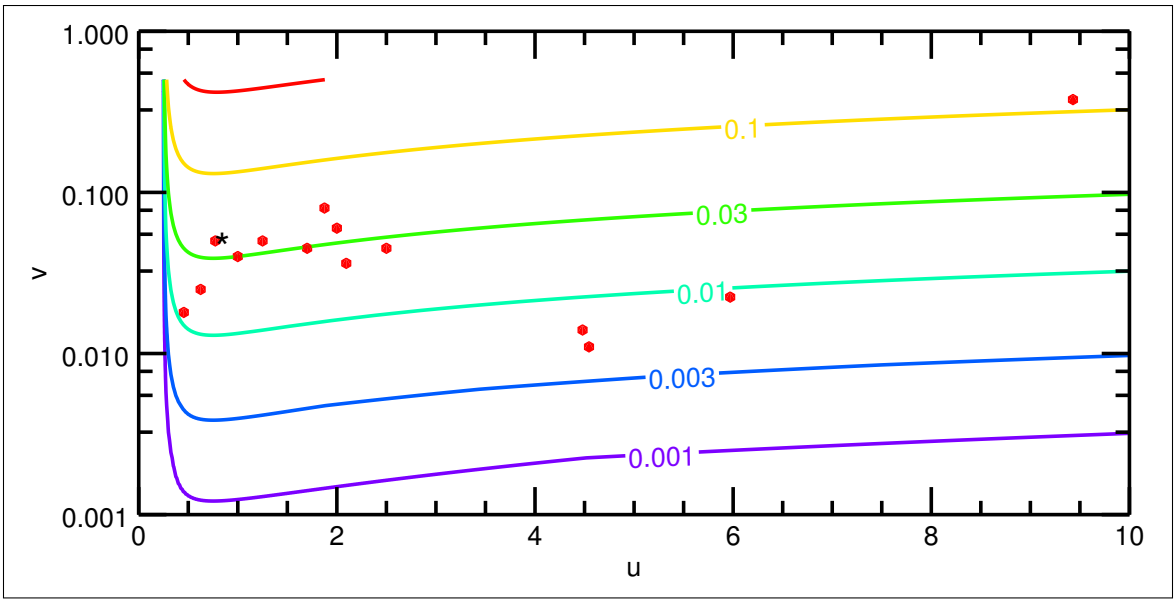

Figure 5.3: Contour plot showing h/A plotted against the dimensionless cavity geometry numbers $u = f/d$ and $v = A/d$. Here h is the skew invariant, f is the focal length of the mirrors, and d is their separation. Larger values of the skew angle γ result in larger skew invariants for a given Herriott pattern radius A. The A/d ratio is a much stronger control on skewness than changes in u. ChiWIS is marked with a black asterisk. Note that Herriott cell solutions exist only for $u > 0.25$ (i.e. $d/f < 4$).

is described by $v \equiv A/d$, the ratio of Herriott pattern radius to mirror separation. We can therefore rewrite Equation 5.1 in terms of these cavity geometry numbers.

Writing the reentrant condition's beam injection direction unit vector $\hat{x}$ in cylindrical coordinates (cf. Equations 2.21 and 2.22) makes the skew and divergence (α) angles of the Herriott pattern identifiable:

$$\hat{x} = \frac{1}{\sqrt{1 + \frac{v^2}{u}}} \left(-\frac{v}{2u} \ , \ \pm\frac{v}{2u}\sqrt{4u - 1} \ , \ 1 \right) \tag{5.2}$$

From equation 5.2 we see that the divergence angle is $\alpha = \arctan\left(-v/2u\right)$, and that the skew angle is:

$$\gamma = \arctan\left(\pm\frac{v}{2u}\sqrt{4u - 1} \right) \tag{5.3}$$

The $\pm$ sign here corresponds to cells with clockwise and counter-clockwise alignments, respectively, as viewed from the input side of the cell. A ray's closest approach to the optical

axis in the cavity occurs halfway between the mirrors at the beam pattern waist, and that distance is given by $S = A\sqrt{1 - 1/4u}$. ICOS cavities are typically filled with low pressure air, so we take $n = 1$. From these and Equation 5.3 we see that the cavity skew invariant is given by:

$$h = S \sin\gamma = A \left(\frac{v\sqrt{1 - \frac{1}{4u}}}{\sqrt{v^2 + \frac{4u^2}{4u-1}}} \right) \tag{5.4}$$

The cavity geometry parameters therefore provide insight into how relevant skew may be for instrument design. Figure 5.3 shows the contours of h/A as a function of u and v, along with the values from selected ICOS instruments described in the literature. (Details for those instruments are also shown in Table 5.1.) The parameter h/A can be thought of as a concentration factor describing how strongly a circular Herriott pattern can be focused onto a detector. Two features are readily evident from Figure 5.3. First, the cavity aspect ratio $v = A/d$ is a much stronger control on the concentration factor than is u. Second, most ICOS instruments cluster within a relatively small range of parameter space, producing very similar concentration factors ($h/A \approx 0.03$). In this design regime, concerns about collection efficiency will scale with A and so with instrument size.

Instruments with large A and therefore large skew invariants, such as this work and Sayres et al. [2009], typically have designs motivated by reducing potential optical 'noise'. Larger-diameter spot patterns minimize overlap of beam spots within the coherence length of the laser, reducing unwanted resonance effects. These constraints are generally strongest for the longer wavelength instruments, whose diffraction-limited spot sizes are larger than those for instruments operating in the near-IR. A second class of instruments susceptible to large skew angles are those required to be extremely compact and low-volume. In these cases d is made very small, while A is constrained by optical resonance considerations, and A/d can become very large. The instrument with the highest skew invariant in Table 1 Bakhirkin et al. [2004], a breath analyzer only 5.3 cm in cavity length, falls into this category. As the

Table 5.1: **Geometry and Skewness of Selected ICOS Instruments.** Values of A with an asterisk are estimated from other quantities in the given reference. Instruments are listed in order of decreasing h.

Instrument	u	v	A (mm)	γ	h (mm)
Bakhirkin et al. [2004]	9.4	0.38	20*	6.9°	2.4
Sayres et al. [2009]	0.77	0.05	45*	2.66°	1.7
This Work	0.83	0.05	45	2.62°	1.7
Sayres et al. [2017]	1.88	0.08	20*	3.4°	1.1
Provencal et al. [2005]	1.25	0.05	20*	2.3°	0.70
McCurdy et al. [2006]	1.0	0.04	20*	2.0°	0.59
Zhao et al. [2007]	1.7	0.045	20*	1.84°	0.59
Marchenko et al. [2015]	2.0	0.06	15*	2.4°	0.55
Baer et al. [2002]	0.65	0.025	20*	1.4°	0.38
Jia et al. [2009]	2.1	0.036	13*	1.4°	0.29
Engel et al. [2006]	0.46	0.018	20*	1.04°	0.24
Sonnenfroh and Parameswaran [2011]	2.5	0.045	9*	1.6°	0.23
Tan and Long [2010]	6.0	0.022	15*	0.59°	0.15
Paul et al. [2001]	4.5	0.014	9.5	0.37°	0.062
Kasyutich et al. [2003]	4.5	0.011	2.5*	0.30°	0.013

ICOS technique is more widely adopted in lightweight and portable instruments, skewness may become an increasingly important design consideration.

If design constraints mandate a skew invariant so large that light collection is limited, better focus can be achieved by using optical components that are not axially symmetric. Such components break the symmetry of the output and do not require skewness to be conserved, and can gainfully exploit the symmetry of the Herriott pattern. Here we describe a simple non-axially symmetric optical component designed for the Chicago Water Isotope Spectrometer (ChiWIS) that allows skewed output rays to be imaged onto the optical axis and results in an approximately six-fold improvement in light collection.

5.2 Design

To correct the skewness inherent in the ChiWIS Herriott pattern, we designed an optical component composed of eight, identical wedged windows, which are manufactured in the shape of 'pizza slices', then glued together and assembled into a mount. This component is

placed between the cavity output mirror and the big plano-convex (PCX) collection lens as shown in Figure 5.4. The slope of the wedged surface is such that it corrects most of the cavity output skewness allowing the output to be focused into a much smaller area.

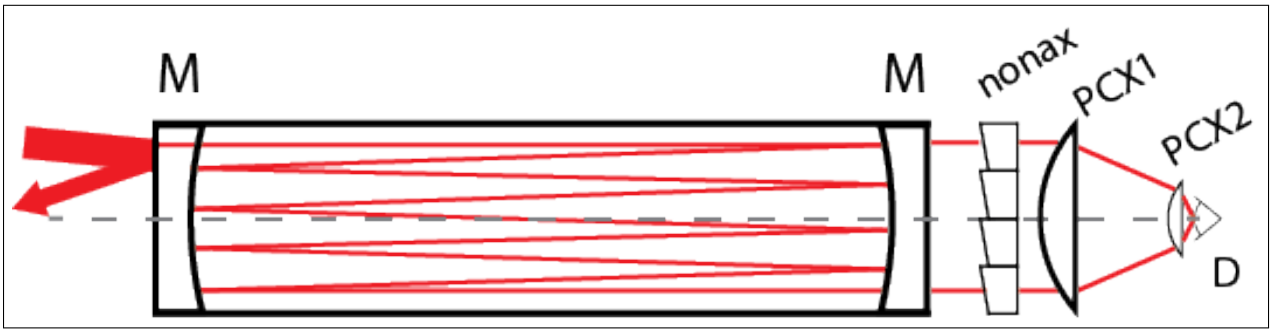

Figure 5.4: Schematic of ChiWIS cell and detection optics with nonax component included. It is placed between the cavity output mirror and PCX1 where the output rays are nearly paraxial, and refracts out most of the skewness in those rays before they are focused down to the optical axis.

The ChiWIS geometry results in a skew invariant of ≈ 1.7 mm, mainly due to its large spot pattern, which was necessitated by its relatively long target wavelength of ≈ 2.647 microns. This wavelength was chosen to measure H_2O and HDO spectral features, and also interacts strongly with OH impurities in glass, requiring the use of high-purity optical materials like Infrasil and ZnSe. The cavity mirrors were 902.02 mm apart, and the collection optics consist of the non-axially symmetric component (nonax), two ZnSe PCX lenses, and a 2 mm diameter InAs Judson detector (J12TE3-66D-R02M). The detector chip is packaged in a can with field-of-view of about 65°, which limits the angle of incidence (AOI) of light onto the detector. Limited AOI onto the detector chip means that in practical terms the minimum spot size h shown in Table 5.1 cannot be achieved. Information about the optical components used in ChiWIS is shown in Table 4.4.

Axially symmetric collection optics can gather only a small portion of the light exiting the cavity. Ray tracing calcultions suggest that Herriott alignment results in collection efficiency of only 13% (Figure 5.6, top). The output retains the ring shape of the original Herriott pattern, with minimum focusing diameter of 4.6 mm, much larger than our detector.

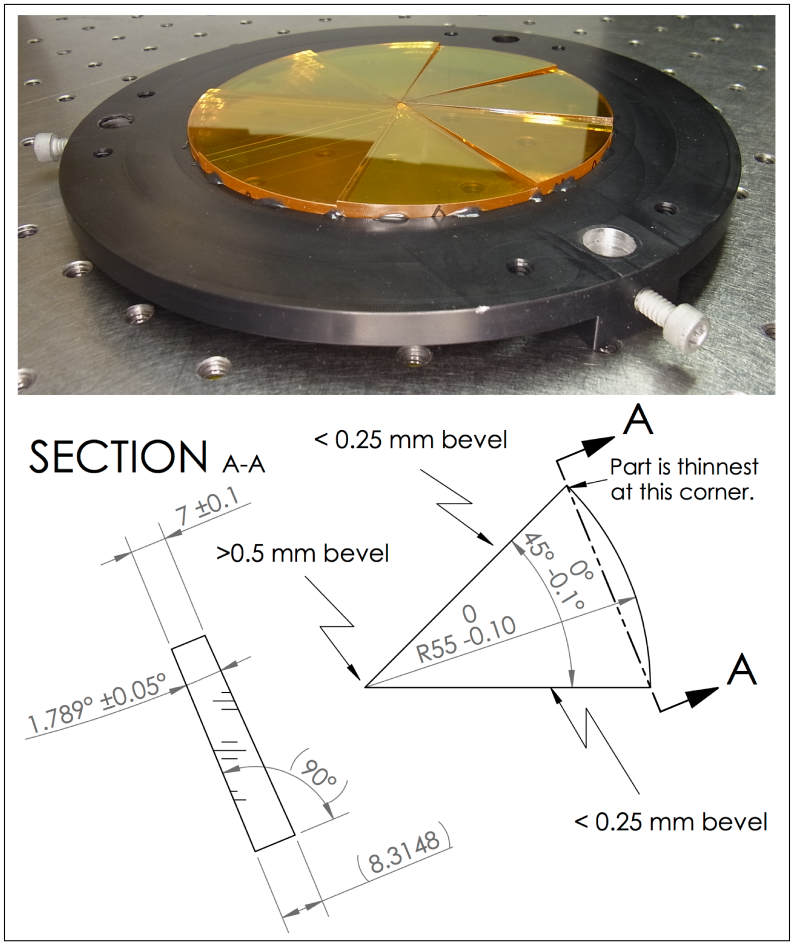

Figure 5.5: *Top:* Photograph of the assembled nonax optic mounted in its anodized, Al mounting ring. The component is photographed at a shallow angle to show the steps between individual slices. *Bottom:* Mechanical drawing of the wedged slices. The gradient of the wedged surface should point from one corner to the other along cross section A-A, but a manufacturing error resulted in the gradient pointing from one corner to the opposing edge. This error does not significantly affect the function of the slices. All dimensions in mm.

Collection efficiency could be slightly increased by aligning the detector face perpendicular to the incoming cavity output, but that adjustment would still result in at best 20% capture. Introducing our designed asymmetric optical element should improve light collection to 93% (Figure 5.6, middle).

While the mathematically perfect un-skewing optic would be a helix, which is prohibitive to manufacture, a design consisting of multiple wedged windows cut into the shape of circular sectors (slices) can closely approximate the ideal element. Once the cavity's skew angle is known, we can determine the local surface necessary to completely refract out the skewness. Assuming the component has its wedged surface facing the cavity output mirror, and that the second surface is plano, perpendicular to the optical axis, and that no refraction in the azimuthal direction occurs there, the wedge angle β necessary to refract out the skew is:

$$\tan\beta = \frac{n_0 \sin\gamma}{n_1 - n_0 \cos\gamma} \tag{5.5}$$

Here n_1 is the index of refraction of the wedge material and n_0 is the index of refraction of the medium. For ZnSe at 2.64 microns $n_1 = 2.4398$ J. Connolly [1979], and $\beta_{ChiWIS} = 1.79°$. The wedge angle points the surface normal away from the incoming skew rays, increasing the angle of incidence on the wedged surface. This also implies that a set of wedges has 'handedness', and cannot be used with both clockwise and counter-clockwise cavity output. Materials with high indices of refraction have lower wedge angles and require less material for manufacture.

The slices are designed to perfectly correct the cavity output along their centerline, and leave only 0.17 degrees of residual skew angle along their edges. When assembled, the net result of the nonax component is that each slice directs the section of the cavity output that passes through it onto the optical axis. (Here we refer to the points where the arc and the radii of the slices meet as the 'corners', and the point where the two radii meet as the vertex.) Each slice is wedged with the angle β calculated above such that the gradient of

the wedged surface points from one corner to the other along cross section A-A (Figure 5.5, bottom). The thickness of the slice at the vertex and along the centerline of the slice is half way between the minimum and maximum thicknesses.

We chose eight slices as a compromise between increased skew cancellation and increased light interaction with component edges and difficulty of assembly. Optical components with two or 4 wedged slices still allow a significant fraction of the light to miss our 2 mm detector (27% and 53%, respectively). Increasing the number of slices beyond 8 results in little improvement due to finite beam size and deviations from a perfectly circular Herriott cell pattern. The drawback to increasing the slice number is more interface surfaces between them, which are likely to scatter light or refract it away from the detector. Assuming a 2 mm diameter beam size, and a Herriott spot pattern 45 mm in radius, $\approx 5\%$ of the rays should overlap the surface between two wedges in the eight-fold case.

The actual manufactured slices have an error in their wedge gradient which ray tracing calculations suggest reduces capture efficiency to 91% (Figure 5.6, bottom). Instead of pointing from corner to corner, the gradient points from corner to edge, leaving at most 0.8° of skew angle, corresponding to a maximum skew invariant of 0.63 mm. These components tend to introduce more divergence with a greater spread than the design version, and as a result, the spot pattern in the detector plane appears more diffuse than in the ideal case.

The 8 identical wedged slices were manufactured by Rocky Mountain Instrument Company from polycrystalline ZnSe, and were AR coated to less than 0.2% reflectivity by Lohn-Star Optics. All edges are beveled to prevent chipping, but the bevel at the vertex of each slice is made larger to allow for some play in their assembly if they vary slightly. After manufacture and coating, the slices are assembled stepwise into the full optical component. The individual slices are bonded together with Norland Optical Adhesive 83H by applying a small amount of adhesive to the faces to be attached, then curing for 60 minutes at 80° C. Good contact between the faces is ensured by mounting the wedges in a circular aluminum form out of which a circular sector matching the parts to be bonded has been removed.

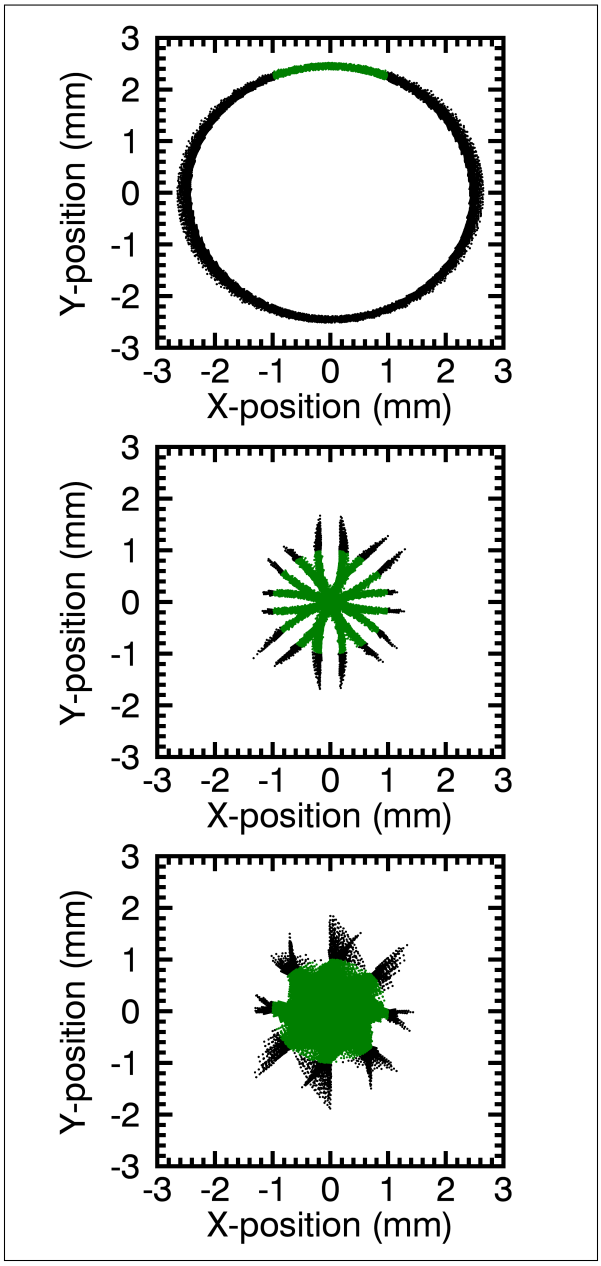

Figure 5.6: Calculated spot patterns in the detector plane without the nonax component (*top*), with the designed nonax component (*middle*), and the actual mis-manufactured nonax component (*bottom*). Green spots are those that intersect the 2 mm diameter detector. The collection efficiencies in each case are 13%, 93%, and 91%. These ray tracing calculations are done by approximating the laser beam by a bundle of 121 parallel rays with a diameter of 2 mm, then injecting them into the cavity in a Herriott configuration. The bundle is advanced over one complete cycle of the cell's Herriott pattern (622 passes), and at each point of intersection with the output mirror the rays are refracted through it and enter the collection optics.

The slices are pressed into place using a large band clamp that goes all the way around the aluminum form and slices. A strip of rubber is placed between the band clamp and the slices to protect them.

Once the full disk of slices is assembled, it is placed into a custom mounting ring compatible with the 3-rail system on the detector side of ChiWIS. The bottom panel of Figure 5.5 shows the final assembly. To hold the component in place, several dots of 3M DP 420 epoxy are placed around the edge of each slice. The component/mounting ring assembly is placed between the cavity mirror and the large PCX lens, as close as possible to the mirror.

5.3 Results

By mapping the focused cavity output in the detector plane, we demonstrate that the non-axially-symmetric optical element performs as expected to increase the efficiency of light collection (Figure 5.7). Output is peaked and centered on the optical axis, with a radius similar to that predicted by ray tracing calculations (Figure 5.6, bottom panel). In the absence of the nonax component, we would expect to see an intensity map that was the convolution between the circular detector shape and the top panel of Figure 5.6 – a smeared-out ring with a distinct intensity minimum at the center of the pattern.

The output is mapped in 200 micron increments over a 5.8 by 5.2 mm range by mounting an XYZ translation stage (Newport 460-XYZ) to the 3-rail mounting assembly on the instrument's detector side, and attaching a 2 mm Judson detector to the translation stage. Although the detector is comparable in size to the features we wish to map, it can easily distinguish the most important effects attributable to the nonax component. Each point in Figure 5.7 represents the total power collected by the detector when centered at that point – in other words, the intensity map is a convolution of the detector's shape and the true cavity output pattern. The data were taken in alternating positive/negative x-direction stripes, and the y-position was incremented between each stripe. Play in the translation stage's vernier dial introduced a discrepancy in the measured x-position between positive

and negative stripes, which was corrected after the data were taken.

The observed output with the nonax component is nearly Gaussian with a FWHM of ≈ 2.36 mm, confirming that it is effectively removing skew and allowing for maximum capture by the 2 mm detector. Deconvoluting the detector shape from the intensity map indicates that the true FWHM of the output is ≈ 1.8 mm, implying the detector captures about 75% of cavity output. Output radius is somewhat larger than the value of ≈ 1.2 mm derived from ray tracing calculations, and efficiency smaller, probably due to a slightly elliptical Herriott cell pattern, which tends to smear the output for the same reasons as the finite beam size. Ray tracing simulations of an elliptical Herriott cell pattern with semiminor axis of 43.5 mm and semimajor axis of 46.5 mm yields a significantly more diffuse spot pattern at the detector plane in which only 70% of the cavity output is captured. The deconvolution procedure assumes that the detector face is a perfect circle of diameter 2 mm and that its response is uniform. The detector chip is cooled to ≈ -65° C, and should have nearly uniform response across its face at this temperature.

We see no other optical or mechanical effects that would limit performance. This component introduces no fringing into observed spectra, and optical noise in the system as a whole is much lower than electrical noise. The assembly process described here results in strong bonds between the wedges themselves and between the wedges and their mount. This optical component was field-tested during the StratoClim Asian Monsoon field campaign, where it was used in eight flights aboard the M55 Geophysica, a high-altitude research aircraft, and required no repair or modification after these flights.

5.4 Discussion

We describe here the design and assembly of a simple, non-axially symmetric optical component that can be used to increase the collection efficiency of large ICOS instruments by a factor of six. This optical component removes enough of the native skewness of cavities aligned in a Herriott pattern that most of the cavity output can be focused down onto a

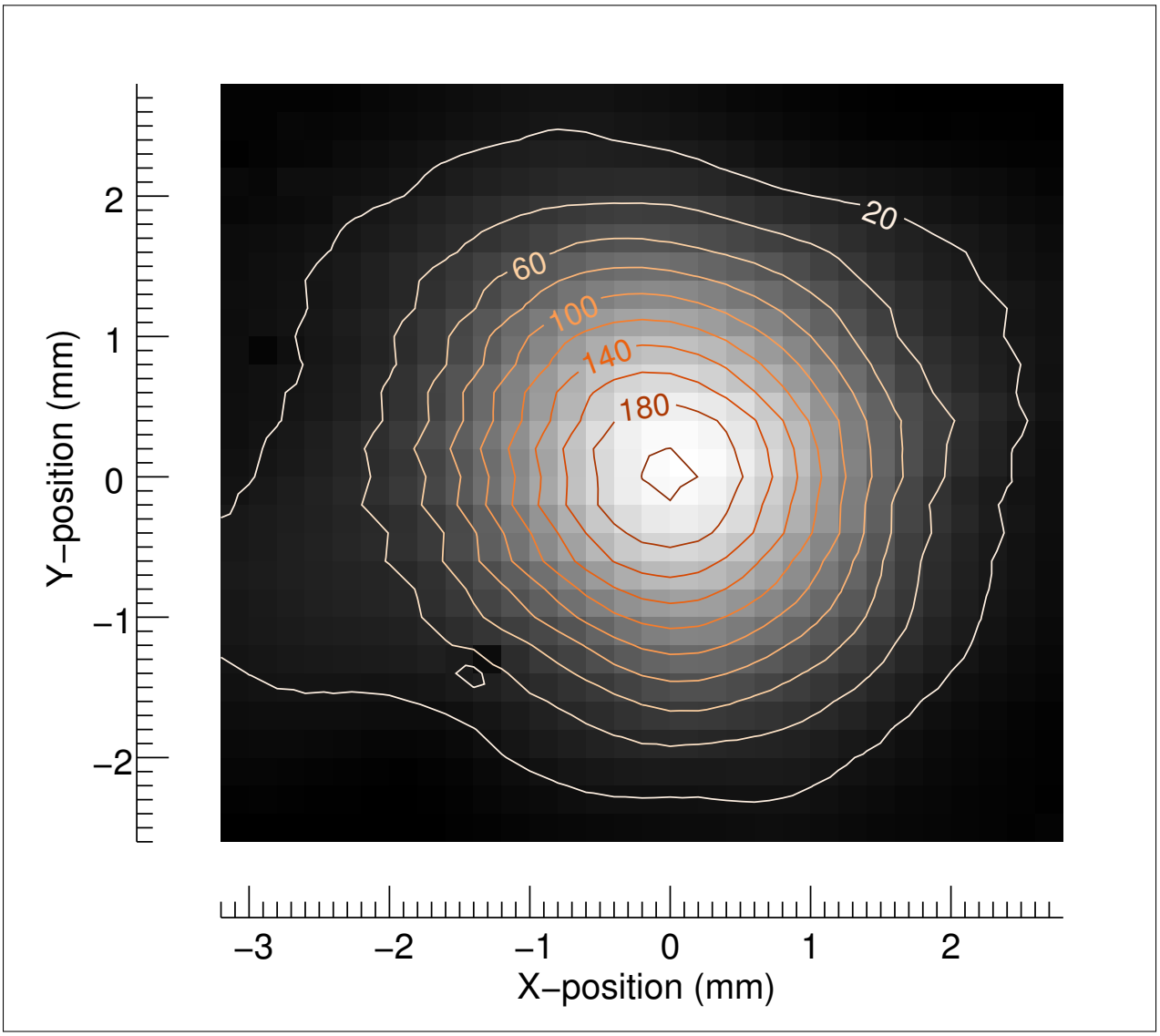

Figure 5.7: Intensity map of cavity output with nonax component in place. X- and Y-coordinate systems are centered on the peak of the output feature. The output is plotted as a black-and-white intensity map with contours in millivolts overlaid. The observed intensity feature has FWHM of $\approx$ 2.36 mm, but deconvoluting the detector shape shows the true FWHM to be $\approx$ 1.8 mm.

commercially available detector. This method can be generalized to any material and applied to cavities of any size. We note that axial symmetry in an ICOS cavity can also be broken by the use of astigmatic cell mirrors, but such output is subject to its own constraints and astigmatism may offer little improvement to collection efficiency. The non-axial component described here provides a simple, effective, and robust means of increasing collection efficiencies.

This method can be generalized to any material and applied to cavities of any size. The optical element described here is made of ZnSe to minimize transmission losses at 2.6 microns, but for instruments operating in wavelength regions less susceptible to absorption by OH bonds or other impurities, this component could be manufactured out of inexpensive and easily machinable optical materials. Optical glasses typically have indices of refraction around 1.5, so designs using these materials would require larger wedge angles to correct for the same amount of skewness. For example, to correct the ChiWIS skewness using BK7 ($n \approx 1.48$), a wedge angle of 5.44° would be required, resulting in a difference in thickness of about 3.3 mm across the part, which is about twice that of the ZnSe design presented here. Wedges with angles of about 5° are well within the capabilities of most optics manufacturers.

We derive the relationship between cavity geometry and skewness, and show that the skew angle γ and concentration factor h/A are completely determined by the dimensionless cavity geometry numbers $u = f/d$ and $v = A/d$. These numbers provide a convenient way to compare the geometries of different instruments, and to gauge a design's susceptibility to having a large skew invariant. We show that skew angles are most sensitive to the cavity aspect ratio v and that in practice, ICOS instrument designs have clustered around similar v, meaning that skewness constraints scale with instrument size.

In the present generation of instruments, skewness constraints are most significant in longer-wavelength instruments, which have larger beam spot sizes ($\lambda^{1/2}$) and therefore require larger cavity mirrors to separate spots on the cavity mirrors by several spot diameters to avoid optical resonance effects. In the future, skewness may become a more widespread

concern as instruments are miniaturized while mirror size remains constrained by optical considerations. Use of ICOS in low sample volume applications such as breath analyzers, fast samplers with rapid flush times, lightweight instruments for unmanned aircraft and field-portable sensors all may warrant use of non-axial components designed to increase collection efficiency.

Table 5.2: **Positions of optical components in ray tracing calculations** All dimensions are in mm. D_1, D_2, D_3, and D_4 are the distances from the plano face of the cavity output mirror to the plano faces of the nonax, PCX1, PCX2, and detector, respectively.

Calculation	D_1	D_2	D_3	D_4
No Nonax	NA	16.50	75.00	83.01
Design Nonax	12.66	29.16	87.66	95.67
Manufactured Nonax	12.66	29.16	87.66	96.31

CHAPTER 6

OVERVIEW OF MEASUREMENTS AND PERFORMANCE

This chapter presents a brief overview of the measurements ChiWIS made during the StratoClim campaign, discusses calibration procedures in converting raw data to derived measureents, and explores some of the successes and failures of its design. As of this writing, all StratoClim data remain preliminary, so science interpretations will be deferred to subsequent manuscripts. This chapter is included to demonstrate that the ChiWIS instrument achieved its design objectives and produced science-quality data.

6.1 StratoClim overview

The StratoClim project was designed to improve understanding of key processes in the Upper Troposphere and Lower Stratosphere (UT/LS) region, including the role of the Asian Monsoon in affecting the chemistry and radiative properties of this region. The project aimed to synthesize data from field campaigns, satellite data products, process modeling, and global modeling to achieve a better understanding of processes including the transport of water and surface-level pollutants to the region and the formation of thin cirrus. Observational efforts included aircraft field campaigns in Europe and Asia, and balloon launches of radiosondes in South Asia and the Pacific. The aircraft field campaigns were divided into three parts, which are described below. Each subsection describes ChiWIS development efforts and achievements during that phase of the campaign.

6.1.1 Overview of the campaigns

Phase I Campaign

The Phase I Campaign took place in Kiruna, Sweden during March/April, 2016. It was intended as an opportunity for instruments to integrate with the aircraft and participate in

engineering flights, but was cut short due to aircraft issues which necessitated rescheduling past the dates of the original flight permits. Progress with ChiWIS was limited to physical integration onto the aircraft, which included fitup to the instrument rack, modification of part of the aircraft fuselage to accommodate the instrument, match drilling of the instrument and rack, cable testing, and confirmation of absence of conflicts with the dome that covers the instruments. The failure to obtain permits to extend the mission precluded the planned full electrical check and test/engineering flights to evaluate instrument performance.

Mediterranean Campaign

The Mediterranean Campaign out of Kalamata, Greece in August/September, 2016 was organized to make up for the failed Kiruna campaign. Instruments, including ChiWIS, were given the opportunity to complete integration with the aircraft and participate in test/engineering flights. Four flights were scheduled, but the last was cancelled due to severe flooding. ChiWIS participated in two of these flights, but suffered from major power failures during each of them. Test flights revealed that the instrument's 3-phase AC to 270 Vdc converters, although rated to 70,000 feet altitude, were not reliable at these altitudes and corresponding low ambient pressures, presumably due to arcing. ChiWIS took no spectra during this campaign, but the power supply failures spurred another round of design and testing that resulted in a change of power conversion scheme and components.

Asian Monsoon Campaign

The Asian Monsoon Campaign took place out of Kathmandu, Nepal in July/August 2017. This campaign consisted of eight flights over Nepal, India, and Bangladesh. (Most instruments were shipped to Kathmandu for integration and did not participate in transit flights between Moscow and Kathmandu.) ChiWIS returned good data on 6 of the 8 flights. The flights returning no data or compromised data were the first, in which a loose contact resulted in about 10% of spectra being recorded, and flight 5, in which a power failure in the

hangar about an hour before rollout allowed ground air into the cavity. Data from this flight shows a clear trend in water vapor due to contamination.

6.1.2 Flight campaign payload

Aside from ChiWIS, the Geophysica payload included approximately twenty other instruments, with some substitution of instruments on different flights. ChiWIS remained mounted for the entire campaign. Payload instruments measured multiple quantities of interest in the UT/LS region, including pressure, temperature, water vapor, total water, particle number density in multiple size bins from nm to hundreds of microns, aerosol composition, and trace gases including CO_2, N_2O, CH_4, O_3, SO_3, H_2SO_4, NO, HNO_3, and NO_y, as well as chlorine and bromine species.

6.2 AM field campaign description

6.2.1 The 2017 Asian Summer Monsoon

Meteorological conditions differed in the first and second halves of the campaign, producing scientifically useful contrasts. The first half featured little local convection (or rainfall), warmer tropopause temperatures and therefore higher near-tropopause water vapor, but few encounters with UT/LS cirrus. The second half featured increasing convection centered around Nepal, colder tropopause temperatures and therefore lower near-tropopause water, and frequent encounters with UT/LS cirrus, including optically thick outflows from high-altitude convection.

6.2.2 Flights

Flights during the AM campaign were almost completely over land, and consequently sample local convection that was continental in character. Flights 2, 4, and 5 were completely within Nepal, but flights 3, 6, 7, and 8 went over India and Bangladesh as well.

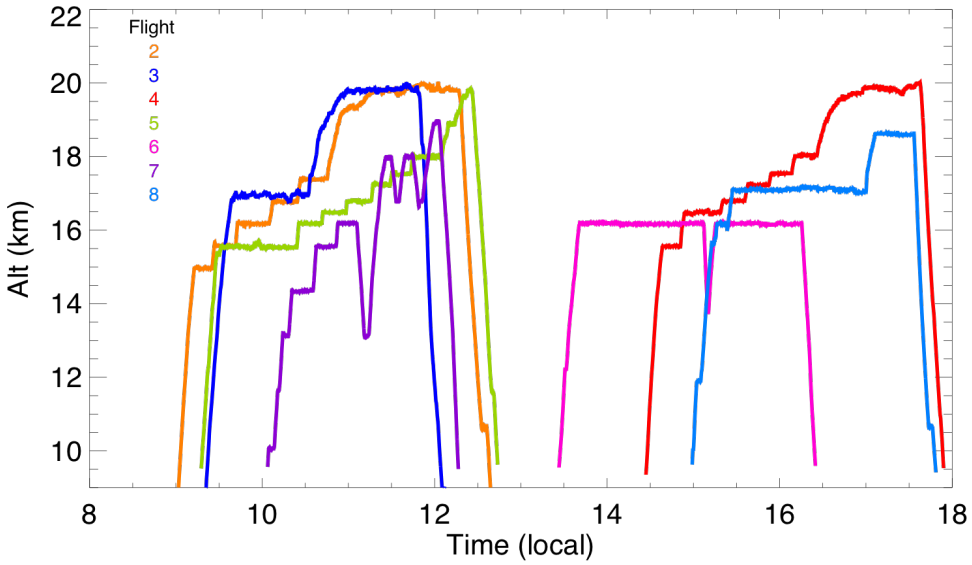

Figure 6.1: Flight profiles for flights 2-8 in the StratoClim campaign. Flights occurred in both the morning and afternoon, and different flight profiles are set to achieve different objectives.

The early flights in the campaign typically consisted of very long legs at high altitude. The reason for this was to accommodate the GLORIA (Gimballed Limb Obxserver for Radiance Imaging of the Atmosphere) instrument, which makes downward-looking profile measurement. Because GLORIA measurements must be made in clear air, few attempts were made to intersect convection. From flight 5 onward, GLORIA was replaced by the in-situ mass spectrometer STRATOMAS, and flight profiles became significantly more complex, with multiple legs at different altitudes, dives to lower altitude, and detours to sample convective outflow. Flight patterns with many different altitude legs and dives are helpful for ChiWIS to build up δD vs. altitude profiles.

6.2.3 Supporting Water Instruments

Two other well-established water instruments made primary measurements of water. The first is the Fluorescence Advanced Stratospheric Hygrometer (FLASH) instrument [Sitnikov et al., 2007], which measures H_2O using the Lyman-α technique. It is designed to measure water vapor mixing ratios between 0.5 and 300 ppm at altitudes of 8-21 kilometers. This

type of instrument does not provide an absolute measurement and must be calibrated in lab before each flight.

The second important water instrument is Fast In-situ Stratospheric Hygrometer (FISH) [Zöger et al., 1998], which reports total water, that is, the sum of the vapor and condensed phases. It does this by utilizing a forward facing inlet which takes in all phases present, then heats the inlet air to transform everything to the vapor phase. During periods of clear air, FISH acts as a water vapor measurement like ChiWIS and FLASH.

Both of these instruments provide essential context and comparisons to the water vapor mixing ratios reported by ChiWIS. Characterizing and understanding the differences between these three instruments is ongoing as of this writing. Several other instruments aboard the Geophysica during StratoClim measure water, but are reliable only at higher concentrations than the ppm ranges seen in the UT/LS, as the instruments are not optimized for this measurement range and suffer from sensitivity and/or contamination concerns. (Water is a highly polar molecule and so adsorbs on surfaces.)

6.3 Data reduction procedures

6.3.1 Thermal pedestal removal

Although instrument performance during StratoClim was largely as expected, one unforeseen issue complicates data reduction. The signal detector picks up a significant amount of power from some other source than the laser. This component of the power was first noticed during the campaign during periods of high water vapor concentration, when the big water line would appear to optically saturate, but at a value much higher than the zero measured during the laser off time between ramps. This was later verified in lab by flooding the cell with N_2O, which has a very weak, but dense forest of spectral lines underneath the spectral region used during the campaign. These data showed the existance of a roughly linear 'pedestal' underneath the signal due to the coherent laser beam.

The pedestal shows no evidence of spectral lines of its own, and therefore is probably not a second mode of the laser. The frequency of the pedestal is significantly different from the laser as evidenced by the fact that the pedestal light makes very few passes through the cell. Roughly 75% of the pedestal power can be blocked by a mask about 1/2 inch arcoss placed on the mirror. We therefore term this optical contribution the 'thermal pedestal'.

The pedestal's shape was reconstructed by placing an infrared filter (Thorlabs FB2750-500) in the shutter's flipper motor, and flipping it into and out of the beam path every thirty seconds during a long data set in lab. This method blocks nearly all the pedestal light (Figure 6.2, left), and allows reconstruction of the thermal pedestal's shape (Figure 6.2, right).

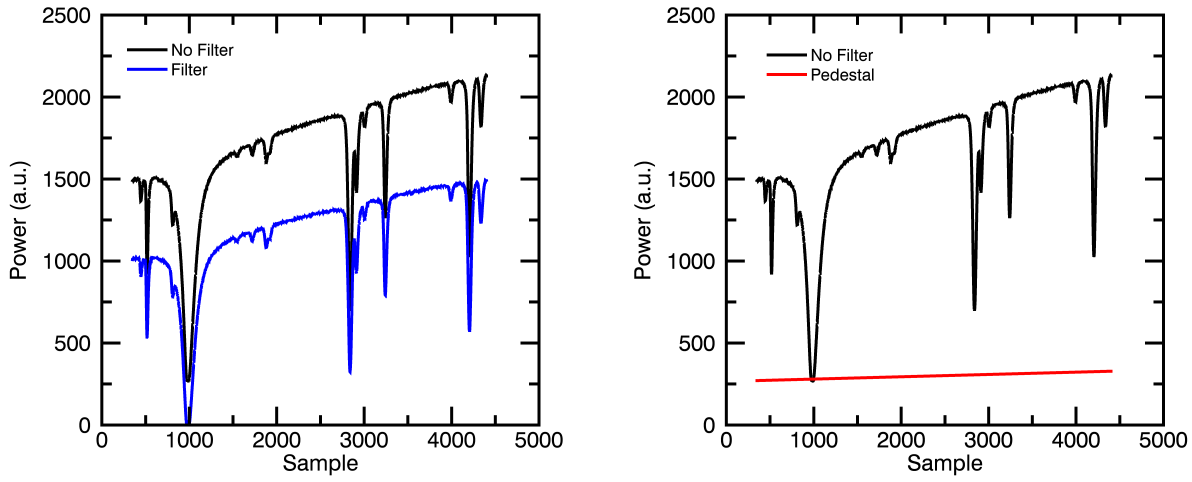

Figure 6.2: Including an infrared filter in the beam path removes the pedestal and attenuates the laser signal by about 17%.

A reasonable estimate of the pedestal can be obtained by fitting the filtered signal to the unfiltered signal with a three parameter fit. The three parameters are the y-intercept and slope of a linear pedestal and a scale factor on the filtered signal. This fitting procedure yields excellent results except for the introduction of optical fringing in some of the spectral lines due to reflection off of the uncoated side of the filter. The best results are obtained by using filtered and unfiltered spectra that are within several seconds of each other to minimize effects due to variations in concentration. The retrieved pedestal value can be subtracted

from ChiWIS data from StratoClim in order to correct the data.

The exact physical origin of this pedestal are unclear, but it is localized to within the laser can. Most likely the chip is simply evolving a large amount of heat, and the collimation lens points a lot of that thermal radiation forward along with the coherent beam. The index of refraction of BD-2 in the wavelength range at which this thermal radiation must be (it is constrained by the filter and the sensitivity cutoff of the detector at about 4 microns) is similar to the index at 2.65 microns, so the radiation would mainly be pointed along the beam. It is also possible that the laser power is interacting with a substandard coating either on the collimation lens or the sapphire can window, although the latter is especially improbable. Understanding and addressing this issue is ongoing.

6.3.2 Non-zero 'zero'

Filtering the beam to remove the pedestal reveals that optically saturated spectral features extend slightly below the 'zero' measured between ramps. The right panel of Figure 6.2 shows that the tip of the big water line at approximately sample 1000 extends slightly below the estimated pedestal. A second set of measurements presented in Figure 6.3 suggests this is not This effect is likely due to a small leakage current flowing through the laser diode which results in incoherent diode mode emission. The long term solution to this problem is to carefully rework the ramp generator to provide a true zero current between ramps, but in the short term this issue must be quantified in order to accurately correct StratoClim data.

This effect is comparable in size to the dip below the red pedestal line shown in the right panel of Figure 6.2.

6.4 Necessary Improvements

Tests to date suggest several necessary improvements that should be made before ChiWIS flies again. These improvements would help the performance of the instrument in flight, and

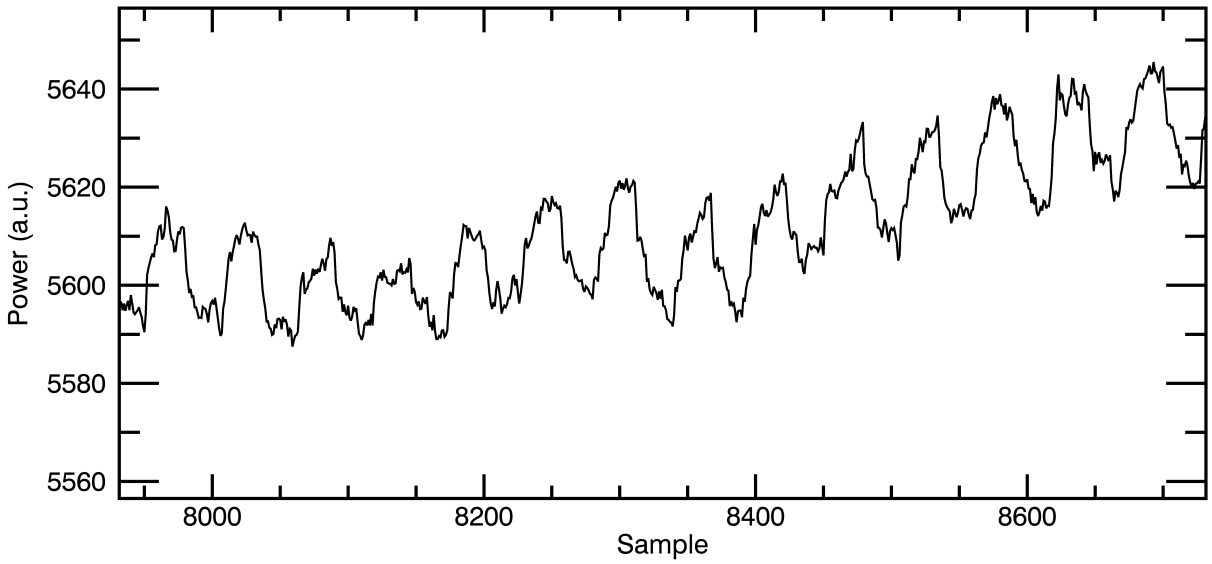

Figure 6.3: Average of about 60 points during the time between ramps during a data run where a shutter blocked then unblocked the beam every thirty seconds. The blocked periods are about 10-15 units lower than the open regions, which seems to indicate the laser is still producing a low amount of light during those times. Each sample is roughly one second.

make it more resilient on the ground.

6.4.1 Normally Closed Valves

The first improvement is to ensure that if power failures occur that the valves close automatically. Ground air entering the chamber is devastating, due to water's tendency to adsorb to everything. It can take hours to flush out the moisture introduced by ground air, and this can compromise measurements if there is not sufficient time before flight. One possibility would be to replace the valves with a model that is 'normally closed'.

The current MKS valves can be electronically configured to be 'normally closed', so an easier option would be to install a backup power supply that would power only the valves in the event of a power failure. This supply would only need to have enough stored energy to close the valves once, so it need not be large.

6.4.2 Pumphead overheating

During StratoClim we were extremely conservative about running the pump at high RPMs for fear of it over heating, and it still occurred. During each flight in StratoClim, the pumphead reached the first software limit for temperature, and consequently the pump's RPM value was reduced. This overheating never occurs at ground level, and is due to the vastly reduced ability of convection to cool the pumphead at low pressure. It is not immediately obvious how to address this problem, although removing the plastic shroud around the pumphead would be a start, as would attaching cooling fins optimized to radiate away heat.

6.4.3 Insufficient Flow

If overheating problem can be adequately addressed, then the problem of insufficient flow at high altitudes should be addressed as well. At the highest altitudes, ChiWIS was unable to maintain its target pressure of 40 millibars, and typically fell significantly below that. This decreases the SNR of the instrument since lower pressure means fewer absorbers in the cavity and smaller spectral lines.

Simply increasing the pump RPM's in flight would probably handle this problem, but it must be tested in an environmental chamber in order to be done safely. One other possibility that could help would be better inlet design and placement on the aircraft. The AMICA instrument also suffered from inability to maintain pressure, and there was some evidence that the fact that the inlets were seeing lower pressure than ambient due to the inlet shape and position on the dome was part of the problem.

6.5 Future Work

In the absence of any planned Geophysica campaigns, ChiWIS must be repurposed. It is possible that the instrument could be refashioned to work aboard the WB-57, but in the short term the instrument is being prepared to make ground level measurements to study

isotopic disequilibrium effects in atmospheric systems by making simultaneous measurements of multiple isotopologues from a tall building on the University of Chicago campus.

The JPL lasers can be tuned to a nearby spectral region shown in Figure 6.4 which contains H_2O, $H_2{}^{18}O$, $H_2{}^{17}O$, and $HD^{18}O$ absorption lines. The data presented in the figure were taken at roughly 5000 ppm, based on the temperature and relative humidity measured in the lab. These lines are all fairly weak, and are better suited to measurements in the range of 500 to 20000 ppm. This spectral region provides all of the isotopologues typically measured in the literature, and each has at least one spectral feature that that suffers from little interference due to neighbors. Most interesting is the presence of two small ($\approx 0.5\%$ deep) $HD^{18}O$ spectral lines. To the best of this author's knowledge, this isotopologue has never been measured in the vapor phase at high data acquisition rates using optical techniques.

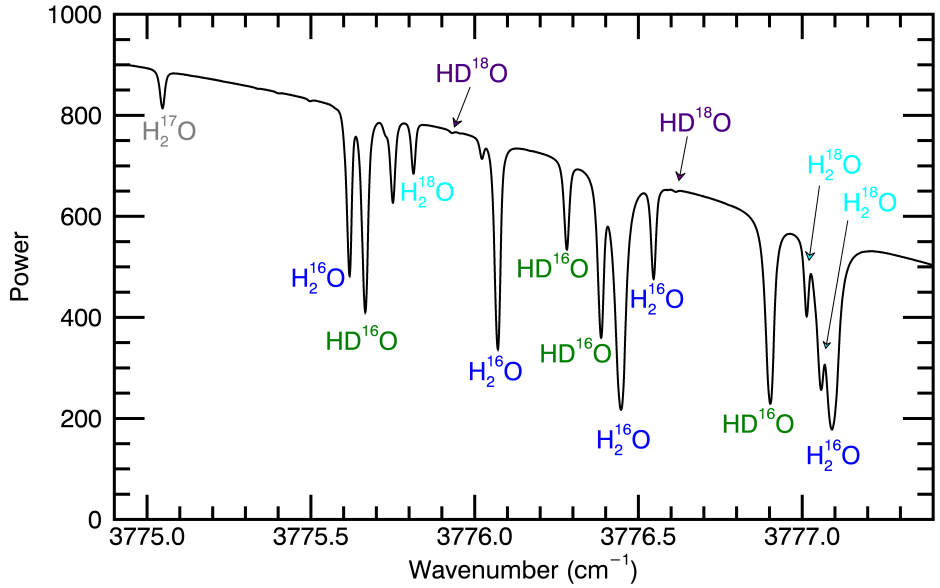

Figure 6.4: Data taken using ChiWIS's secondary spectral region, which is more appropriate for measurements at ground level where mixing ratios can range from thousands to tens of thousands of ppm. The spectrum shown here is a ten second average, with the thermal pedestal unsubtracted.

Aside from the obvious allure of making an $HD^{18}O$ measurement, ground level measure-

ments can shed light on a variety of phenomena. Gorski et al. [2015] showed, for example, that up to 13% of surface level water vapor in winter Salt Lake City was due to waters of combustion. The D/H ratios in waters of combustion tend to reflect the isotopic composition of the hydrocarbons involved, since there is no other end product for the hydrogen atom except in water molecules. Sensitive enough measurements can also detect the difference between bare soil evaporation, evapo-transpiration, and evaporation from water surfaces. As was discussed in section 1.2.5, measurements in Earth's boundary layer are subject to many different influences and it is not immediately obvious how to interpret measurements. Modeling will be required to understand how wind speed and direction influence an air parcel's interaction with nearby sources and sinks.

The instrument will require some modification to operate continuously at ground level. Unfortunately, 3-phase power sources are not readily available in campus buildings, so it will be directly powered from a 115 Vac - 270 Vdc converter, which requires minor modification of the power distribution system. Additionally, the instrument will have to use a much longer inlet line ($\approx$ 20 meters), which will require much more validation before it can be trusted.

Being stationed on a building also means dealing with building exhaust as a source of potential contamination. Aside from careful inlet placement, one method for dealing with these exhausts is to have co-located CO_2 measurement, which is a good indicator of any sort of exhaust or leakage from a building. ChiWIS will be co-located with such an instrument on loan from the Wofsy group at Harvard University.

CHAPTER 7

CONCLUSION

This work discusses the design and operation of the Chicago Water Isotope Spectrometer, a new ICOS instrument for making measurements of the HDO/H_2O ratio in the Asian Summer Monsoon. In addition, it discusses scientific results (Chapter 3) from previous work that informed the design of the instrument, and reports on the design and construction of a new optical component that increased the collection efficiency of ChiWIS by a factor of approximately six (Chapter 5). This non-axially symmetric optical component can aid in the miniaturization of ICOS instruments, which is important for devices that need to sample quickly or have low volumes. The instrument flew aboard the M55 Geophysica during the StratoClim Asian Summer Monsoon field campaign for eight flights, and returned quality data for six of those eight flights. Once the data is corrected and quality controlled, it will provide the first in-situ measurements of the HDO/H_2O ratio in the Asian Summer Monsoon. This data set will provide insight into the monsoon's importance as a source of stratospheric water vapor, and shed light on the differences in moisture transport between the Asian Monsoon and the North American Monsoon, which have very different isotopic signatures. In lieu of more aircraft-borne measurements of the UT/LS, the instrument will make measurements of water vapor isotopologues from a ground site on the University of Chicago campus.

REFERENCES

Andrew J. Amaya, Harshad Pathak, Viraj P. Modak, Hartawan Laksmono, N. Duane Loh, Jonas A. Sellberg, Raymond G. Sierra, Trevor A. McQueen, Matt J. Hayes, Garth J. Williams, Marc Messerschmidt, Sbastien Boutet, Michael J. Bogan, Anders Nilsson, Claudiu A. Stan, and Barbara E. Wyslouzil. How cubic can ice be? *The Journal of Physical Chemistry Letters*, 8(14):3216–3222, 2017. doi: 10.1021/acs.jpclett.7b01142. PMID: 28657757.

L Araguás-Araguás, K Froehlich, and K Rozanski. Deuterium and oxygen-18 isotope composition of precipitation and atmospheric moisture. *Hydrological Processes*, 14(8):1341–1355, 2000. ISSN 1099-1085. doi: 10.1002/1099-1085(20000615)14:8¡1341::AID-HYP983¿3.0.CO;2-Z. URL `http://dx.doi.org/10.1002/1099-1085(20000615)14:8<1341::AID-HYP983>3.0.CO;2-Z`.

B.H. Armstrong. Spectrum line profiles: The voigt function. *Journal of Quantitative Spectroscopy and Radiative Transfer*, 7(1):61 – 88, 1967. ISSN 0022-4073. doi: https://doi.org/10.1016/0022-4073(67)90057-X. URL `http://www.sciencedirect.com/science/article/pii/002240736790057X`.

Douglas Baer, J.B. Paul, Manish Gupta, and A OKeefe. Sensitive absorption measurements in the near-infrared region using off-axis integrated-cavity-output spectroscopy. *Applied Physics B*, 75:261–265, 09 2002.

Yury A. Bakhirkin, Anatoliy A. Kosterev, Chad Roller, Robert F. Curl, and Frank K. Tittel. Mid-infrared quantum cascade laser based off-axis integrated cavity output spectroscopy for biogenic nitric oxide detection. *Appl. Opt.*, 43(11):2257–2266, Apr 2004. doi: 10.1364/AO.43.002257. URL `http://ao.osa.org/abstract.cfm?URI=ao-43-11-2257`.

R. J. Barber, J. Tennyson, G. J. Harris, and R. N. Tolchenov. A high-accuracy computed water line list. *Monthly Notices of the Royal Astronomical Society*, 368(3):1087–1094, 2006. doi: 10.1111/j.1365-2966.2006.10184.x. URL + `http://dx.doi.org/10.1111/j.1365-2966.2006.10184.x`.

Paul De Biévre, Marc Gallet, Norman E. Holden, and I. Lynus Barnes. Isotopic abundances and atomic weights of the elements. *Journal of Physical and Chemical Reference Data*, 13 (3):809–891, 1984. doi: 10.1063/1.555720. URL `https://doi.org/10.1063/1.555720`.

M. Blackman and N.D. Lisgarten. Electron diffraction investigations into the cubic and other structural forms of ice. *Advances in Physics*, 7(26):189–198, 1958. doi: 10.1080/00018735800101217. URL `https://doi.org/10.1080/00018735800101217`.

A. W. Brewer. Evidence for a world circulation provided by the measurements of helium and water vapour distribution in the stratosphere. *Quarterly Journal of the Royal Meteorological Society*, 75(326):351–363, 1949. doi: 10.1002/qj.49707532603. URL `https://rmets.onlinelibrary.wiley.com/doi/abs/10.1002/qj.49707532603`.

Ryan M. Briggs, Clifford Frez, Mahmood Bagheri, Carl E. Borgentun, James A. Gupta, Mark F. Witinski, James G. Anderson, and Siamak Forouhar. Single-mode 2.65 μm ingaassb/alingaassb laterally coupled distributed-feedback diode lasers for atmospheric gas detection. *Opt. Express*, 21(1):1317–1323, Jan 2013. doi: 10.1364/OE.21.001317. URL http://www.opticsexpress.org/abstract.cfm?URI=oe-21-1-1317.

Christopher D. Cappa, Melissa B. Hendricks, Donald J. DePaolo, and Ronald C. Cohen. Isotopic fractionation of water during evaporation. *Journal of Geophysical Research: Atmospheres*, 108(D16), 2003. doi: 10.1029/2003JD003597. URL https://agupubs.onlinelibrary.wiley.com/doi/abs/10.1029/2003JD003597.

J. M. St. Clair, T. F. Hanisco, E. M. Weinstock, E. J. Moyer, D. S. Sayres, F. N. Keutsch, J. H. Kroll, J. N. Demusz, N. T. Allen, J. B. Smith, J. R. Spackman, and J. G. Anderson. A new photolysis laser-induced fluorescence instrument for the detection of h2o and hdo in the lower stratosphere. *Review of Scientific Instruments*, 79(6):064101, 2008. doi: 10.1063/1.2940221. URL https://doi.org/10.1063/1.2940221.

T. Corti, B. P. Luo, M. de Reus, D. Brunner, F. Cairo, M. J. Mahoney, G. Martucci, R. Matthey, V. Mitev, F. H. dos Santos, C. Schiller, G. Shur, N. M. Sitnikov, N. Spelten, H. J. Vssing, S. Borrmann, and T. Peter. Unprecedented evidence for deep convection hydrating the tropical stratosphere. *Geophysical Research Letters*, 35(10), 2008. doi: 10.1029/2008GL033641. URL https://agupubs.onlinelibrary.wiley.com/doi/abs/10.1029/2008GL033641.

H Craig and LI Gordon. Deuterium and oxygen 18 variations in the ocean and the marine atmosphere, ln: Tongiorgi, e.(ed.), stable isotopes in oceanographic studies and paleotemperatures. *CNR, Pisa*, page 9, 1965.

Harmon Craig. Isotopic variations in meteoric waters. *Science*, 133(3465):1702–1703, 1961. ISSN 0036-8075. doi: 10.1126/science.133.3465.1702. URL http://science.sciencemag.org/content/133/3465/1702.

Robert E Criss. *Principles of stable isotope distribution*. Oxford University Press on Demand, 1999.

D. J. Cziczo, P. J. DeMott, S. D. Brooks, A. J. Prenni, D. S. Thomson, D. Baumgardner, J. C. Wilson, S. M. Kreidenweis, and D. M. Murphy. Observations of organic species and atmospheric ice formation. *Geophysical Research Letters*, 31(12):n/a–n/a, 2004a. ISSN 1944-8007. doi: 10.1029/2004GL019822. URL http://dx.doi.org/10.1029/2004GL019822. L12116.

D. J. Cziczo, D. M. Murphy, P. K. Hudson, and D. S. Thomson. Single particle measurements of the chemical composition of cirrus ice residue during crystal-face. *Journal of Geophysical Research: Atmospheres*, 109(D4):n/a–n/a, 2004b. ISSN 2156-2202. doi: 10.1029/2003JD004032. URL http://dx.doi.org/10.1029/2003JD004032. D04201.

Edwin F. Danielsen. A dehydration mechanism for the stratosphere. *Geophysical Research Letters*, 9(6):605–608, 1982. doi: 10.1029/GL009i006p00605. URL https://agupubs.onlinelibrary.wiley.com/doi/abs/10.1029/GL009i006p00605.

W. Dansgaard. The abundance of o18 in atmospheric water and water vapour. *Tellus*, 5(4):461–469, 1953. doi: 10.1111/j.2153-3490.1953.tb01076.x. URL https://onlinelibrary.wiley.com/doi/abs/10.1111/j.2153-3490.1953.tb01076.x.

W. Dansgaard. Stable isotopes in precipitation. *Tellus*, 16(4):436–468, 1964. doi: 10.3402/tellusa.v16i4.8993. URL https://doi.org/10.3402/tellusa.v16i4.8993.

W. Dansgaard, S. J. Johnsen, J. Møller, and C. C. Langway. One thousand centuries of climatic record from camp century on the greenland ice sheet. *Science*, 166(3903):377–380, 1969. ISSN 0036-8075. doi: 10.1126/science.166.3903.377. URL http://science.sciencemag.org/content/166/3903/377.

Piers M. de F. Forster and Keith P. Shine. Stratospheric water vapour changes as a possible contributor to observed stratospheric cooling. *Geophysical Research Letters*, 26(21):3309–3312, 1999. ISSN 1944-8007. doi: 10.1029/1999GL010487. URL http://dx.doi.org/10.1029/1999GL010487.

C. Dyroff, D. Fütterer, and A. Zahn. Compact diode-laser spectrometer isowat for highly sensitive airborne measurements of water-isotope ratios. *Applied Physics B*, 98(2):537–548, Feb 2010. ISSN 1432-0649. doi: 10.1007/s00340-009-3775-6. URL https://doi.org/10.1007/s00340-009-3775-6.

Christoph Dyroff, S Sanati, Emanuel Christner, A Zahn, M Balzer, H Bouquet, JB McManus, Yenny González-Ramos, and Matthias Schneider. Airborne in situ vertical profiling of hdo/h 2 16 o in the subtropical troposphere during the musica remote sensing validation campaign. *Atmospheric Measurement Techniques*, 8(5):2037, 2015.

Volker Ebert and Jürgen Wolfrum. *Absorption*, pages 231–270. Springer Berlin Heidelberg, Berlin, Heidelberg, 2001. ISBN 978-3-642-56443-7. doi: 10.1007/978-3-642-56443-7_13. URL https://doi.org/10.1007/978-3-642-56443-7_13.

Dieter Ehhalt and Karl Knott. Kinetische isotopentrennung bei der verdampfung von wasser. *Tellus*, 17(3):389–397, 1965.

M. D. Ellehøj, H. C. SteenLarsen, S. J. Johnsen, and M. B. Madsen. Icevapor equilibrium fractionation factor of hydrogen and oxygen isotopes: Experimental investigations and implications for stable water isotope studies. *Rapid Communications in Mass Spectrometry*, 27(19):2149–2158, 2013. doi: 10.1002/rcm.6668. URL https://onlinelibrary.wiley.com/doi/abs/10.1002/rcm.6668.

Gregory S. Engel and Elisabeth J. Moyer. Precise multipass herriott cell design: Derivation of controlling design equations. *Opt. Lett.*, 32(6):704–706, Mar 2007. doi: 10.1364/OL.32.000704. URL http://ol.osa.org/abstract.cfm?URI=ol-32-6-704.

Gregory S. Engel, Walter S. Drisdell, Frank N. Keutsch, Elisabeth J. Moyer, and James G. Anderson. Ultrasensitive near-infrared integrated cavity output spectroscopy technique for detection of co at 1.57 μm: new sensitivity limits for absorption measurements in passive optical cavities. *Appl. Opt.*, 45(36):9221–9229, Dec 2006. doi: 10.1364/AO.45.009221. URL `http://ao.osa.org/abstract.cfm?URI=ao-45-36-9221`.

Richard Engeln, Giel Berden, Rudy Peeters, and Gerard Meijer. Cavity enhanced absorption and cavity enhanced magnetic rotation spectroscopy. *Review of Scientific Instruments*, 69(11):3763–3769, 1998. doi: 10.1063/1.1149176. URL `https://doi.org/10.1063/1.1149176`.

VN Faddeyeva and NM Terentev. *Tables of the probability integral for complex argument*. Pergamon Press, 1961.

D. W. Fahey, R.-S. Gao, O. Möhler, H. Saathoff, C. Schiller, V. Ebert, M. Krämer, T. Peter, N. Amarouche, L. M. Avallone, R. Bauer, Z. Bozóki, L. E. Christensen, S. M. Davis, Georges Durry, C. Dyroff, R. L. Herman, S. Hunsmann, Sergey Khaykin, P. Mackrodt, J. Meyer, J. B. Smith, N. Spelten, R. F. Troy, H. Vömel, S. Wagner, and F. G. Wienhold. The AquaVIT-1 intercomparison of atmospheric water vapor measurement techniques. *Atmospheric Measurement Techniques*, 7(9):3177–3213, 2014. doi: 10.5194/amt-7-3177-2014. URL `https://hal.archives-ouvertes.fr/hal-00971815`.

Aamir Farooq, Jay B Jeffries, and Ronald K Hanson. In situ combustion measurements of h 2 o and temperature near 2.5 m using tunable diode laser absorption. *Measurement Science and Technology*, 19(7):075604, 2008. URL `http://stacks.iop.org/0957-0233/19/i=7/a=075604`.

V. I. (Vasily Ivanovich) Ferronsky, editor. *Environmental isotopes in the hydrosphere*. Wiley & Sons, Chichester ; New York, array edition, 1982. Rev. translation of: Prirodnye izotopy gidrosfery / pod obshchei redaktsiei V.I. Ferronskogo. 1975.

S. Fueglistaler, A. E. Dessler, T. J. Dunkerton, I. Folkins, Q. Fu, and P. W. Mote. Tropical tropopause layer. *Reviews of Geophysics*, 47(1):n/a–n/a, 2009. ISSN 1944-9208. doi: 10.1029/2008RG000267. URL `http://dx.doi.org/10.1029/2008RG000267`. RG1004.

Joseph Galewsky and John V. Hurley. An advection-condensation model for subtropical water vapor isotopic ratios. *Journal of Geophysical Research: Atmospheres*, 115(D16):n/a–n/a, 2010. ISSN 2156-2202. doi: 10.1029/2009JD013651. URL `http://dx.doi.org/10.1029/2009JD013651`. D16116.

Joseph Galewsky, Mel Strong, and Zachary D. Sharp. Measurements of water vapor d/h ratios from mauna kea, hawaii, and implications for subtropical humidity dynamics. *Geophysical Research Letters*, 34(22), 2007. doi: 10.1029/2007GL031330. URL `https://agupubs.onlinelibrary.wiley.com/doi/abs/10.1029/2007GL031330`.

Joseph Galewsky, Christopher Rella, Zachary Sharp, Kimberly Samuels, and Dylan Ward. Surface measurements of upper tropospheric water vapor isotopic composition on the chajnantor plateau, chile. *Geophysi-*

cal Research Letters, 38(17), 2011. doi: 10.1029/2011GL048557. URL https://agupubs.onlinelibrary.wiley.com/doi/abs/10.1029/2011GL048557.

R. S. Gao, P. J. Popp, D. W. Fahey, T. P. Marcy, R. L. Herman, E. M. Weinstock, D. G. Baumgardner, T. J. Garrett, K. H. Rosenlof, T. L. Thompson, P. T. Bui, B. A. Ridley, S. C. Wofsy, O. B. Toon, M. A. Tolbert, B. Kärcher, Th. Peter, P. K. Hudson, A. J. Weinheimer, and A. J. Heymsfield. Evidence that nitric acid increases relative humidity in low-temperature cirrus clouds. *Science*, 303(5657):516–520, 2004. ISSN 0036-8075. doi: 10.1126/science.1091255. URL http://science.sciencemag.org/content/303/5657/516.

Andrew Gettelman, Douglas E. Kinnison, Timothy J. Dunkerton, and Guy P. Brasseur. Impact of monsoon circulations on the upper troposphere and lower stratosphere. *Journal of Geophysical Research: Atmospheres*, 109(D22), 2004. doi: 10.1029/2004JD004878. URL https://agupubs.onlinelibrary.wiley.com/doi/abs/10.1029/2004JD004878.

I.E. Gordon, L.S. Rothman, C. Hill, R.V. Kochanov, Y. Tan, P.F. Bernath, M. Birk, V. Boudon, A. Campargue, K.V. Chance, B.J. Drouin, J.-M. Flaud, R.R. Gamache, J.T. Hodges, D. Jacquemart, V.I. Perevalov, A. Perrin, K.P. Shine, M.-A.H. Smith, J. Tennyson, G.C. Toon, H. Tran, V.G. Tyuterev, A. Barbe, A.G. Csszr, V.M. Devi, T. Furtenbacher, J.J. Harrison, J.-M. Hartmann, A. Jolly, T.J. Johnson, T. Karman, I. Kleiner, A.A. Kyuberis, J. Loos, O.M. Lyulin, S.T. Massie, S.N. Mikhailenko, N. Moazzen-Ahmadi, H.S.P. Mller, O.V. Naumenko, A.V. Nikitin, O.L. Polyansky, M. Rey, M. Rotger, S.W. Sharpe, K. Sung, E. Starikova, S.A. Tashkun, J. Vander Auwera, G. Wagner, J. Wilzewski, P. Wciso, S. Yu, and E.J. Zak. The hitran2016 molecular spectroscopic database. *Journal of Quantitative Spectroscopy and Radiative Transfer*, 203: 3 – 69, 2017. ISSN 0022-4073. doi: https://doi.org/10.1016/j.jqsrt.2017.06.038. URL http://www.sciencedirect.com/science/article/pii/S0022407317301073. HITRAN2016 Special Issue.

Galen Gorski, Courtenay Strong, Stephen P. Good, Ryan Bares, James R. Ehleringer, and Gabriel J. Bowen. Vapor hydrogen and oxygen isotopes reflect water of combustion in the urban atmosphere. *Proceedings of the National Academy of Sciences*, 112(11):3247–3252, 2015. ISSN 0027-8424. doi: 10.1073/pnas.1424728112. URL http://www.pnas.org/content/112/11/3247.

Jack D Graybeal. *Molecular spectroscopy*. Mcgraw-Hill College, 1993.

Taryn Haladay and Graeme Stephens. Characteristics of tropical thin cirrus clouds deduced from joint cloudsat and calipso observations. *Journal of Geophysical Research: Atmospheres*, 114(D8), 2009. doi: 10.1029/2008JD010675. URL https://agupubs.onlinelibrary.wiley.com/doi/abs/10.1029/2008JD010675.

JOHN Hallett, WILLIAM P Arnott, Matthew P Bailey, and JOAN T Hallett. Ice crystals in cirrus. *Cirrus*, pages 41–77, 2002.

Thomas F. Hanisco, E. J. Moyer, E. M. Weinstock, J. M. St. Clair, D. S. Sayres, J. B. Smith, R. Lockwood, J. G. Anderson, A. E. Dessler, F. N. Keutsch,

J. R. Spackman, W. G. Read, and T. P. Bui. Observations of deep convective influence on stratospheric water vapor and its isotopic composition. *Geophysical Research Letters*, 34(4), 2007. doi: 10.1029/2006GL027899. URL https://agupubs.onlinelibrary.wiley.com/doi/abs/10.1029/2006GL027899.

D. Herriott, H. Kogelnik, and R. Kompfner. Off-axis paths in spherical mirror interferometers. *Appl. Opt.*, 3(4):523–526, Apr 1964. doi: 10.1364/AO.3.000523. URL http://ao.osa.org/abstract.cfm?URI=ao-3-4-523.

Donald R. Herriott and Harry J. Schulte. Folded optical delay lines. *Appl. Opt.*, 4(8):883–889, Aug 1965. doi: 10.1364/AO.4.000883. URL http://ao.osa.org/abstract.cfm?URI=ao-4-8-883.

P.V. Hobbs. *Ice Physics*. Clarendon Press, 1974. ISBN 9780198519362. URL https://books.google.com/books?id=2o8JAQAAIAAJ.

J. Hodgkinson and R. P. Tatam. Optical gas sensing: a review. *Measurement Science and Technology*, 24(1):012004, January 2013. doi: 10.1088/0957-0233/24/1/012004.

G. Honjo and K. Shimaoka. Determination of hydrogen position in cubic ice by electron diffraction. *Acta Crystallographica*, 10(11):710–711, Nov 1957. doi: 10.1107/S0365110X57002479. URL https://doi.org/10.1107/S0365110X57002479.

A. Hopfner. Vapor pressure isotope effects. *Angewandte Chemie International Edition in English*, 8(10):689–699, 1969. ISSN 1521-3773. doi: 10.1002/anie.196906891. URL http://dx.doi.org/10.1002/anie.196906891.

Henry G. Houghton. *Physical meteorology*. MIT Press, Cambridge, Mass., 1985. Includes index.

Arpa Hudait and Valeria Molinero. What determines the ice polymorph in clouds? *Journal of the American Chemical Society*, 138(28):8958–8967, 2016. doi: 10.1021/jacs.6b05227. PMID: 27355985.

Arpa Hudait, Siwei Qiu, Laura Lupi, and Valeria Molinero. Free energy contributions and structural characterization of stacking disordered ices. *Phys. Chem. Chem. Phys.*, 18:9544–9553, 2016. doi: 10.1039/C6CP00915H. URL http://dx.doi.org/10.1039/C6CP00915H.

J. Humlíček. Optimized computation of the voigt and complex probability functions. *Journal of Quantitative Spectroscopy and Radiative Transfer*, 27(4):437 – 444, 1982. ISSN 0022-4073. doi: https://doi.org/10.1016/0022-4073(82)90078-4. URL http://www.sciencedirect.com/science/article/pii/0022407382900784.

John V. Hurley, Joseph Galewsky, John Worden, and David Noone. A test of the advectioncondensation model for subtropical water vapor using stable isotopologue observations from mauna loa observatory, hawaii. *Journal of Geophysical Research: Atmospheres*, 117(D19), 2012. doi: 10.1029/2012JD018029. URL https://agupubs.onlinelibrary.wiley.com/doi/abs/10.1029/2012JD018029.

R. Donadio J. Connolly, B. diBenedetto. Specifications of raytran material. *Proc.SPIE*, 0181:0181 – 0181 – 4, 1979. doi: 10.1117/12.957359. URL https://doi.org/10.1117/12.957359.

P Jenniskens and DF Blake. Structural transitions in amorphous water ice and astrophysical implications. *Science*, 265(5173):753–756, 1994. ISSN 0036-8075. doi: 10.1126/science.11539186. URL http://science.sciencemag.org/content/265/5173/753.

Eric J. Jensen, Glenn Diskin, R. Paul Lawson, Sara Lance, T. Paul Bui, Dennis Hlavka, Matthew McGill, Leonhard Pfister, Owen B. Toon, and Rushan Gao. Ice nucleation and dehydration in the tropical tropopause layer. *Proceedings of the National Academy of Sciences*, 110(6):2041–2046, 2013. doi: 10.1073/pnas.1217104110. URL http://www.pnas.org/content/110/6/2041.abstract.

Hui Jia, Weixiong Zhao, Tingdong Cai, Weidong Chen, Weijun Zhang, and Xiaoming Gao. Absorption spectroscopy of ammonia between 6526 and 6538cm-1. *Journal of Quantitative Spectroscopy and Radiative Transfer*, 110(6):347 – 357, 2009. ISSN 0022-4073. doi: https://doi.org/10.1016/j.jqsrt.2009.01.002. URL http://www.sciencedirect.com/science/article/pii/S0022407309000077.

MATS Johansson and KARL ERIK Holmberg. Separation of heavy water in phase equilibria involving pure water or salt-water systems. *Acta Chem. Scand*, 23:765, 1969.

Jean Jouzel and Liliane Merlivat. Deuterium and oxygen 18 in precipitation: Modeling of the isotopic effects during snow formation. *Journal of Geophysical Research: Atmospheres*, 89(D7):11749–11757, 1984. doi: 10.1029/JD089iD07p11749. URL https://agupubs.onlinelibrary.wiley.com/doi/abs/10.1029/JD089iD07p11749.

B Kärcher and W Haag. Factors controlling upper tropospheric relative humidity. In *Annales Geophysicae*, volume 22, pages 705–715. Copernicus GmbH, 2004.

V.L. Kasyutich, C.S.E. Bale, C.E. Canosa-Mas, C. Pfrang, S. Vaughan, and R.P. Wayne. Cavity-enhanced absorption: detection of nitrogen dioxide and iodine monoxide using a violet laser diode. *Applied Physics B*, 76(6):691–697, Jun 2003. ISSN 1432-0649. doi: 10.1007/s00340-003-1153-3. URL https://doi.org/10.1007/s00340-003-1153-3.

J. T. Kiehl and Kevin E. Trenberth. Earth's annual global mean energy budget. *Bulletin of the American Meteorological Society*, 78(2):197–208, 1997. doi: 10.1175/1520-0477(1997)078¡0197:EAGMEB¿2.0.CO;2. URL https://doi.org/10.1175/1520-0477(1997)078<0197:EAGMEB>2.0.CO;2.

Daniel B Kirk-Davidoff, Eric J Hintsa, James G Anderson, and David W Keith. The effect of climate change on ozone depletion through changes in stratospheric water vapour. *Nature*, 402(6760):399, 1999.

T Kobayashi, T Kuroda, and I Sunagawa. Morphology of crystals: Part b. *Terra Scientific, Tokyo*, 1987.

Alexei V. Korolev and Ilia P. Mazin. Supersaturation of water vapor in clouds. *Journal of the Atmospheric Sciences*, 60(24):2957–2974, 2003. doi: 10.1175/1520-0469(2003)060¡2957:SOWVIC¿2.0.CO;2. URL https://doi.org/10.1175/1520-0469(2003)060<2957:SOWVIC>2.0.CO;2.

M. Krämer, C. Schiller, A. Afchine, R. Bauer, I. Gensch, A. Mangold, S. Schlicht, N. Spelten, N. Sitnikov, S. Borrmann, M. de Reus, and P. Spichtinger. Ice supersaturations and cirrus cloud crystal numbers. *Atmospheric Chemistry and Physics*, 9(11):3505–3522, 2009. doi: 10.5194/acp-9-3505-2009. URL https://www.atmos-chem-phys.net/9/3505/2009/.

S. Kremser, I. Wohltmann, M. Rex, U. Langematz, M. Dameris, and M. Kunze. Water vapour transport in the tropical tropopause region in coupled chemistry-climate models and era-40 reanalysis data. *Atmospheric Chemistry and Physics*, 9(8):2679–2694, 2009. doi: 10.5194/acp-9-2679-2009. URL https://www.atmos-chem-phys.net/9/2679/2009/.

Zhiming Kuang, Geoffrey C. Toon, Paul O. Wennberg, and Yuk L. Yung. Measured hdo/h2o ratios across the tropical tropopause. *Geophysical Research Letters*, 30(7), 2003. doi: 10.1029/2003GL017023. URL https://agupubs.onlinelibrary.wiley.com/doi/abs/10.1029/2003GL017023.

Werner F Kuhs, Christian Sippel, Andrzej Falenty, and Thomas C Hansen. Extent and relevance of stacking disorder in ice ic. *Proceedings of the National Academy of Sciences*, 109(52):21259–21264, 2012.

WF Kuhs, DV Bliss, and JL Finney. High-resolution neutron powder diffraction study of ice ic. *Le Journal de Physique Colloques*, 48(C1):C1–631, 1987.

Chun-Ta Lai and James R. Ehleringer. Deuterium excess reveals diurnal sources of water vapor in forest air. *Oecologia*, 165(1):213–223, Jan 2011. ISSN 1432-1939. doi: 10.1007/s00442-010-1721-2. URL https://doi.org/10.1007/s00442-010-1721-2.

Kara D. Lamb. *In-situ isotopic water vapor measurements as a tracer of cold cloud microphysics.* PhD thesis, Ann Arbor, 2015. URL http://gateway.proquest.com/openurl?url_ver=Z39.88-2004rft_-val_fmt=info:ofi/fmt:kev:mtx:dissertation&res_dat=xri:pqmrft_-dat=xri:pqdiss:3725505. Advisors: Elisabeth J. Moyer Committee members: Cheng Chin; Zheng-Tian Lu; Wendy Zhang.

Kara D Lamb, Benjamin W Clouser, Maximilien Bolot, Laszlo Sarkozy, Volker Ebert, Harald Saathoff, Ottmar Möhler, and Elisabeth J Moyer. Laboratory measurements of hdo/h2o isotopic fractionation during ice deposition in simulated cirrus clouds. *Proceedings of the National Academy of Sciences*, 114(22):5612–5617, 2017.

C Lauer. *Aufbau und Validierung eines kalibrationsfreien, extraktiven 1.4 um-Laserhygrometers für den Einsatz an der Aerosolkammer AIDA*. PhD thesis, PhD thesis, 2007.

Michel Legrand and Paul Mayewski. Glaciochemistry of polar ice cores: A review. *Reviews of Geophysics*, 35(3):219–243, 1997. doi: 10.1029/96RG03527. URL https://agupubs.onlinelibrary.wiley.com/doi/abs/10.1029/96RG03527.

Douglas Lowe and A. Robert MacKenzie. Polar stratospheric cloud microphysics and chemistry. *Journal of Atmospheric and Solar-Terrestrial Physics*, 70(1):13 – 40, 2008. ISSN 1364-6826. doi: https://doi.org/10.1016/j.jastp.2007.09.011. URL http://www.sciencedirect.com/science/article/pii/S1364682607002520.

Laura Lupi, Arpa Hudait, Baron Peters, Michael Grünwald, Ryan Gotchy Mullen, Andrew H Nguyen, and Valeria Molinero. Role of stacking disorder in ice nucleation. *Nature*, 551 (7679):218, 2017.

Boaz Luz, Eugeni Barkan, Ruth Yam, and Aldo Shemesh. Fractionation of oxygen and hydrogen isotopes in evaporating water. *Geochimica et Cosmochimica Acta*, 73(22):6697 – 6703, 2009. ISSN 0016-7037. doi: https://doi.org/10.1016/j.gca.2009.08.008. URL http://www.sciencedirect.com/science/article/pii/S0016703709005110.

Majoube, Michel. Fractionnement en oxygne 18 et en deutrium entre leau et sa vapeur. *J. Chim. Phys.*, 68:1423–1436, 1971. doi: 10.1051/jcp/1971681423. URL https://doi.org/10.1051/jcp/1971681423.

Tamsin L Malkin, Benjamin J Murray, Andrey V Brukhno, Jamshed Anwar, and Christoph G Salzmann. Structure of ice crystallized from supercooled water. *Proceedings of the National Academy of Sciences*, 109(4):1041–1045, 2012.

Tamsin L. Malkin, Benjamin J. Murray, Christoph G. Salzmann, Valeria Molinero, Steven J. Pickering, and Thomas F. Whale. Stacking disorder in ice i. *Phys. Chem. Chem. Phys.*, 17:60–76, 2015a. doi: 10.1039/C4CP02893G. URL http://dx.doi.org/10.1039/C4CP02893G.

Tamsin L. Malkin, Benjamin J. Murray, Christoph G. Salzmann, Valeria Molinero, Steven J. Pickering, and Thomas F. Whale. Stacking disorder in ice i. *Phys. Chem. Chem. Phys.*, 17:60–76, 2015b. doi: 10.1039/C4CP02893G. URL http://dx.doi.org/10.1039/C4CP02893G.

D. Marchenko, A. H. Neerincx, J. Mandon, J. Zhang, M. Boerkamp, J. Mink, S. M. Cristescu, S. te Lintel Hekkert, and F. J. M. Harren. A compact laser-based spectrometer for detection of c2h2 in exhaled breath and hcn in vitro. *Applied Physics B*, 118(2):275–280, Feb 2015. ISSN 1432-0649. doi: 10.1007/s00340-014-5983-y. URL https://doi.org/10.1007/s00340-014-5983-y.

Sadao Matsuo, Hideko Kuniyoshi, and Yasuo Miyake. Vapor pressure of ice containing d2o. *Science*, 145(3639):1454–1455, 1964. ISSN 0036-8075. doi: 10.1126/science.145.3639.1454. URL http://science.sciencemag.org/content/145/3639/1454.

Erwin Mayer and Andreas Hallbrucker. Cubic ice from liquid water. *Nature*, 325(6105): 601–602, 1987.

M.R. McCurdy, Y.A. Bakhirkin, and F.K. Tittel. Quantum cascade laser-based integrated cavity output spectroscopy of exhaled nitric oxide. *Applied Physics B*, 85 (2):445–452, Nov 2006. ISSN 1432-0649. doi: 10.1007/s00340-006-2365-0. URL https://doi.org/10.1007/s00340-006-2365-0.

C. R. McKinney, J. M. McCrea, S. Epstein, H. A. Allen, and H. C. Urey. Improvements in mass spectrometers for the measurement of small differences in isotope abundance ratios. *Review of Scientific Instruments*, 21(8):724–730, 1950. doi: 10.1063/1.1745698. URL https://doi.org/10.1063/1.1745698.

L. Merlivat and G. Nief. Fractionnement isotopique lors des changements dtat solidevapeur et liquidevapeur de l'eau des tempratures infrieures 0c. *Tellus*, 19(1):122–127, 1967. doi: 10.1111/j.2153-3490.1967.tb01465.x. URL https://onlinelibrary.wiley.com/doi/abs/10.1111/j.2153-3490.1967.tb01465.x.

Liliane Merlivat. Molecular diffusivities of h216o, hd16o, and h218o in gases. *The Journal of Chemical Physics*, 69(6):2864–2871, 1978. doi: 10.1063/1.436884. URL https://aip.scitation.org/doi/abs/10.1063/1.436884.

Liliane Merlivat and Jean Jouzel. Global climatic interpretation of the deuteriumoxygen 18 relationship for precipitation. *Journal of Geophysical Research: Oceans*, 84(C8):5029–5033, 1979. doi: 10.1029/JC084iC08p05029. URL https://agupubs.onlinelibrary.wiley.com/doi/abs/10.1029/JC084iC08p05029.

PW Milonni and JH Eberly. *Laser Physics (Hoboken, NJ)*. Wiley, 2010.

Emily B Moore and Valeria Molinero. Is it cubic? ice crystallization from deeply supercooled water. *Physical Chemistry Chemical Physics*, 13(44):20008–20016, 2011.

MARCELO Moreira, LEONEL STERNBERG, LUIZ MARTINELLI, REYNALDO VICTORIA, EDELCILIO BARBOSA, LUIZ BONATES, and DANIEL NEPSTAD. Contribution of transpiration to forest ambient vapour based on isotopic measurements. *Global Change Biology*, 3(5):439–450, 1997. doi: 10.1046/j.1365-2486.1997.00082.x. URL https://onlinelibrary.wiley.com/doi/abs/10.1046/j.1365-2486.1997.00082.x.

Philip M. Morse. Diatomic molecules according to the wave mechanics. ii. vibrational levels. *Phys. Rev.*, 34:57–64, Jul 1929. doi: 10.1103/PhysRev.34.57. URL https://link.aps.org/doi/10.1103/PhysRev.34.57.

E.J. Moyer, D.S. Sayres, G.S. Engel, J.M. St. Clair, F.N. Keutsch, N.T. Allen, J.H. Kroll, and J.G. Anderson. Design considerations in high-sensitivity off-axis integrated cavity output spectroscopy. *Applied Physics B*, 92(3):467, Aug 2008. ISSN 1432-0649. doi: 10.1007/s00340-008-3137-9. URL https://doi.org/10.1007/s00340-008-3137-9.

Elisabeth J. Moyer, Fredrick W. Irion, Yuk L. Yung, and Michael R. Gunson. Atmos stratospheric deuterated water and implications for tropospherestratosphere transport. *Geophysical Research Letters*, 23(17):2385–2388, 1996. doi: 10.1029/96GL01489. URL https://agupubs.onlinelibrary.wiley.com/doi/abs/10.1029/96GL01489.

D. M. Murphy and T. Koop. Review of the vapour pressures of ice and supercooled water for atmospheric applications. *Quarterly Journal of the Royal Meteorological Society*, 131(608):1539–1565, 2005. ISSN 1477-870X. doi: 10.1256/qj.04.94. URL http://dx.doi.org/10.1256/qj.04.94.

Benjamin J Murray. Enhanced formation of cubic ice in aqueous organic acid droplets. *Environmental Research Letters*, 3(2):025008, 2008. URL http://stacks.iop.org/1748-9326/3/i=2/a=025008.

Benjamin J Murray and Allan K Bertram. Formation and stability of cubic ice in water droplets. *Physical Chemistry Chemical Physics*, 8(1):186–192, 2006.

Benjamin J Murray, Daniel A Knopt, and Allan K Bertram. The formation of cubic ice under conditions relevant to earth's atmosphere. *Nature*, 434(7030):202, 2005.

Benjamin J. Murray, Christoph G. Salzmann, Andrew J. Heymsfield, Steven Dobbie, Ryan R. Neely III, and Christopher J. Cox. Trigonal ice crystals in earths atmosphere. *Bulletin of the American Meteorological Society*, 96(9):1519–1531, 2015. doi: 10.1175/BAMS-D-13-00128.1.

Ray Nassar, Peter F. Bernath, Chris D. Boone, Andrew Gettelman, Sean D. McLeod, and Curtis P. Rinsland. Variability in hdo/h2o abundance ratios in the tropical tropopause layer. *Journal of Geophysical Research: Atmospheres*, 112(D21), 2007. doi: 10.1029/2007JD008417. URL https://agupubs.onlinelibrary.wiley.com/doi/abs/10.1029/2007JD008417.

Alfred O. Nier. A mass spectrometer for isotope and gas analysis. *Review of Scientific Instruments*, 18(6):398–411, 1947. doi: 10.1063/1.1740961. URL https://doi.org/10.1063/1.1740961.

Anthony O'Keefe. Integrated cavity output analysis of ultra-weak absorption. *Chemical Physics Letters*, 293(5):331 – 336, 1998. ISSN 0009-2614. doi: https://doi.org/10.1016/S0009-2614(98)00785-4. URL http://www.sciencedirect.com/science/article/pii/S0009261498007854.

J.J. Olivero and R.L. Longbothum. Empirical fits to the voigt line width: A brief review. *Journal of Quantitative Spectroscopy and Radiative Transfer*, 17(2):233 – 236, 1977. ISSN 0022-4073. doi: https://doi.org/10.1016/0022-4073(77)90161-3. URL http://www.sciencedirect.com/science/article/pii/0022407377901613.

Joshua B. Paul, Larry Lapson, and James G. Anderson. Ultrasensitive absorption spectroscopy with a high-finesse optical cavity and off-axis alignment. *Appl. Opt.*, 40(27):4904–4910, Sep 2001. doi: 10.1364/AO.40.004904. URL http://ao.osa.org/abstract.cfm?URI=ao-40-27-4904.

Thomas Peter, Claudia Marcolli, Peter Spichtinger, Thierry Corti, Marcia B. Baker, and Thomas Koop. When dry air is too humid. *Science*, 314(5804):1399–1402, 2006. ISSN 00368075, 10959203. URL http://www.jstor.org/stable/20032920.

Raymond T Pierrehumbert. The hydrologic cycle in deep-time climate problems. *Nature*, 419(6903):191, 2002.

Robert Provencal, Manish Gupta, Thomas G. Owano, Douglas S. Baer, Kenneth N. Ricci, Anthony O'Keefe, and James R. Podolske. Cavity-enhanced quantum-cascade laser-based instrument for carbon monoxide measurements. *Appl. Opt.*, 44(31):6712–6717, Nov 2005. doi: 10.1364/AO.44.006712. URL http://ao.osa.org/abstract.cfm?URI=ao-44-31-6712.

Hans R Pruppacher and 1940 Klett, James D. *Microphysics of clouds and precipitation*. Dordrecht ; Boston : Kluwer Academic Publishers, 2nd rev. and enl. ed edition, 1997. ISBN 0792342119 (alk. paper). "With an introduction to cloud chemistry and cloud electricity.".

Jovan Pupezin, Gyorgy Jakli, Gabor Jancso, and W. Van Alexander Hook. The vapor pressure isotope effect in aqueous systems. i. h2o-d2o (-64 to 100) and h216o-h218o (-17 to 16); ice and liquid. *Journal of Physical Chemistry*, 76(5):743–762, 1972. ISSN 0022-3654.

William J. Randel, Elisabeth Moyer, Mijeong Park, Eric Jensen, Peter Bernath, Kaley Walker, and Chris Boone. Global variations of hdo and hdo/h2o ratios in the upper troposphere and lower stratosphere derived from acefts satellite measurements. *Journal of Geophysical Research: Atmospheres*, 117(D6), 2012. doi: 10.1029/2011JD016632. URL https://agupubs.onlinelibrary.wiley.com/doi/abs/10.1029/2011JD016632.

Rayleigh. Lix. on the distillation of binary mixtures. *The London, Edinburgh, and Dublin Philosophical Magazine and Journal of Science*, 4(23):521–537, 1902. doi: 10.1080/14786440209462876. URL https://doi.org/10.1080/14786440209462876.

M. Reverdy, V. Noel, H. Chepfer, and B. Legras. On the origin of subvisible cirrus clouds in the tropical upper troposphere. *Atmospheric Chemistry and Physics*, 12(24):12081–12101, 2012. doi: 10.5194/acp-12-12081-2012. URL https://www.atmos-chem-phys.net/12/12081/2012/.

Roddy R Rogers and MK Yau. *A short course in cloud physics, International series in natural philosophy*. Butterworth Heinemann, Burlington, MA, 1989.

L.S. Rothman, I.E. Gordon, Y. Babikov, A. Barbe, D. Chris Benner, P.F. Bernath, M. Birk, L. Bizzocchi, V. Boudon, L.R. Brown, A. Campargue, K. Chance, E.A. Cohen, L.H. Coudert, V.M. Devi, B.J. Drouin, A. Fayt, J.-M. Flaud, R.R. Gamache, J.J. Harrison, J.-M. Hartmann, C. Hill, J.T. Hodges, D. Jacquemart, A. Jolly, J. Lamouroux, R.J. Le Roy, G. Li, D.A. Long, O.M. Lyulin, C.J. Mackie, S.T. Massie, S. Mikhailenko, H.S.P. Mller, O.V. Naumenko, A.V. Nikitin, J. Orphal, V. Perevalov, A. Perrin, E.R. Polovtseva, C. Richard, M.A.H. Smith, E. Starikova, K. Sung, S. Tashkun, J. Tennyson, G.C. Toon, Vl.G. Tyuterev, and G. Wagner. The hitran2012 molecular spectroscopic database. *Journal of Quantitative Spectroscopy and Radiative Transfer*, 130: 4 – 50, 2013. ISSN 0022-4073. doi: https://doi.org/10.1016/j.jqsrt.2013.07.002. URL

http://www.sciencedirect.com/science/article/pii/S0022407313002859. HITRAN2012 special issue.

D. S. Sayres, L. Pfister, T. F. Hanisco, E. J. Moyer, J. B. Smith, J. M. St. Clair, A. S. O'Brien, M. F. Witinski, M. Legg, and J. G. Anderson. Influence of convection on the water isotopic composition of the tropical tropopause layer and tropical stratosphere. *Journal of Geophysical Research: Atmospheres*, 115(D10), 2010. doi: 10.1029/2009JD013100. URL https://agupubs.onlinelibrary.wiley.com/doi/abs/10.1029/2009JD013100.

D. S. Sayres, R. Dobosy, C. Healy, E. Dumas, J. Kochendorfer, J. Munster, J. Wilkerson, B. Baker, and J. G. Anderson. Arctic regional methane fluxes by ecotope as derived using eddy covariance from a low-flying aircraft. *Atmospheric Chemistry and Physics*, 17(13):8619–8633, 2017. doi: 10.5194/acp-17-8619-2017. URL https://www.atmos-chem-phys.net/17/8619/2017/.

David S. Sayres, E. J. Moyer, T. F. Hanisco, J. M. St. Clair, F. N. Keutsch, A. OBrien, N. T. Allen, L. Lapson, J. N. Demusz, M. Rivero, T. Martin, M. Greenberg, C. Tuozzolo, G. S. Engel, J. H. Kroll, J. B. Paul, and J. G. Anderson. A new cavity based absorption instrument for detection of water isotopologues in the upper troposphere and lower stratosphere. *Review of Scientific Instruments*, 80(4):044102, 2009. doi: 10.1063/1.3117349. URL https://doi.org/10.1063/1.3117349.

Daniel V Schroeder. *An introduction to thermal physics*. AAPT, 1999.

F. V. Shallcross and G. B. Carpenter. Xray diffraction study of the cubic phase of ice. *The Journal of Chemical Physics*, 26(4):782–784, 1957. doi: 10.1063/1.1743404. URL https://doi.org/10.1063/1.1743404.

J. E. Shilling, M. A. Tolbert, O. B. Toon, E. J. Jensen, B. J. Murray, and A. K. Bertram. Measurements of the vapor pressure of cubic ice and their implications for atmospheric ice clouds. *Geophysical Research Letters*, 33(17):n/a–n/a, 2006. ISSN 1944-8007. doi: 10.1029/2006GL026671. URL http://dx.doi.org/10.1029/2006GL026671. L17801.

N. M. Sitnikov, V. A. Yushkov, A. A. Afchine, L. I. Korshunov, V. I. Astakhov, A. E. Ulanovskii, M. Kraemer, A. Mangold, C. Schiller, and F. Ravegnani. The flash instrument for water vapor measurements on board the high-altitude airplane. *Instruments and Experimental Techniques*, 50(1):113–121, Feb 2007. ISSN 1608-3180. doi: 10.1134/S0020441207010174. URL https://doi.org/10.1134/S0020441207010174.

J. Skrotzki, P. Connolly, M. Schnaiter, H. Saathoff, O. Möhler, R. Wagner, M. Niemand, V. Ebert, and T. Leisner. The accommodation coefficient of water molecules on ice cirrus cloud studies at the aida simulation chamber. *Atmospheric Chemistry and Physics*, 13(8):4451–4466, 2013. doi: 10.5194/acp-13-4451-2013. URL https://www.atmos-chem-phys.net/13/4451/2013/.

Julian Skrotzki. *High-accuracy multiphase humidity measurements using TDLAS: application to the investigation of ice growth in simulated cirrus clouds*. PhD thesis, 2012a.

Julian Skrotzki. *High-accuracy multiphase humidity measurements using TDLAS: application to the investigation of ice growth in simulated cirrus clouds*. PhD thesis, 2012b.

D. Sonnenfroh and K. Parameswaran. Diode laser-based sensor for high precision measurements ofambient co2 in network applications. *Applied Physics B*, 102(2): 407–416, Feb 2011. ISSN 1432-0649. doi: 10.1007/s00340-010-4277-2. URL https://doi.org/10.1007/s00340-010-4277-2.

D. C. Steytler, J. C. Dore, and C. J. Wright. Neutron diffraction study of cubic ice nucleation in a porous silica network. *The Journal of Physical Chemistry*, 87(14):2458–2459, 1983. doi: 10.1021/j100237a003. URL http://dx.doi.org/10.1021/j100237a003.

S Svanberg. *Atomic and molecular spectroscopy, Basic aspects and practical applications. Forth ed*. Springer, 2004.

Tru Takahashi. On the role of cubic structure in ice nucleation. *Journal of Crystal Growth*, 59 (3):441 – 449, 1982. ISSN 0022-0248. doi: https://doi.org/10.1016/0022-0248(82)90365-7. URL http://www.sciencedirect.com/science/article/pii/0022024882903657.

Zhongqi Tan and Xingwu Long. Off-axis integrated cavity output spectroscopy and its application. *Optics Communications*, 283(7):1406 – 1409, 2010. ISSN 0030-4018. doi: https://doi.org/10.1016/j.optcom.2009.11.081. URL http://www.sciencedirect.com/science/article/pii/S0030401809012620.

Jonathan Tennyson, Peter F. Bernath, Linda R. Brown, Alain Campargue, Michel R. Carleer, Attila G. Csszr, Robert R. Gamache, Joseph T. Hodges, Alain Jenouvrier, Olga V. Naumenko, Oleg L. Polyansky, Laurence S. Rothman, Robert A. Toth, Ann Carine Vandaele, Nikolai F. Zobov, Ludovic Daumont, Alexander Z. Fazliev, Tibor Furtenbacher, Iouli E. Gordon, Semen N. Mikhailenko, and Sergei V. Shirin. Iupac critical evaluation of the rotationalvibrational spectra of water vapor. part ienergy levels and transition wavenumbers for h217o and h218o. *Journal of Quantitative Spectroscopy and Radiative Transfer*, 110(9): 573 – 596, 2009. ISSN 0022-4073. doi: https://doi.org/10.1016/j.jqsrt.2009.02.014. URL http://www.sciencedirect.com/science/article/pii/S0022407309000703. HITRAN.

Jonathan Tennyson, Peter F. Bernath, Linda R. Brown, Alain Campargue, Attila G. Csszr, Ludovic Daumont, Robert R. Gamache, Joseph T. Hodges, Olga V. Naumenko, Oleg L. Polyansky, Laurence S. Rothman, Robert A. Toth, Ann Carine Vandaele, Nikolai F. Zobov, Sophie Fally, Alexander Z. Fazliev, Tibor Furtenbacher, Iouli E. Gordon, Shui-Ming Hu, Semen N. Mikhailenko, and Boris A. Voronin. Iupac critical evaluation of the rotationalvibrational spectra of water vapor. part ii: Energy levels and transition wavenumbers for hd16o, hd17o, and hd18o. *Journal of Quantitative Spectroscopy and Radiative Transfer*, 111(15):2160 – 2184, 2010. ISSN 0022-4073. doi: https://doi.org/10.1016/j.jqsrt.2010.06.012. URL http://www.sciencedirect.com/science/article/pii/S0022407310002578. XVIth Symposium on High Resolution Molecular Spectroscopy (HighRus-2009).

Jonathan Tennyson, Peter F. Bernath, Linda R. Brown, Alain Campargue, Attila G. Csszr, Ludovic Daumont, Robert R. Gamache, Joseph T. Hodges, Olga V. Naumenko, Oleg L. Polyansky, Laurence S. Rothman, Ann Carine Vandaele, Nikolai F. Zobov, Afaf R. Al Derzi, Csaba Fbri, Alexander Z. Fazliev, Tibor Furtenbacher, Iouli E. Gordon, Lorenzo Lodi, and Irina I. Mizus. Iupac critical evaluation of the rotation-alvibrational spectra of water vapor, part iii: Energy levels and transition wavenumbers for h216o. *Journal of Quantitative Spectroscopy and Radiative Transfer*, 117:29 – 58, 2013. ISSN 0022-4073. doi: https://doi.org/10.1016/j.jqsrt.2012.10.002. URL http://www.sciencedirect.com/science/article/pii/S0022407312004311.

Frank K. Tittel, Dirk Richter, and Alan Fried. *Mid-Infrared Laser Applications in Spectroscopy*, pages 458–529. Springer Berlin Heidelberg, Berlin, Heidelberg, 2003. ISBN 978-3-540-36491-7. doi: 10.1007/3-540-36491-9_11. URL https://doi.org/10.1007/3-540-36491-9_11.

Robert A. Toth and James W. Brault. Line positions and strengths in the (001), (110), and (030) bands of hdo. *Appl. Opt.*, 22(6):908–926, Mar 1983. doi: 10.1364/AO.22.000908. URL http://ao.osa.org/abstract.cfm?URI=ao-22-6-908.

Harold C Urey. The thermodynamic properties of isotopic substances. *Journal of the Chemical Society (Resumed)*, pages 562–581, 1947.

Robert Wagner and Ottmar Mhler. Heterogeneous ice nucleation ability of crystalline sodium chloride dihydrate particles. *Journal of Geophysical Research: Atmospheres*, 118(10):4610–4622, 2013. ISSN 2169-8996. doi: 10.1002/jgrd.50325. URL http://dx.doi.org/10.1002/jgrd.50325.

Milton H. Wahl and Harold C. Urey. The vapor pressures of the isotopic forms of water. *The Journal of Chemical Physics*, 3(7):411–414, 1935. doi: 10.1063/1.1749690. URL https://doi.org/10.1063/1.1749690.

C. R. Webster, R. D. May, C. A. Trimble, R. G. Chave, and J. Kendall. Aircraft (er-2) laser infrared absorption spectrometer (alias) for in-situ stratospheric measurements of hcl, n2o, ch4, no2, and hno3. *Appl. Opt.*, 33(3):454–472, Jan 1994. doi: 10.1364/AO.33.000454. URL http://ao.osa.org/abstract.cfm?URI=ao-33-3-454.

Christopher R. Webster and Andrew J. Heymsfield. Water isotope ratios d/h, 18o/16o, 17o/16o in and out of clouds map dehydration pathways. *Science*, 302 (5651):1742–1745, 2003. ISSN 0036-8075. doi: 10.1126/science.1089496. URL http://science.sciencemag.org/content/302/5651/1742.

Lisa R. Welp, Xuhui Lee, Timothy J. Griffis, XueFa Wen, Wei Xiao, Shenggong Li, Xiaomin Sun, Zhongmin Hu, Maria Val Martin, and Jianping Huang. A meta-analysis of water vapor deuteriumexcess in the midlatitude atmospheric surface layer. *Global Biogeochemical Cycles*, 26(3), 2012. doi: 10.1029/2011GB004246. URL https://agupubs.onlinelibrary.wiley.com/doi/abs/10.1029/2011GB004246.

XueFa Wen, ShiChun Zhang, XiaoMin Sun, GuiRui Yu, and Xuhui Lee. Water vapor and precipitation isotope ratios in beijing, china. *Journal of Geophysical Research: Atmospheres*, 115(D1), 2010. doi: 10.1029/2009JD012408. URL https://agupubs.onlinelibrary.wiley.com/doi/abs/10.1029/2009JD012408.

J. U. White. Long optical paths of large aperture. *Journal of the Optical Society of America (1917-1983)*, 32:285, May 1942.

John U. White. Very long optical paths in air. *J. Opt. Soc. Am.*, 66(5):411–416, May 1976. doi: 10.1364/JOSA.66.000411. URL http://www.osapublishing.org/abstract.cfm?URI=josa-66-5-411.

E.E. Whiting. An empirical approximation to the voigt profile. *Journal of Quantitative Spectroscopy and Radiative Transfer*, 8(6):1379 – 1384, 1968. ISSN 0022-4073. doi: https://doi.org/10.1016/0022-4073(68)90081-2. URL http://www.sciencedirect.com/science/article/pii/0022407368900812.

D.G. Williams, W. Cable, K. Hultine, J.C.B. Hoedjes, E.A. Yepez, V. Simonneaux, S. Er-Raki, G. Boulet, H.A.R. de Bruin, A. Chehbouni, O.K. Hartogensis, and F. Timouk. Evapotranspiration components determined by stable isotope, sap flow and eddy covariance techniques. *Agricultural and Forest Meteorology*, 125(3):241 – 258, 2004. ISSN 0168-1923. doi: https://doi.org/10.1016/j.agrformet.2004.04.008. URL http://www.sciencedirect.com/science/article/pii/S0168192304000930.

R. Winston, J.C. Miñano, and P. Benítez. *Nonimaging Optics*. Electronics & Electrical. Elsevier Academic Press, 2005. ISBN 9780127597515. URL https://books.google.com/books?id=MliJHWwTnVQC.

Enrico A. Yepez, David G. Williams, Russell L. Scott, and Guanghui Lin. Partitioning overstory and understory evapotranspiration in a semiarid savanna woodland from the isotopic composition of water vapor. *Agricultural and Forest Meteorology*, 119(1):53 – 68, 2003. ISSN 0168-1923. doi: https://doi.org/10.1016/S0168-1923(03)00116-3. URL http://www.sciencedirect.com/science/article/pii/S0168192303001163.

W. Zhao, X. Gao, W. Chen, W. Zhang, T. Huang, T. Wu, and H. Cha. Wavelength modulated off-axis integrated cavity output spectroscopy in the near infrared. *Applied Physics B*, 86(2):353–359, Jan 2007. ISSN 1432-0649. doi: 10.1007/s00340-006-2451-3. URL https://doi.org/10.1007/s00340-006-2451-3.

B Zobrist, C Marcolli, DA Pedernera, and Thomas Koop. Do atmospheric aerosols form glasses? *Atmospheric Chemistry and Physics*, 8(17):5221–5244, 2008.

M. Zöger, A. Afchine, N. Eicke, M.T. Gerhards, E. Klein, D. S. McKenna, U. Mrschel, U. Schmidt, V. Tan, F. Tuitjer, T. Woyke, and C. Schiller. Fast in situ stratospheric hygrometers: A new family of balloonborne and airborne lyman photofragment fluorescence hygrometers. *Journal of Geophysical Research: Atmospheres*, 104(D1):1807–1816, 1998. doi: 10.1029/1998JD100025. URL https://agupubs.onlinelibrary.wiley.com/doi/abs/10.1029/1998JD100025.